Multi-pulse PTV: Evaluation on Spatial Resolution, Velocity Accuracy and

Acceleration Measurement

by

Liuyang Ding

Approved April 2014 by the
Graduate Supervisory Committee:

Ronald J. Adrian, Chair
Marcus Herrmann
Huei-ping Huang

ARIZONA STATE UNIVERSITY

May 2014

ABSTRACT

Multi-pulse particle tracking velocimetry (multi-pulse PTV) is a recently proposed flow measurement technique aiming to improve the performance of conventional PTV/ PIV. In this work, multi-pulse PTV is assessed based on PTV simulations in terms of spatial resolution, velocity measurement accuracy and the capability of acceleration measurement. The errors of locating particles, velocity measurement and acceleration measurement are analytically calculated and compared among quadruple-pulse, triple-pulse and dual-pulse PTV. The optimizations of triple-pulse and quadruple-pulse PTV are discussed, and criteria are developed to minimize the combined error in position, velocity and acceleration.

Experimentally, the velocity and acceleration fields of a round impinging air jet are measured to test the triple-pulse technique. A high speed beam-splitting camera and a custom 8-pulsed laser system are utilized to achieve good timing flexibility and temporal resolution. A new method to correct the registration error between CCDs is also presented. Consequently, the velocity field shows good consistency between triple-pulse and dual-pulse measurements. The mean acceleration profile along the centerline of the jet is used as the ground truth for the verification of the triple-pulse PIV measurements of the acceleration fields. The instantaneous acceleration field of the jet is directly measured by triple-pulse PIV and presented. Accelerations up to 1,000 g's are measured in these experiments.

ACKNOWLEDGEMENTS

algorithm development during that period. I hope we will have more wonderful collaborations in the future.

Last but not the least, I sincerely acknowledge the endless love and support from my parents. Without their encouragement and support, I can't have the chance to explore the wonderful experience of graduate study in United States. Their unconditional love is always the biggest motivation for me to pursue my life goals.

TABLE OF CONTENTS

iv

LIST OF TABLES

LIST OF FIGURES

Chapter 1

INTRODUCTION

Advances in the development and application of PIV have made it the dominant ex-
perimental method in fluid mechanics over the last two decades (Adrian, 1991, 2005;
Westerweel *et al.*, 2013). In comparison with two conventional methods, hot-wire
anemometry (HWA) and laser-Doppler velocimetry (LDV), PIV has the advantage of
accessing instantaneous velocity fields, and thus multi-point flow properties and ad-
vanced visualizations. Velocity derivatives, such as velocity gradient tensor, vorticity,
and force, can be estimated by numerically differencing PIV field data. In studies of
turbulence and complex flows, Reynolds stress, spatial correlation, power spectrum,
and dissipation rate can all be directly calculated from PIV measurements (Adrian
and Westerweel, 2011).

In a dual-pulsed planar PIV system, the flow is seeded with micro-scale tracer
particles acting as the fluid markers and illuminated by high-energy pulsed lasers.
Light scattered from particles is collected by the imaging system at two time instants
separated by a small, precise time Δt. The digital images of the particles are then
processed and interrogated determining the displacement field $\Delta \boldsymbol{X}$ in the image do-
main. With the assumption of ideal geometric imaging, the flow velocity field $\boldsymbol{u}$ is
given by

$$\boldsymbol{u} = \frac{\Delta \boldsymbol{x}}{\Delta t} = \frac{\Delta \boldsymbol{X}}{M_0 \Delta t}, \tag{1.1}$$

where $\Delta \boldsymbol{x}$ denotes the displacement vector in the flow domain, and M_0 is the lateral
magnification. Today, cross-correlation has become the standard tool to interrogate
the entire image window by window. Each of the outcome vectors represents the

1

average motion of the group of particles within the interrogation window. Particle tracking algorithms such as the super-resolution technique (Keane *et al.*, 1995) are also applied to track the motion of individual particles. This method can improve the spatial resolution of the measurement, but typically at the cost of increasing the percentage of bad vectors.

The performance of a PIV system is characterized mainly by its dynamic spatial range (DSR) and dynamic velocity range (DVR) (Adrian, 1997). The dynamic spatial range is defined as the ratio of the linear dimension of the field of view to the minimum resolvable length scale of the flow. Let l_x and L_X be the linear dimensions of the field of view and the recording medium, respectively, and related by

$$l_x = L_x/M_0. \tag{1.2}$$

If the maximum displacement is denoted by Δx_{max}, the minimum resolvable scale must be less than Δx_{max}, and the dynamic spatial range can be defined as

$$DSR = \frac{l_x}{\Delta x_{max}} = \frac{L_x/M_0}{\Delta x_{max}}. \tag{1.3}$$

Likewise, the dynamic velocity range is defined as the ratio of the maximum velocity to the minimum resolvable velocity,

$$DVR = \frac{u_{max}}{\sigma_u} = \frac{\Delta x_{max} M_0}{c_\tau d_\tau}, \tag{1.4}$$

where $u_{max} = \Delta x_{max}/\Delta t$ is the full-scale velocity, and $\sigma_u = c_\tau d_\tau/M_0\Delta t$ is the velocity measurement uncertainty, with c_τ being the uncertainty level in locating the particle center and d_τ being the particle diameter. From the definitions, the DSR and DVR reveal the amount of information that a PIV system can hold and the measurement uncertainty level compared to the full-scale velocity. It is also noticed that the product of DSR and DVR is a constant for a given PIV system,

$$DSR \times DVR = \frac{L_X}{c_\tau d_\tau}, \tag{1.5}$$

which indicates that it is beneficial to either increase the size of the recording medium or reduce the measurement uncertainty. Also, the improvement in DSR or DVR has to be at the sacrifice of the other one. Recently, Westerweel *et al.* (2013) reviewed the state-of-art development of PIV technique. By that, the size of the recording medium had reached 11-14 Mpixel, and some advanced PIV interrogation algorithms had reduced c_τ down to 0.05-0.2. But, both parameters appeared to be reaching their limit. On the other hand, the total error could result from many sources such as lens aberration, image distortion, pixel fill-factor and so on. Unless a revolution occurs in manufacturing technology, significant advances in PIV technology require fundamental changes in the conventional dual-pulsed system design.

Multi-pulse PIV is a recently proposed, novel technique (Haranandani, 2011; Westerweel *et al.*, 2013) that is intended to better resolve the particle motion and consequently enhance the velocity measurement accuracy and allow direct measurement of acceleration. By adding one or two additional pulses and recording the particle location at more than two time instants, it is possible to fit a polynomial (second order or higher) representing the trajectory and estimate the particle velocity and acceleration using the temporal derivative. Furthermore, an optimized t, the time along the trajectory, can be found (Haranandani, 2011) that will achieve minimum combined error in position and velocity, assuming the real trajectory of the particle is a locally circular path. In Haranandani's study, he also compared the error in position and velocity between triple-pulse and conventional dual-pulse PTV, and showed that the triple-pulse method can substantially improve the position and velocity accuracy when the particle moves a long curved path and exhibits strong tangential acceleration. Multi-pulse methods achieve better spatial resolution by more accurately assigning a Lagrangian vector, i.e. the velocity vector, to a Eulerian point in the fluid. They also account for the temporal and spatial variations of the particle veloc-

ity between pulses, whereas dual-pulsed PIV assumes constant velocity between the two exposures. As pointed out by Boillot and Prasad (1996), one of the constraints in increasing DVR is that the velocity variation increases as Δt increases, making the constant velocity assumption less accurate. In principle, the error due to acceleration can be reduced by multi-pulse method, making improvements of DVR appear promising. Estimates of acceleration also offer the possibility of correcting for particle slip in highly accelerated flows. Without knowledge of the acceleration, it must be assumed that particles have zero slip so that the Eulerian velocity $\boldsymbol{u}[\boldsymbol{x}_p(t), t]$ can be represented by the Lagrangian velocity of the particle, if the Δt is short enough,

$$\boldsymbol{u}[\boldsymbol{x}_p(t), t] \cong \boldsymbol{v}_p(t) \cong \frac{\Delta \boldsymbol{x}_p}{\Delta t} = \frac{\boldsymbol{x}_p(t + \Delta t) - \boldsymbol{x}_p(t)}{\Delta t}. \tag{1.6}$$

However, if the particle dynamic, i.e. the inertias of the particle and the fluid are taken into account, a more detailed version of Equation (1.6) is needed. According to Adrian and Westerweel (2011),

$$\boldsymbol{u}[\boldsymbol{x}_p(t), t] = \frac{\Delta \boldsymbol{x}_p}{\Delta t} - \dot{\boldsymbol{v}}_p(t)\frac{\Delta t}{2} + [\dot{\boldsymbol{v}}_p(t) - \boldsymbol{b}]\tau_p + O(\Delta t^2) \tag{1.7}$$

where $\boldsymbol{b}$ is the particle body force per unit mass, and τ_p is the particle momentum response time. The second term is the aforementioned velocity variation between pulses. The third term represents the particle lag and particle drift caused by body forces such as gravity. This expression implies that by measuring particle acceleration with multi-pulse technique, we could actually refine the fluid velocity measurement accuracy by accounting for velocity variation and particle slip. In addition, as the Navier-Stokes equation indicates, acceleration measurement by multi-pulse scheme can also make the direct estimation of the fluid pressure and viscous forces possible.

Various schemes for multiple recordings of the particle locations have been investigated and implemented. Keane and Adrian (1991) numerically studied the optimized

rules for multiple pulsed PIV systems. They concluded that as the pulse number increases, the correlation quality improves by effectively increasing the image density. This implies that we may be able to use lower seeding density and still achieve good correlation with multiple pulses, which will benefit super-resolution analysis. They also found that with multiple pulses, the quality of the correlation became less sensitive to the velocity gradient, a factor that often limits dual-pulsed systems.

Time-resolved PIV (TR-PIV) is now a popular tool for investigating highly unsteady flows. The combination of high-repetition-rate Nd:YLF lasers and high-frame-rate CMOS cameras allows the acquisition frequency of TR-PIV to reach up to 5 kHz with 1024×1024-pixel images (Westerweel *et al.*, 2013). Compared to low-repetition-rate Nd:YAG lasers, Nd:YLF lasers used in TR-PIV typically has lower energy output. As an example, Nd:YLF laser can generate 10-20 mJ laser pulses at 1 kHz pulse rate, while only 1-2 mJ for pulse rate of 10 kHz (Adrian and Westerweel, 2011). Additionally, CMOS camera generally has larger pixel size and higher noise. These two factors together contribute to the reduction of the quality of TR-PIV particle images. As a compensation, some interrogation algorithms utilizing coherent particle patterns in consecutive frames were developed to try to obtain strong correlation signal. Examples are multiframe PIV (Hain and Kähler, 2007), multi-frame pyramid correlation (Sciacchitano *et al.*, 2012), fluid-tracking correlation (Lynch and Scarano, 2013) and so on. The acquisition rate of current TR-PIV is considered enough for most water flows. For example, Scarano *et al.* (2010) conducted a decent TR-PIV measurement of circular and chevron jet transition at acquisition rate 1 kHz with the jet exit velocity $0.45m/s$. However for most air flows with flow speed typically being 10 to 100 m/s, TR-PIV is considered not sufficient to resolve the flow and thus not capable to accurately measure acceleration. In order to record images at multiple times with small enough Δt, Christensen and Adrian (2002) developed a 4-pulse system with two

dual-pulsed lasers and 2 PIV CCD cameras. Cross-polarized light sheet is formed and the particle images are separated to each camera using cross-polarized filter in front of the imaging optics. This work is a valuable pioneer of multi-pulse PIV in measuring instantaneous acceleration field discussed in present paper.

In present work, the optimization and the accuracy assessment of multi-pulse PTV is a continuation of the investigation by Haranandani (2011). Farrugia et $al.$ (1995) performed an PIV experiment using three pulses and compute the displacement field using third-order auto-correlation. To distinguish the flow direction, he set the time separation ratio α[1] to be 1/3. Haranandani (2011) used $\alpha = 1/3$ in his work as well. Here, instead, triple-pulse and quadruple-pulse PTV with equal time spacing are considered since the flow direction is automatically indicated in cross-correlation analysis. The optimization regarding the minimum combined error in position, velocity and acceleration is achieved for triple-pulse and quadruple-pulse. Experiment was conducted on a circular impinging air jet. A 8-pulse laser system consisted of 4 dual-cavity lasers is used in combination of a 4-imaging-channel beam-splitting camera to achieve satisfactory temporal resolution for high-speed air flow. The ensemble-averaged centerline acceleration profiles, obtained by dual-pulse PIV and triple-pulse PIV respectively, are compared to test capability of triple-pulse PIV in measuring acceleration.

---

[1]Here α is defined as $(t_2 - t_1)/(t_3 - t_1)$, where t_1,t_2, and t_3 are time instants at which particles are recorded.

TRIPLE- AND QUADRUPLE-PULSE PTV SIMULATION WITH PARTICLE

DISPLACEMENT RANGE CONSTRAINT

In this chapter, the methodology of calculating particle trajectory, velocity and acceleration by triple- and quadruple-pulse PTV is presented. I will also discuss the way of setting reference trajectory and consequently computing errors in position, velocity, and acceleration. The optimizations for triple- and quadruple-pulse PTV is achieved in the sense of minimizing combined position, velocity and acceleration errors. For this chapter, all evaluations are considered within the particle displacement range that is considered to be optimal for most current PIV/PTV measurements. Usually the particle displacement is set to be 8-15 pixels for dual-pulse PIV measurements, which accounts for the trade-off between DVR and DSR, and avoids strong loss-of-pair effect due to out-of-plane motion. For multi-pulse measurements in this study, it is reasonable to extend the range by a factor of 2 or 3. In next chapter, the evaluation will show the potential gain if the constraint on particle displacement range is substantially released. For completeness, some contents overlap with the work by Haranandani (2011).

2.1   Optimization of triple-pulse PTV

2.1.1   Simulation method

Think of an arbitrary point out of a particle long-term trajectory. A small enough segment around the point can always be approximated as a segment of a local circle

with the radius being the local radius of curvature R^1. Thus, it is reasonable to assume that a particle travels along a local circle with in short Δt. Suppose the laser is pulsed at time t_i and the true particle locations are $\boldsymbol{X}_{pi}{}^2$, $i = 1, 2, 3$. To simplify the analysis, all t_i are referred to the first pulse and denoted by primes, i.e.

$$t_i' = t_i - t_1, \quad i = 1, 2, 3. \tag{2.1}$$

if we use α to represent the location of the second pulse, we get

$$t_1' = 0, \quad t_2' = \alpha \Delta t, \quad t_3' = \Delta t. \tag{2.2}$$

Following the prime convention, the true particle trajectory is mathematically described as the following,

$$\boldsymbol{X}_p(t') = \boldsymbol{X}_{p1} + [R - Rcos\vartheta(t')]\boldsymbol{i} + Rsin\vartheta(t')\boldsymbol{j}, \tag{2.3}$$

with $t' \in [0, \Delta t]$. Then $\boldsymbol{X}_{pi}$ are related to $\boldsymbol{X}_p(t')$ by

$$\boldsymbol{X}_{p1} = \boldsymbol{X}_p(t_1') = \boldsymbol{X}_p(0) = \boldsymbol{X}_{p1} \tag{2.4a}$$

$$\boldsymbol{X}_{p2} = \boldsymbol{X}_p(t_2') = \boldsymbol{X}_p(\alpha\Delta t) = \boldsymbol{X}_{p1} + [R - Rcos\vartheta(\alpha\Delta t)]\boldsymbol{i} + [Rsin\vartheta(\alpha\Delta t)]\boldsymbol{j} \tag{2.4b}$$

$$\boldsymbol{X}_{p3} = \boldsymbol{X}_p(t_3') = \boldsymbol{X}_p(\Delta t) = \boldsymbol{X}_{p1} + [R - Rcos\vartheta(\Delta t)]\boldsymbol{i} + [Rsin\vartheta(\Delta t)]\boldsymbol{j} \tag{2.4c}$$

If we also refer the trajectory (2.3) and particle locations (2.4) to $\boldsymbol{X}_{p1}$, then

$$\boldsymbol{X}_p'(t') = [R - Rcos\vartheta(t')]\boldsymbol{i} + Rsin\vartheta(t')\boldsymbol{j}, \tag{2.5}$$

and

$$\boldsymbol{X}_{p1}' = \boldsymbol{X}_{p1} - \boldsymbol{X}_{p1} = 0, \tag{2.6a}$$

$$\boldsymbol{X}_{p2}' = \boldsymbol{X}_{p2} - \boldsymbol{X}_{p1} = [R - Rcos\vartheta(\alpha\Delta t)]\boldsymbol{i} + [Rsin\vartheta(\alpha\Delta t)]\boldsymbol{j}, \tag{2.6b}$$

$$\boldsymbol{X}_{p3}' = \boldsymbol{X}_{p3} - \boldsymbol{X}_{p1} = [R - Rcos\vartheta(\Delta t)]\boldsymbol{i} + [Rsin\vartheta(\Delta t)]\boldsymbol{j}. \tag{2.6c}$$

---

[1]Here, R is defined on image plane.

[2]If the interrogation window size is small enough and the velocity gradient within the window is negligible, $\boldsymbol{X}_{pi}$ could also represent the centroid position of the particle group.

In equation (2.3), the angular displacement ϑ is modeled by the combination of an angular velocity term, $\dot{\vartheta}_0 t'$, and an angular acceleration term, $\frac{1}{2}\ddot{\vartheta}_0 t'^2$, i.e.

$$\vartheta(t') = \dot{\vartheta}_0 t' + \frac{1}{2}\ddot{\vartheta}_0 t'^2. \tag{2.7}$$

On the other hand, at each time instants t_i', we have a measured particle location with some measurement noise $\delta \boldsymbol{X}_{pi}$, which is treated as zero-mean (no bias error) random variables. If the measured locations are denoted by adding a subscript m, then we have

$$\boldsymbol{X}_{pi,m} = \boldsymbol{X}_{pi} + \delta \boldsymbol{X}_{pi}. \tag{2.8}$$

With these three particle location measurements, it is possible to fit a quadratic curve as an estimation of the true particle trajectory (2.3). The formula of the estimated trajectory is given by

$$\hat{\boldsymbol{X}}_p(t') = \left[1 - \frac{1+\alpha}{\alpha}\frac{t'}{\Delta t} + \frac{1}{\alpha}\frac{t'^2}{\Delta t^2}\right]\boldsymbol{X}_{p1,m} + \left[\frac{1}{\alpha(1-\alpha)}\frac{t'}{\Delta t} - \frac{1}{\alpha(1-\alpha)}\frac{t'^2}{\Delta t^2}\right]\boldsymbol{X}_{p2,m}$$
$$+ \left[-\frac{\alpha}{1-\alpha}\frac{t'}{\Delta t} + \frac{1}{1-\alpha}\frac{t'^2}{\Delta t^2}\right]\boldsymbol{X}_{p3,m}. \tag{2.9}$$

which is organized as the linear interpolation of measured particle locations. Additionally, the velocity and acceleration estimations are obtained by taking derivatives of the trajectory estimation (2.9):

$$\dot{\hat{\boldsymbol{X}}}_p(t') = \left[-\frac{1+\alpha}{\alpha} + \frac{2}{\alpha}\frac{t'}{\Delta t}\right]\frac{\boldsymbol{X}_{p1,m}}{\Delta t} + \left[\frac{1}{\alpha(1-\alpha)} - \frac{2}{\alpha(1-\alpha)}\frac{t'}{\Delta t}\right]\frac{\boldsymbol{X}_{p2,m}}{\Delta t}$$
$$+ \left[-\frac{\alpha}{1-\alpha} + \frac{2}{1-\alpha}\frac{t'}{\Delta t}\right]\frac{\boldsymbol{X}_{p3,m}}{\Delta t} \tag{2.10}$$

and

$$\ddot{\hat{\boldsymbol{X}}}_p(t') = \frac{2}{\alpha}\frac{\boldsymbol{X}_{p1,m}}{\Delta t^2} - \frac{2}{\alpha(1-\alpha)}\frac{\boldsymbol{X}_{p2,m}}{\Delta t^2} + \frac{2}{1-\alpha}\frac{\boldsymbol{X}_{p3,m}}{\Delta t^2} \tag{2.11}$$

Equation (2.3) and (2.9) actually lead to method of analyzing particle position RMS error σ_x, which is defined as

$$\sigma_{X_p}^2(t') \triangleq \langle \left|\hat{\boldsymbol{X}}_p(t') - \boldsymbol{X}_p(t')\right|^2 \rangle. \tag{2.12}$$

Similarly, we can also calculate the velocity RMS error, σ_v, and the acceleration RMS error, σ_a, using (2.10) and (2.11):

$$\sigma_v^2(t') \triangleq \langle \left| \dot{\hat{\boldsymbol{X}}}_p(t') - \dot{\boldsymbol{X}}_p(t') \right|^2 \rangle, \tag{2.13}$$

$$\sigma_a^2(t') \triangleq \langle \left| \ddot{\hat{\boldsymbol{X}}}_p(t') - \ddot{\boldsymbol{X}}_p(t') \right|^2 \rangle. \tag{2.14}$$

For generality, we normalize the position RMS error by the local radius of curvature, R; normalize the velocity RMS error by the full scale velocity, $R(\dot{\vartheta}_0 + \ddot{\vartheta}_0 \Delta t)$; normalize the acceleration RMS error by the full scale acceleration, $R\sqrt{\dot{\vartheta}_0^4 + \ddot{\vartheta}_0^2}$, and denote the normalized RMS errors by bars on top, i.e.

$$\bar{\sigma}_{X_p} = \frac{\sigma_{X_p}}{R} \tag{2.15}$$

$$\bar{\sigma}_v = \frac{\sigma_v}{R(\dot{\vartheta}_0 + \ddot{\vartheta}_0 \Delta t)} \tag{2.16}$$

$$\bar{\sigma}_a = \frac{\sigma_a}{R\sqrt{\dot{\vartheta}_0^4 + \ddot{\vartheta}_0^2}} \tag{2.17}$$

Using (2.4), (2.7), (2.8), (2.9) for $\hat{\boldsymbol{X}}_p(t')$, and (2.3), (2.7) for $\boldsymbol{X}_p(t')$, and assuming the locating noise for different particles are zero-mean and statistically independent, i.e.

$$\langle \delta \boldsymbol{X}_{pi} \rangle = \boldsymbol{0}, \qquad \langle \delta \boldsymbol{X}_{pi} \cdot \delta \boldsymbol{X}_{pj} \rangle = \langle |\delta \boldsymbol{X}_p|^2 \rangle \delta_{ij}, \tag{2.18}$$

the nomarlized position RMS error (2.15) is given as the following:

$$
\begin{aligned}
\bar{\sigma}^2_{X_p} = \Bigg(&\left[\frac{1}{\alpha(1-\alpha)} \frac{t'}{\Delta t} - \frac{1}{\alpha(1-\alpha)} \frac{t'^2}{\Delta t^2} \right] \left[1 - \cos(\dot{\vartheta}_0 \alpha \Delta t + \frac{1}{2} \ddot{\vartheta}_0 \alpha^2 \Delta t^2) \right] \\
&- \left[\frac{\alpha}{1-\alpha} \frac{t'}{\Delta t} - \frac{1}{1-\alpha} \frac{t'^2}{\Delta t^2} \right] \left[1 - \cos(\dot{\vartheta}_0 \Delta t + \frac{1}{2} \ddot{\vartheta}_0 \Delta t^2) \right] \\
&- \left[1 - \cos(\dot{\vartheta}_0 t' + \frac{1}{2} \ddot{\vartheta}_0 t'^2) \right] \Bigg)^2 \\
+ \Bigg(&\left[\frac{1}{\alpha(1-\alpha)} \frac{t'}{\Delta t} - \frac{1}{\alpha(1-\alpha)} \frac{t'^2}{\Delta t^2} \right] \sin(\dot{\vartheta}_0 \alpha \Delta t + \frac{1}{2} \ddot{\vartheta}_0 \alpha^2 \Delta t^2) \\
&- \left[\frac{\alpha}{1-\alpha} \frac{t'}{\Delta t} - \frac{1}{1-\alpha} \frac{t'^2}{\Delta t^2} \right] \sin(\dot{\vartheta}_0 \Delta t + \frac{1}{2} \ddot{\vartheta}_0 \Delta t^2) - \sin(\dot{\vartheta}_0 t' + \frac{1}{2} \ddot{\vartheta}_0 t'^2) \Bigg)^2 \\
+ \Bigg(&\left[1 - \frac{1+\alpha}{\alpha} \frac{t'}{\Delta t} + \frac{1}{\alpha} \frac{t'^2}{\Delta t^2} \right]^2 + \left[\frac{1}{\alpha(1-\alpha)} \frac{t'}{\Delta t} - \frac{1}{\alpha(1-\alpha)} \frac{t'^2}{\Delta t^2} \right]^2 \\
&+ \left[-\frac{\alpha}{1-\alpha} \frac{t'}{\Delta t} + \frac{1}{1-\alpha} \frac{t'^2}{\Delta t^2} \right]^2 \Bigg) \frac{\langle |\delta \boldsymbol{X}_p|^2 \rangle}{R^2}.
\end{aligned}
\tag{2.19}
$$

Likewise, the formulae for the normalized velocity RMS error and acceleration RMS error are given as the following:

$$
\begin{aligned}
\bar{\sigma}^2_v = \Bigg(&\left[\frac{1}{\alpha(1-\alpha)} \frac{1}{\dot{\vartheta}_0 \Delta t} - \frac{2}{\alpha(1-\alpha)} \frac{t'}{\Delta t} \frac{1}{\dot{\vartheta}_0 \Delta t} \right] \left[1 - \cos(\dot{\vartheta}_0 \alpha \Delta t + \frac{1}{2} \ddot{\vartheta}_0 \alpha^2 \Delta t^2) \right] \\
&- \left[\frac{\alpha}{1-\alpha} \frac{1}{\dot{\vartheta}_0 \Delta t} - \frac{2}{1-\alpha} \frac{t'}{\Delta t} \frac{1}{\dot{\vartheta}_0 \Delta t} \right] \left[1 - \cos(\dot{\vartheta}_0 \Delta t + \frac{1}{2} \ddot{\vartheta}_0 \Delta t^2) \right] \\
&- \left[\sin(\dot{\vartheta}_0 t' + \frac{1}{2} \ddot{\vartheta}_0 t'^2)(1 + \frac{\ddot{\vartheta}_0 t'}{\dot{\vartheta}_0}) \right] \Bigg)^2 \frac{1}{(1 + \ddot{\vartheta}_0 \Delta t / \dot{\vartheta}_0)^2} \\
+ \Bigg(&\left[\frac{1}{\alpha(1-\alpha)} \frac{1}{\dot{\vartheta}_0 \Delta t} - \frac{2}{\alpha(1-\alpha)} \frac{t'}{\Delta t} \frac{1}{\dot{\vartheta}_0 \Delta t} \right] \sin(\dot{\vartheta}_0 \alpha \Delta t + \frac{1}{2} \ddot{\vartheta}_0 \alpha^2 \Delta t^2) \\
&- \left[\frac{\alpha}{1-\alpha} \frac{1}{\dot{\vartheta}_0 \Delta t} - \frac{2}{1-\alpha} \frac{t'}{\Delta t} \frac{1}{\dot{\vartheta}_0 \Delta t} \right] \sin(\dot{\vartheta}_0 \Delta t + \frac{1}{2} \ddot{\vartheta}_0 \Delta t^2) \\
&- \left[\cos(\dot{\vartheta}_0 t' + \frac{1}{2} \ddot{\vartheta}_0 t'^2)(1 + \frac{\ddot{\vartheta}_0 t'}{\dot{\vartheta}_0}) \right] \Bigg)^2 \frac{1}{(1 + \ddot{\vartheta}_0 \Delta t / \dot{\vartheta}_0)^2} \\
+ \Bigg(&\left[-\frac{1+\alpha}{\alpha} \frac{1}{\dot{\vartheta}_0 \Delta t} + \frac{2}{\alpha} \frac{t'}{\Delta t} \frac{1}{\dot{\vartheta}_0 \Delta t} \right]^2 + \left[\frac{1}{\alpha(1-\alpha)} \frac{1}{\dot{\vartheta}_0 \Delta t} - \frac{2}{\alpha(1-\alpha)} \frac{t'}{\Delta t} \frac{1}{\dot{\vartheta}_0 \Delta t} \right]^2 \\
&+ \left[-\frac{\alpha}{1-\alpha} \frac{1}{\dot{\vartheta}_0 \Delta t} + \frac{2}{1-\alpha} \frac{t'}{\Delta t} \frac{1}{\dot{\vartheta}_0 \Delta t} \right]^2 \Bigg) \frac{1}{(1 + \ddot{\vartheta}_0 \Delta t / \dot{\vartheta}_0)^2} \frac{\langle |\delta \boldsymbol{X}_p|^2 \rangle}{R^2},
\end{aligned}
\tag{2.20}
$$

$$\bar{\sigma}_a^2 = \frac{1}{1 + \dot{\vartheta}_0^4/\ddot{\vartheta}_0^2} \left(\left[-\frac{2}{\alpha(1-\alpha)} \frac{1}{\ddot{\vartheta}_0 \Delta t^2} \right] \left[1 - \cos(\dot{\vartheta}_0 \alpha \Delta t + \frac{1}{2}\ddot{\vartheta}_0 \alpha^2 \Delta t^2) \right] \right.$$

$$- \left[-\frac{2}{1-\alpha} \frac{1}{\ddot{\vartheta}_0 \Delta t^2} \right] \left[1 - \cos(\dot{\vartheta}_0 \Delta t + \frac{1}{2}\ddot{\vartheta}_0 \Delta t^2) \right]$$

$$\left. - \left[\cos(\dot{\vartheta}_0 t' + \frac{1}{2}\ddot{\vartheta}_0 t'^2)(\frac{\dot{\vartheta}_0^2}{\ddot{\vartheta}_0} + \ddot{\vartheta}_0 t'^2 + 2\dot{\vartheta}_0 t') + \sin(\dot{\vartheta}_0 t' + \frac{1}{2}\ddot{\vartheta}_0 t'^2) \right] \right)^2$$

$$+ \frac{1}{1 + \dot{\vartheta}_0^4/\ddot{\vartheta}_0^2} \left(\left[-\frac{2}{\alpha(1-\alpha)} \frac{1}{\ddot{\vartheta}_0 \Delta t^2} \right] \sin(\dot{\vartheta}_0 \alpha \Delta t + \frac{1}{2}\ddot{\vartheta}_0 \alpha^2 \Delta t^2) \right.$$

$$- \left[-\frac{2}{1-\alpha} \frac{1}{\ddot{\vartheta}_0 \Delta t^2} \right] \sin(\dot{\vartheta}_0 \Delta t + \frac{1}{2}\ddot{\vartheta}_0 \Delta t^2)$$

$$\left. - \left[-\sin(\dot{\vartheta}_0 t' + \frac{1}{2}\ddot{\vartheta}_0 t'^2)(\frac{\dot{\vartheta}_0^2}{\ddot{\vartheta}_0} + \ddot{\vartheta}_0 t'^2 + 2\dot{\vartheta}_0 t') + \cos(\dot{\vartheta}_0 t' + \frac{1}{2}\ddot{\vartheta}_0 t'^2) \right] \right)^2$$

$$+ \frac{1}{1 + \dot{\vartheta}_0^4/\ddot{\vartheta}_0^2} \left(\left[\frac{2}{\alpha} \frac{1}{\ddot{\vartheta}_0 \Delta t^2} \right]^2 + \left[-\frac{2}{\alpha(1-\alpha)} \frac{1}{\ddot{\vartheta}_0 \Delta t^2} \right]^2 + \left[\frac{2}{1-\alpha} \frac{1}{\ddot{\vartheta}_0 \Delta t^2} \right]^2 \right) \frac{\langle |\delta \boldsymbol{X}_p|^2 \rangle}{R^2}$$

$$(2.21)$$

In Equation (2.19) to (2.21), the first two square terms are respect interpolation errors for $\boldsymbol{i}$ and $\boldsymbol{j}$ component. The third term represents the error due to inaccurate particle center location, i.e. $\delta \boldsymbol{X}_{pi}$.

As discussed above, PIV measurements assign Lagrangian quantities, such as particle velocities and accelerations, to Eulerian positions in the fluid. The accuracy of the Euleraian position determination affects the total performance of the PIV system. In present analysis, we define two cost funtions for velocity and acceleration measurment, respectively, to account for the position error simultaneously. The velocity cost function, K_v, is defined as

$$K_v \triangleq \sqrt{\eta \bar{\sigma}_{X_p}^2 + (1 - \eta)\bar{\sigma}_v^2}, \quad (2.22)$$

where η is a wighting factor taken to be 0.5. Similarly, the acceleration cost function is defined as

$$K_a \triangleq \sqrt{\eta \bar{\sigma}_{X_p}^2 + (1 - \eta)\bar{\sigma}_a^2}. \quad (2.23)$$

It is noted that the RMS errors are functions of t', and in the meanwhile depend on parameters including $\dot{\vartheta}_0$, $\ddot{\vartheta}_0$, and $\langle|\delta\boldsymbol{X}_p|^2\rangle$. The purpose of current analysis is to find the optimized t' that minimizing the cost functions for wide ranges of different parameters. Three dimensionless parameters are considered, which are normalized particle displacement, $R\dot{\vartheta}_0\Delta t/R = \dot{\vartheta}_0\Delta t$, acceleration factor, $\frac{1}{2}\ddot{\vartheta}_0\Delta t^2/\dot{\vartheta}_0\Delta t = \ddot{\vartheta}_0\Delta t/2\dot{\vartheta}_0$, and normalized particle locating noise, $\sqrt{\langle|\delta\boldsymbol{X}_p|^2\rangle}\Big/R$. To set a reasonable range for the noise level, here we need consider some numbers encountered in common PIV practice. The RMS locating noise $\sqrt{\langle|\delta\boldsymbol{X}_p|^2\rangle}$ is proportional to the particle diameter (Adrian and Westerweel, 2011). Typically, the particle diameter is optimized to be 2-3 pixels, and the noise is 5%-20% of the diameter. This means that the locating noise is typically around 0.1-0.6 pixels. On the other hand, the fluid motion could have quite diverse radii of curvature — from 20-30 pixels near the center of a vortex to hundreds or thousands pixels of laminar Stokes flows. This implies that the noise level $\sqrt{\langle|\delta\boldsymbol{X}_p|^2\rangle}\Big/R$ can vary over many orders of magnitude and it is dominated by R. Furthermore, if we consider the particle displacement only within the optimal range adopted in most PIV measurements, the normalized displacement range, approximated as the ratio of the displacement to the radius of curvature, is associated with the noise level. In this chapter, the cost function is evaluated with different noise levels by setting the normalized displacement range accordingly. Table 2.1 lists various R and the corresponding noise levels, assuming 0.3 pixels as a representative locating error. The last column lists the corresponding normalized displacement ranges, assuming the particle displacement is 10-30 pixels. These ranges are considered as the optimal in triple-pulse PTV/PIV measurements. Table 2.2 summarizes the parameter space of the triple-pulse PTV simulation.

$\sqrt{\langle\|\delta\boldsymbol{X}_p\|^2\rangle}$	R	$\sqrt{\langle\|\delta\boldsymbol{X}_p\|^2\rangle}\Big/R$	$\dot{\vartheta}_0\Delta t$
(pix)	(pix)		
	30	1.0%	0.33-1.0
	40	0.75%	0.25-0.75
	60	0.5%	0.17-0.5
0.3	200	0.15%	0.05-0.15
	400	0.075%	0.025-0.075
	1000	0.03%	0.01-0.03

Table 2.1: List of noise levels and corresponding normalized displacements with wide range of the radius of curvature. Assume particle displacement is 10-30 pixels.

d_τ	22.5 μm
α	0.5
$t'/\Delta t$	[0, 1]
$\ddot{\vartheta}_0\Delta t/2\dot{\vartheta}_0$	-0.3, -0.1, 0, 0.2, 0.4
$\sqrt{\langle\|\delta\boldsymbol{X}_p\|^2\rangle}\Big/R$	0.03%, 0.075%, 0.15%, 0.5%, 0.75%, 1.0%
$\dot{\vartheta}_0\Delta t$	Corresponds to the noise level, see Table 2.1

Table 2.2: Parameter space for triple-pulse PTV simulation with particle displacement range constraint

2.1.2 Simulation results of velocity measurement

The simulation is carried out using parameters specified in Table 2.2. For each combination of $\ddot{\vartheta}_0\Delta t/2\dot{\vartheta}_0$ and $\sqrt{\langle\|\delta\boldsymbol{X}_p\|^2\rangle}\Big/R$, the 2-D contour plot of K_v and K_a are generated over $t'/\Delta t \in [0, 1]$ and the corresponding range of $\dot{\vartheta}_0\Delta t$. In other words, the cost function K_v and K_a are investigated over a 4-D space spanned by $t'/\Delta t$, $\dot{\vartheta}_0\Delta t$, $\ddot{\vartheta}_0\Delta t/2\dot{\vartheta}_0$, and $\sqrt{\langle\|\delta\boldsymbol{X}_p\|^2\rangle}\Big/R$, to find the optimized t' that minimizes K_v and K_a, respectively.
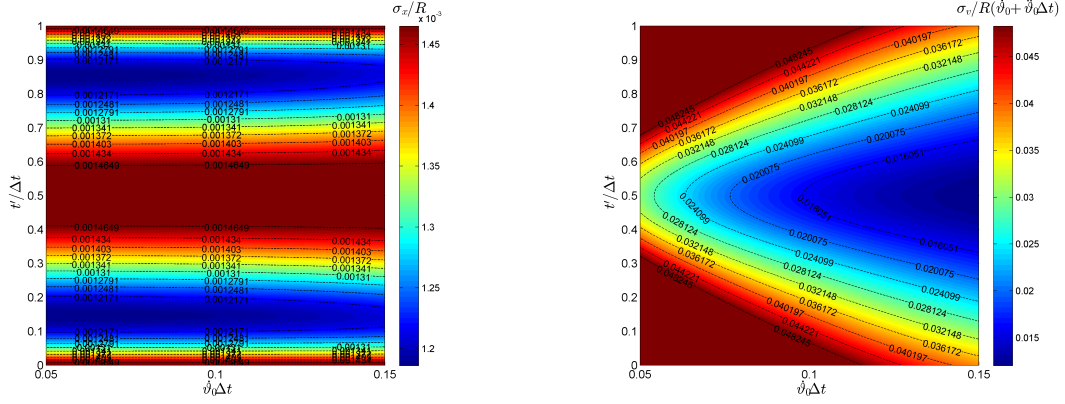
(a) position RMS error

(b) velocity RMS error
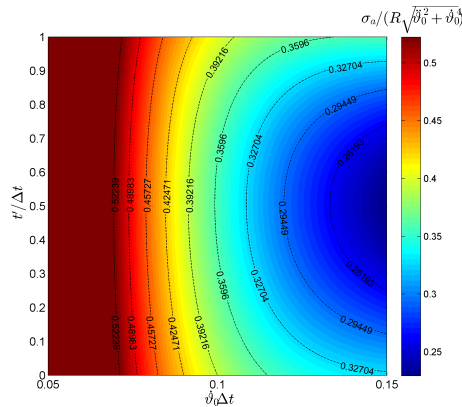
(c) acceleration RMS error

Figure 2.1: Triple-pulse normalized RMS error in (a) position, (b) velocity, and (c) acceleration with acceleration factor 0.2 and noise level 0.15%.

Figure 2.1 shows the normalized RMS errors in position, velocity and acceleration, defined in Equation (2.15) to (2.17), respectively. By comparing the contour values, it is found that the velocity error is about one order of magnitude greater than the position error, while the acceleration error is greater than velocity error by another order of magnitude. This implies that the velocity cost function is dominated by the velocity error, and the acceleration cost function is dominated by the acceleration error. It is also found the $t'/\Delta t$ that minimizes the error is different for position, velocity and acceleration, which means we have to achieve the optimization for veloc-

ity and acceleration by sacrificing the position accuracy. However, since the position error is substantially small, the strategy of evaluating the cost function will still give reasonable optimizations.

The contour plots of velocity cost function K_v is shown in Figure 2.2 and 2.3. To present 4-D data on 2-D plane, the 2-D contour plots are organized into a plot array, in which the noise level varies along the horizontal direction and the acceleration factor varies vertically. As a general observation, the topology of the plots preserves for almost all different acceleration factors and noise levels. For most cases, the cost function approaches the minimum at $t'/\Delta t = 0.5$ for wide range of normalized displacement $\dot{\vartheta}_0 \Delta t$. However, the contour plots of several cases appear quite different from others, which are associated with strong acceleration and high noise level. For example, the one with acceleration factor 0.4 and noise level 1.0% has the minimum at around $t'/\Delta t = 0.21$ and 0.78 for $\dot{\vartheta}_0 \Delta t > 0.4$. Similar topology shows when the acceleration factor is 0.4 and the noise level is 0.5% and 0.75%, and when the acceleration factor is 0.2 and the noise level is 0.75% and 1.0%, and when the acceleration factor is -0.3 and the noise level is 1.0%. These exceptions combined with other cases lead to the conclusion that, for flow exhibiting strong acceleration and close to the center of a vortex, $t'/\Delta t = 0.21$ and 0.78 will give more accurate velocity measurement, while for other regions one should generally use $t'/\Delta t = 0.5$. From the plot array, a good estimation of the exceptional range might be $\sqrt{\langle |\delta \boldsymbol{X}_p|^2 \rangle} \Big/ R \geqslant 0.75$ and $\left| \ddot{\vartheta}_0 \Delta t / 2 \dot{\vartheta}_0 \right| \geqslant 0.3$. Note that the radius of curvature and the acceleration factor can be estimated using the three measured particle positions. They are given as the following:

$$R \approx \frac{|\boldsymbol{X}_{p3,m} - \boldsymbol{X}_{p1,m}|}{2 sin \varphi} \tag{2.24}$$

where the φ is the angle between vector $(\boldsymbol{X}_{p3,m} - \boldsymbol{X}_{p2,m})$ and $(\boldsymbol{X}_{p1,m} - \boldsymbol{X}_{p2,m})$, and

$$\ddot{\vartheta}_0 \Delta t / 2 \dot{\vartheta}_0 \approx \frac{\alpha \varphi_{23} - (1 - \alpha) \varphi_{12}}{-\alpha^2 \varphi_{23} + (1 - \alpha^2) \varphi_{12}}, \tag{2.25}$$

16

where $\varphi_{23} = 2sin^{-1}(|\boldsymbol{X}_{p3,m} - \boldsymbol{X}_{p2,m}|/2R)$ is the central angle spanned by $\boldsymbol{X}_{p3,m}$ and $\boldsymbol{X}_{p2,m}$, and likewise for φ_{12}. Details of the derivation are provided in APPENDIX B.
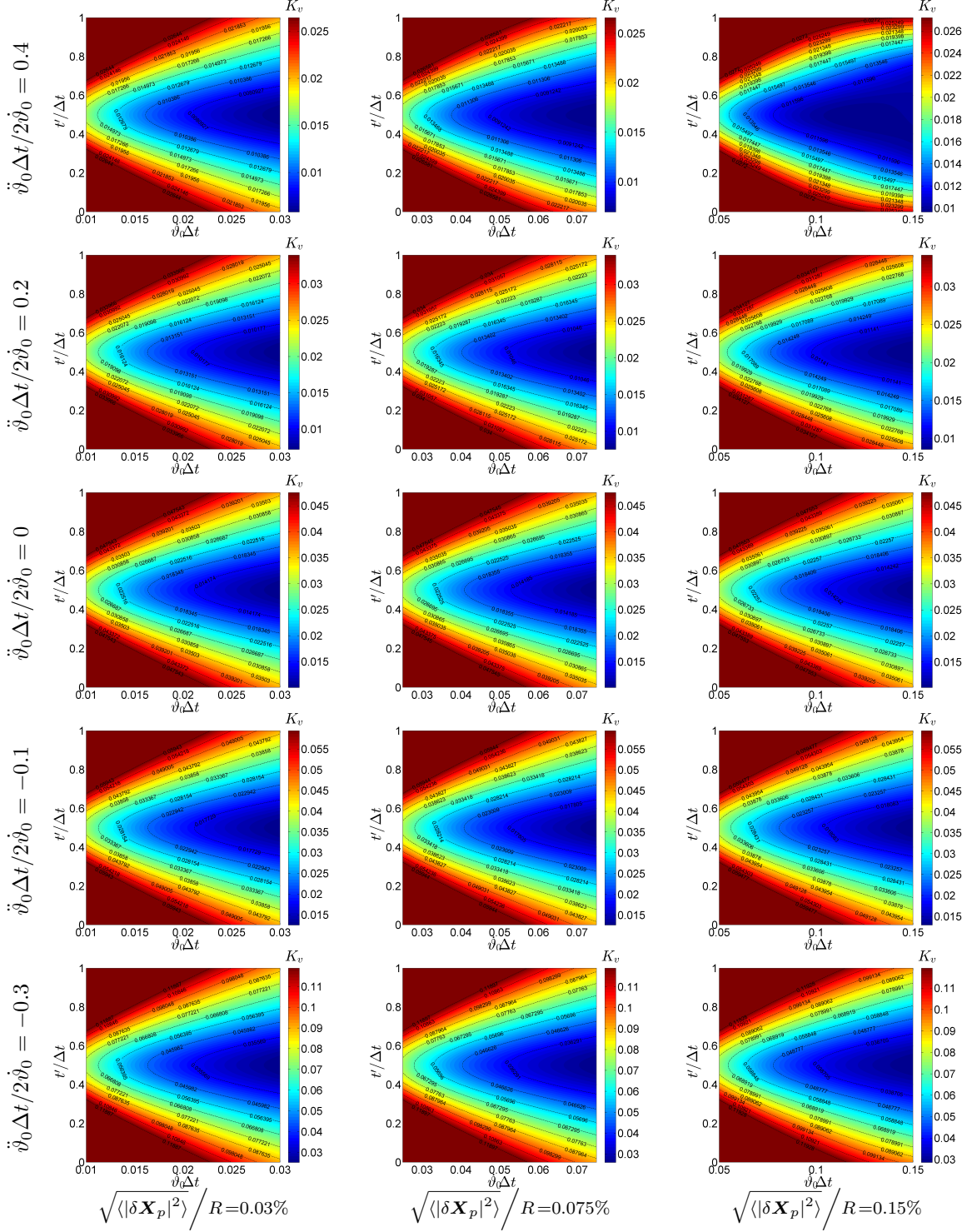
Figure 2.2: Triple-pulse velocity cost function with 0.03%, 0.075%, 0.15% noise level, with particle displacement range constraint

18
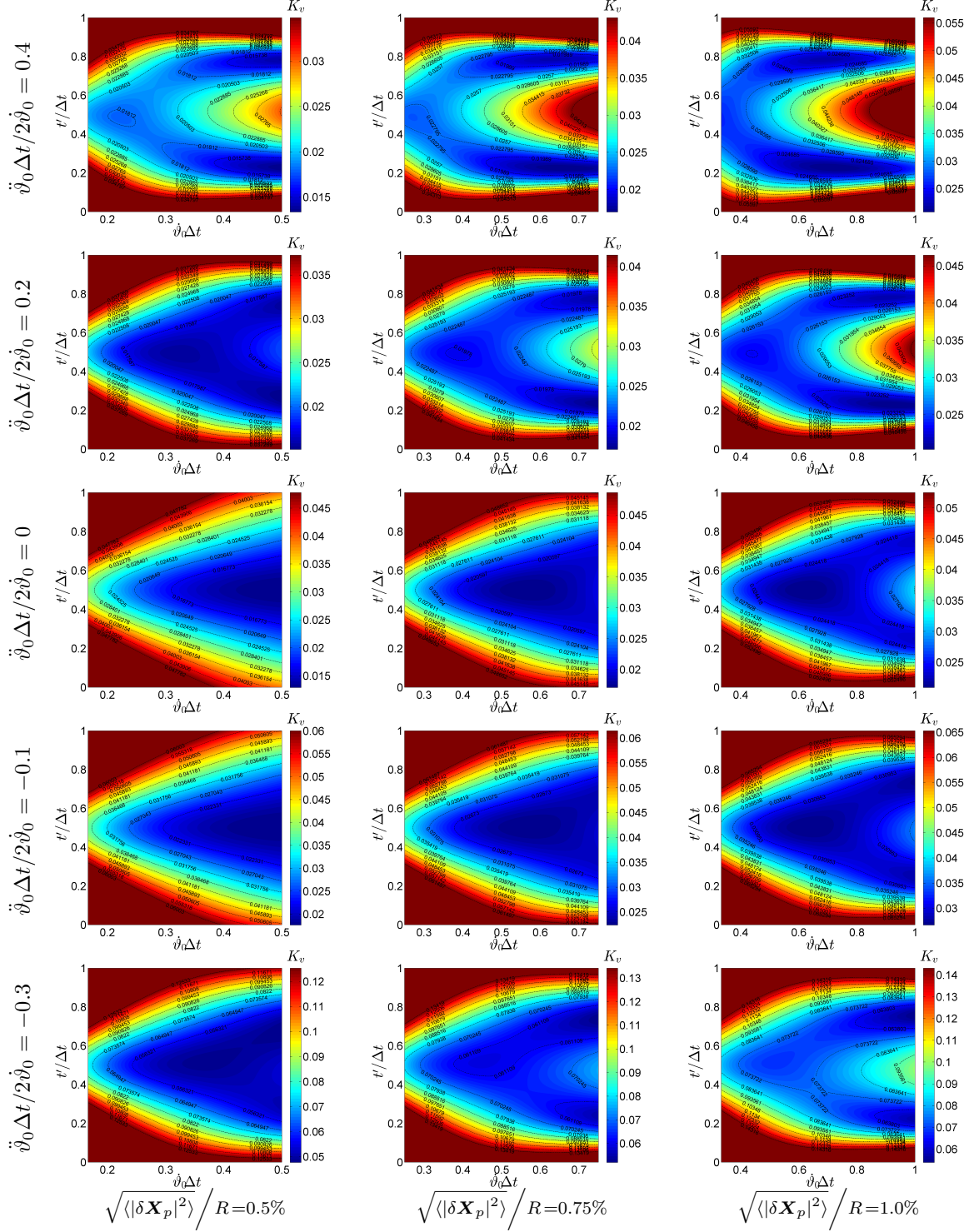
Figure 2.3: Triple-pulse velocity cost function with 0.5%, 0.75%, 1.0% noise level, with particle displacement range constraint
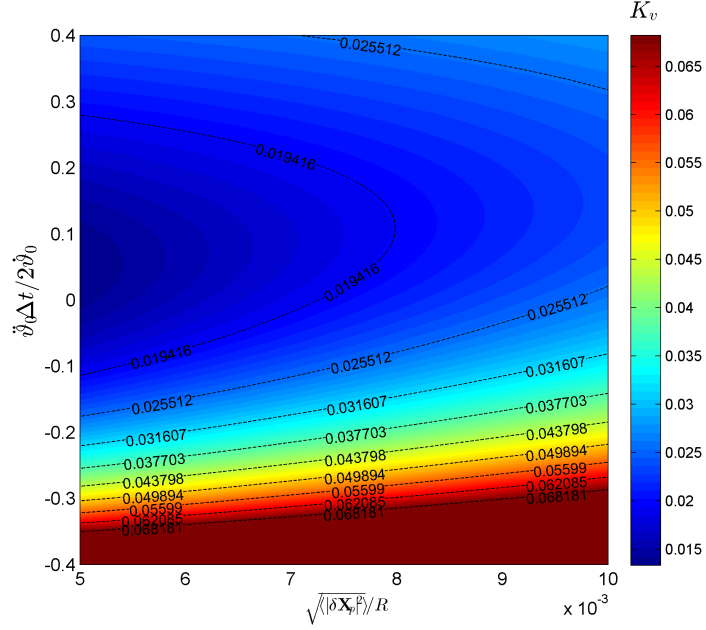
Figure 2.4: Triple-pulse velocity cost function plotted against acceleration factor and noise level, with $t'/\Delta t$=0.5 and $\dot{\vartheta}_0\Delta t$=0.4

Furthermore, in Figure 2.4, the velocity cost function is plotted against noise level (0.5%-1.0% horizontal axis) and acceleration factor (-0.4-0.4 vertical axis) with $t'/\Delta t$=0.5 and $\dot{\vartheta}_0\Delta t$=0.4. It shows that the error percentage with respect to the full scale velocity increases as the noise level increases and the acceleration factor magnitude increases. This implies that the triple-pulse velocity estimator that estimates the velocity in a linear way performs worse when strong velocity variation presents. It is also noticed that the error percentage change due to the increasing noise level becomes less rapid as the acceleration factor increases. In other words, the increase of noise level has less impact on the relative error percentage when the particle exhibits strong acceleration or deceleration.

20

2.1.3 Simulation results for acceleration measurement

Similarly, the acceleration cost function defined in Equation (2.23) is calculated and plotted in Figure 2.5 and 2.6. As shown clearly, $t'/\Delta t$=0.5 globally yields the optimized acceleration measurement.
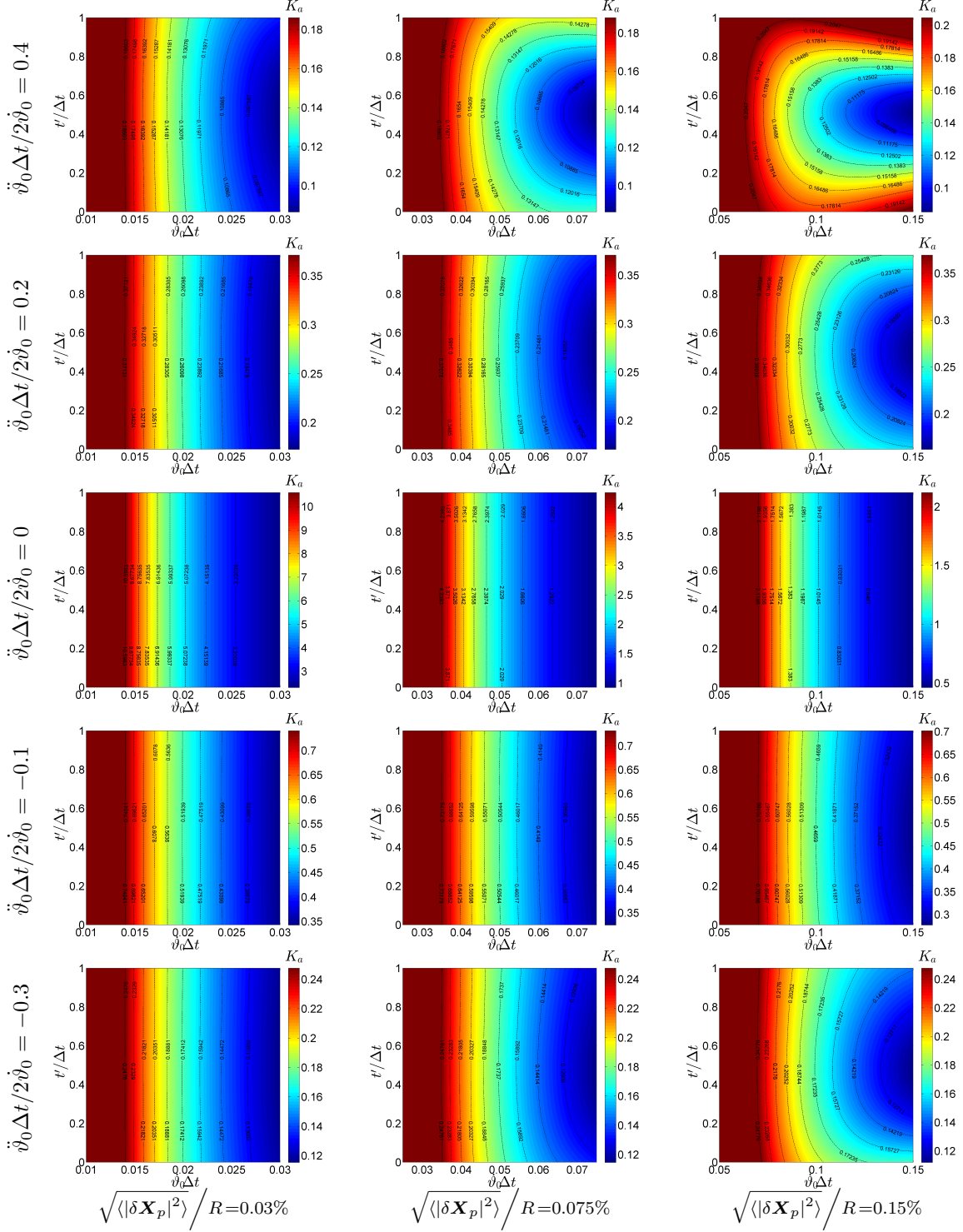
Figure 2.5: Triple-pulse acceleration cost function with 0.03%, 0.075%, 0.15% noise level, with particle displacement range constraint
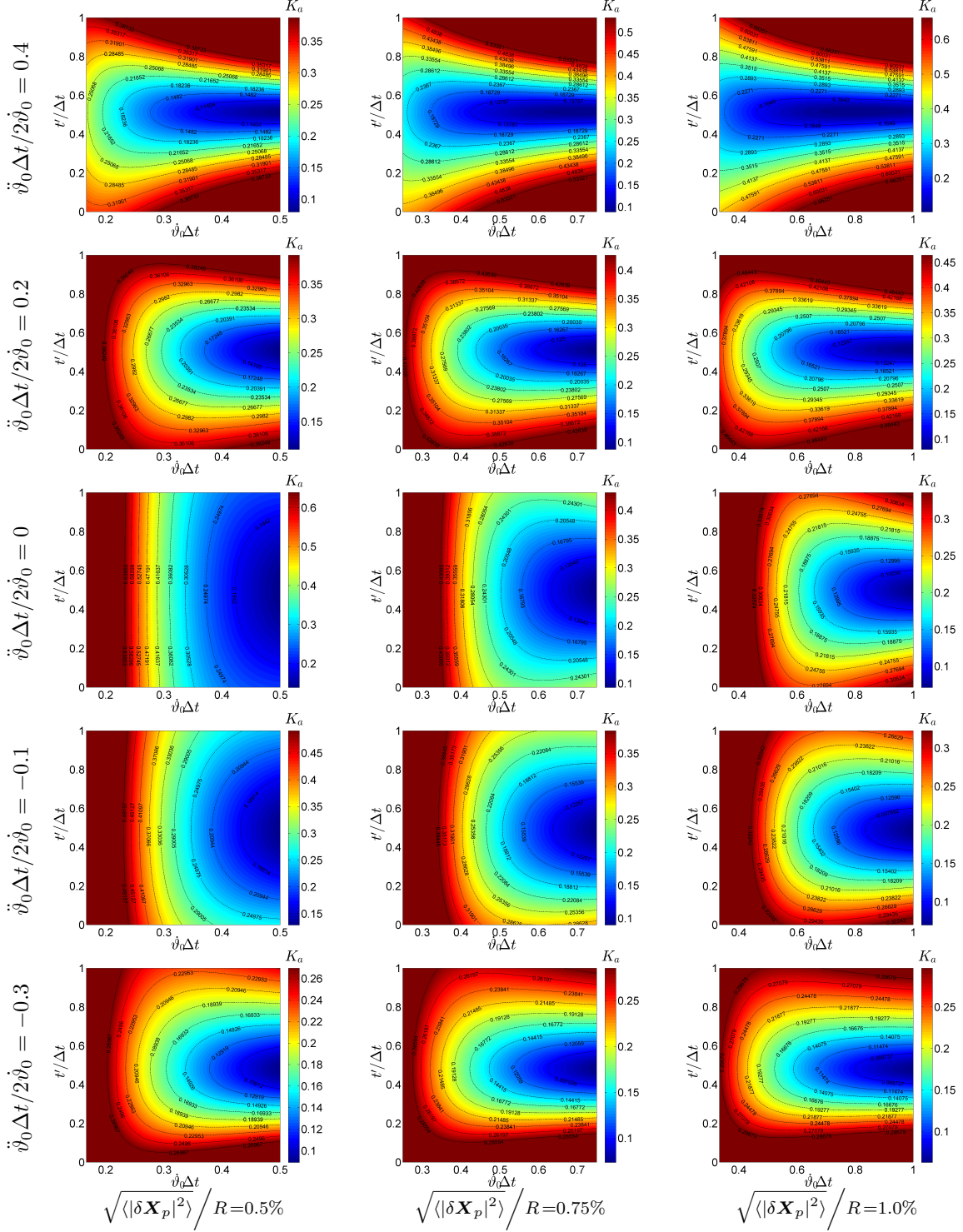
Figure 2.6: Triple-pulse acceleration cost function with 0.5%, 0.75%, 1.0% noise level, with particle displacement range constraint
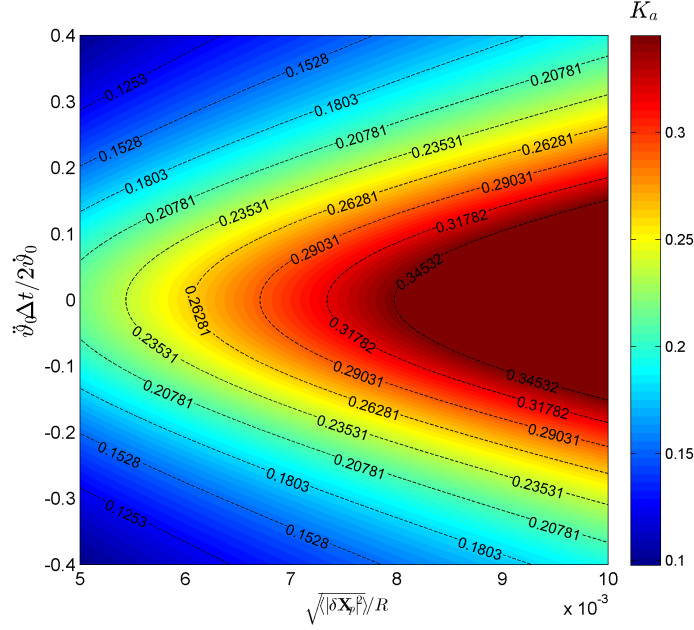
Figure 2.7: Triple-pulse acceleration cost function plotted against acceleration factor and noise level, with $t'/\Delta t$=0.5 and $\dot{\vartheta}_0\Delta t$=0.4

The acceleration cost function is also compared in terms of varying acceleration factor and noise level. Figure 2.7 shows the dependencies in the similar way as in Figure 2.4. The error percentage increases with the noise level increases. On the other hand, the error percentage becomes smaller for higher acceleration factor magnitude. That is to say, better acceleration measurement can be achieved when the flow accelerates more strongly. What is found to be different from velocity cost function is that the impact of the noise level on the error percentage becomes less significant as the acceleration factor magnitude grows, while this dependency is with respect to the acceleration factor for velocity cost function.

2.2 Optimization of quadruple-pulse PTV

2.2.1 Simulation method

Following the nomenclature defined in section 2.1.1, in quadruple pulse analysis we use β and γ to indicate the location of the 2$^{\text{nd}}$ and the 3$^{\text{rd}}$ pulse, i.e.

$$t'_1 = 0, \quad t'_2 = \beta \Delta t, \quad t'_3 = \gamma \Delta t, \quad t'_4 = \Delta t. \tag{2.26}$$

The particle locations in quadruple-pulse analysis are

$$\boldsymbol{X}'_{p1} = \boldsymbol{X}_{p1} - \boldsymbol{X}_{p1} = 0, \tag{2.27a}$$

$$\boldsymbol{X}'_{p2} = \boldsymbol{X}_{p2} - \boldsymbol{X}_{p1} = [R - Rcos\vartheta(\beta \Delta t)]\boldsymbol{i} + [Rsin\vartheta(\beta \Delta t)]\boldsymbol{j}, \tag{2.27b}$$

$$\boldsymbol{X}'_{p3} = \boldsymbol{X}_{p3} - \boldsymbol{X}_{p1} = [R - Rcos\vartheta(\gamma \Delta t)]\boldsymbol{i} + [Rsin\vartheta(\gamma \Delta t)]\boldsymbol{j}, \tag{2.27c}$$

$$\boldsymbol{X}'_{p4} = \boldsymbol{X}_{p4} - \boldsymbol{X}_{p1} = [R - Rcos\vartheta(\Delta t)]\boldsymbol{i} + [Rsin\vartheta(\Delta t)]\boldsymbol{j}. \tag{2.27d}$$

We still use $\boldsymbol{X}_{pi,m}$ defined in Equation (2.8) to denote measured particle locations, the particle trajectory estimation is given by

$$\hat{\boldsymbol{X}}_p(t') = (1 + \boldsymbol{a}_1 \cdot \bar{\boldsymbol{t}}')\boldsymbol{X}_{p1,m} + (\boldsymbol{a}_2 \cdot \bar{\boldsymbol{t}}')\boldsymbol{X}_{p2,m} + (\boldsymbol{a}_3 \cdot \bar{\boldsymbol{t}}')\boldsymbol{X}_{p3,m} + (\boldsymbol{a}_4 \cdot \bar{\boldsymbol{t}}')\boldsymbol{X}_{p4,m}, \tag{2.28}$$

in which vector $\boldsymbol{a}_i, i = 1, 2, 3, 4$ are defined as

$$\boldsymbol{a}_1 = \frac{1}{\beta\gamma} \left(-\beta\gamma - \beta - \gamma, 1 + \beta + \gamma, -1 \right), \tag{2.29a}$$

$$\boldsymbol{a}_2 = \frac{1}{\beta(1 - \beta)(\gamma - \beta)} \left(\gamma, -\gamma - 1, 1 \right), \tag{2.29b}$$

$$\boldsymbol{a}_3 = \frac{1}{\gamma(1 - \gamma)(\gamma - \beta)} \left(-\beta, \beta + 1, -1 \right), \tag{2.29c}$$

$$\boldsymbol{a}_4 = \frac{1}{(1 - \beta)(1 - \gamma)} \left(\beta\gamma, -\beta - \gamma, 1 \right), \tag{2.29d}$$

and time vector $\bar{\boldsymbol{t}}'$ is defined as

$$\bar{\boldsymbol{t}}' = \left(\frac{t'}{\Delta t}, \frac{t'^2}{\Delta t^2}, \frac{t'^3}{\Delta t^3} \right). \tag{2.30}$$

Subsequently, the velocity estimation is

$$\dot{\hat{\boldsymbol{X}}}_p(t') = (\boldsymbol{a}_1 \cdot \dot{\boldsymbol{t}}')\boldsymbol{X}_{p1,m} + (\boldsymbol{a}_2 \cdot \dot{\boldsymbol{t}}')\boldsymbol{X}_{p2,m} + (\boldsymbol{a}_3 \cdot \dot{\boldsymbol{t}}')\boldsymbol{X}_{p3,m} + (\boldsymbol{a}_4 \cdot \dot{\boldsymbol{t}}')\boldsymbol{X}_{p4,m}, \quad (2.31)$$

with

$$\dot{\boldsymbol{t}}' = \frac{1}{\Delta t}\left(1, \frac{2t'}{\Delta t}, \frac{3t'^2}{\Delta t^2}\right). \quad (2.32)$$

The acceleration estimation is

$$\ddot{\hat{\boldsymbol{X}}}_p(t') = (\boldsymbol{a}_1 \cdot \ddot{\boldsymbol{t}}')\boldsymbol{X}_{p1,m} + (\boldsymbol{a}_2 \cdot \ddot{\boldsymbol{t}}')\boldsymbol{X}_{p2,m} + (\boldsymbol{a}_3 \cdot \ddot{\boldsymbol{t}}')\boldsymbol{X}_{p3,m} + (\boldsymbol{a}_4 \cdot \ddot{\boldsymbol{t}}')\boldsymbol{X}_{p4,m}, \quad (2.33)$$

with

$$\ddot{\boldsymbol{t}}' = \frac{1}{\Delta t^2}\left(0, 2, \frac{6t'}{\Delta t}\right). \quad (2.34)$$

The RMS errors in position, velocity, and acceleration are normalized in the same way as shown in Equation (2.15), (2.16), and (2.17). Thus we can calculate the normalized RMS errors of quadruple-pulse PTV:

$$
\begin{aligned}
\bar{\sigma}^2_{X_p} = {} & \left(\boldsymbol{a}_2 \cdot \bar{\boldsymbol{t}}'\left[1 - cos(\dot{\vartheta}_0\beta\Delta t + \frac{1}{2}\ddot{\vartheta}_0\beta^2\Delta t^2)\right] + \boldsymbol{a}_3 \cdot \bar{\boldsymbol{t}}'\left[1 - cos(\dot{\vartheta}_0\gamma\Delta t + \frac{1}{2}\ddot{\vartheta}_0\gamma^2\Delta t^2)\right]\right. \\
& \left. + \boldsymbol{a}_4 \cdot \bar{\boldsymbol{t}}'\left[1 - cos(\dot{\vartheta}_0\Delta t + \frac{1}{2}\ddot{\vartheta}_0\Delta t^2)\right] - \left[1 - cos(\dot{\vartheta}_0 t' + \frac{1}{2}\ddot{\vartheta}_0 t'^2)\right]\right)^2 \\
& + \left(\boldsymbol{a}_2 \cdot \bar{\boldsymbol{t}}'\left[sin(\dot{\vartheta}_0\beta\Delta t + \frac{1}{2}\ddot{\vartheta}_0\beta^2\Delta t^2)\right] + \boldsymbol{a}_3 \cdot \bar{\boldsymbol{t}}'\left[sin(\dot{\vartheta}_0\gamma\Delta t + \frac{1}{2}\ddot{\vartheta}_0\gamma^2\Delta t^2)\right]\right. \\
& \left. + \boldsymbol{a}_4 \cdot \bar{\boldsymbol{t}}'\left[sin(\dot{\vartheta}_0\Delta t + \frac{1}{2}\ddot{\vartheta}_0\Delta t^2)\right] - sin(\dot{\vartheta}_0 t' + \frac{1}{2}\ddot{\vartheta}_0 t'^2)\right)^2 \\
& + \left([1 + \boldsymbol{a}_1 \cdot \bar{\boldsymbol{t}}']^2 + [\boldsymbol{a}_2 \cdot \bar{\boldsymbol{t}}']^2 + [\boldsymbol{a}_3 \cdot \bar{\boldsymbol{t}}']^2 + [\boldsymbol{a}_4 \cdot \bar{\boldsymbol{t}}']^2\right)\frac{\langle|\delta\boldsymbol{X}_p|^2\rangle}{R^2}. \quad (2.35)
\end{aligned}
$$

$$\bar{\sigma}_v^2 = \frac{1}{(1 + \ddot{\vartheta}_0 \Delta t / \dot{\vartheta}_0)^2} \left(\boldsymbol{a}_2 \cdot \frac{\dot{\boldsymbol{t}}'}{\dot{\vartheta}_0} \left[1 - cos(\dot{\vartheta}_0 \beta \Delta t + \frac{1}{2} \ddot{\vartheta}_0 \beta^2 \Delta t^2) \right] \right.$$

$$+ \boldsymbol{a}_3 \cdot \frac{\dot{\boldsymbol{t}}'}{\dot{\vartheta}_0} \left[1 - cos(\dot{\vartheta}_0 \gamma \Delta t + \frac{1}{2} \ddot{\vartheta}_0 \gamma^2 \Delta t^2) \right]$$

$$\left. + \boldsymbol{a}_4 \cdot \frac{\dot{\boldsymbol{t}}'}{\dot{\vartheta}_0} \left[1 - cos(\dot{\vartheta}_0 \Delta t + \frac{1}{2} \ddot{\vartheta}_0 \Delta t^2) \right] - \left[sin(\dot{\vartheta}_0 t' + \frac{1}{2} \ddot{\vartheta}_0 t'^2)(1 + \frac{\ddot{\vartheta}_0 t'}{\dot{\vartheta}_0}) \right] \right)^2$$

$$+ \frac{1}{(1 + \ddot{\vartheta}_0 \Delta t / \dot{\vartheta}_0)^2} \left(\boldsymbol{a}_2 \cdot \frac{\dot{\boldsymbol{t}}'}{\dot{\vartheta}_0} \left[sin(\dot{\vartheta}_0 \beta \Delta t + \frac{1}{2} \ddot{\vartheta}_0 \beta^2 \Delta t^2) \right] \right.$$

$$+ \boldsymbol{a}_3 \cdot \frac{\dot{\boldsymbol{t}}'}{\dot{\vartheta}_0} \left[sin(\dot{\vartheta}_0 \gamma \Delta t + \frac{1}{2} \ddot{\vartheta}_0 \gamma^2 \Delta t^2) \right]$$

$$\left. + \boldsymbol{a}_4 \cdot \frac{\dot{\boldsymbol{t}}'}{\dot{\vartheta}_0} \left[sin(\dot{\vartheta}_0 \Delta t + \frac{1}{2} \ddot{\vartheta}_0 \Delta t^2) \right] - \left[cos(\dot{\vartheta}_0 t' + \frac{1}{2} \ddot{\vartheta}_0 t'^2)(1 + \frac{\ddot{\vartheta}_0 t'}{\dot{\vartheta}_0}) \right] \right)^2$$

$$+ \frac{1}{(1 + \ddot{\vartheta}_0 \Delta t / \dot{\vartheta}_0)^2} \left(\left[\boldsymbol{a}_1 \cdot \frac{\dot{\boldsymbol{t}}'}{\dot{\vartheta}_0} \right]^2 + \left[\boldsymbol{a}_2 \cdot \frac{\dot{\boldsymbol{t}}'}{\dot{\vartheta}_0} \right]^2 \right.$$

$$\left. + \left[\boldsymbol{a}_3 \cdot \frac{\dot{\boldsymbol{t}}'}{\dot{\vartheta}_0} \right]^2 + \left[\boldsymbol{a}_4 \cdot \frac{\dot{\boldsymbol{t}}'}{\dot{\vartheta}_0} \right]^2 \right) \frac{\langle |\delta \boldsymbol{X}_p|^2 \rangle}{R^2}. \tag{2.36}$$

$$
\begin{aligned}
\bar{\sigma}_a^2 = & \frac{1}{1+\dot{\vartheta}_0^4/\ddot{\vartheta}_0^2}\left(\boldsymbol{a}_2\cdot\frac{\dddot{\boldsymbol{t}}'}{\dddot{\vartheta}_0}\left[1-\cos(\dot{\vartheta}_0\beta\Delta t+\frac{1}{2}\ddot{\vartheta}_0\beta^2\Delta t^2)\right]\right.\\
& +\boldsymbol{a}_3\cdot\frac{\dddot{\boldsymbol{t}}'}{\dddot{\vartheta}_0}\left[1-\cos(\dot{\vartheta}_0\gamma\Delta t+\frac{1}{2}\ddot{\vartheta}_0\gamma^2\Delta t^2)\right]\\
& +\boldsymbol{a}_4\cdot\frac{\dddot{\boldsymbol{t}}'}{\dddot{\vartheta}_0}\left[1-\cos(\dot{\vartheta}_0\Delta t+\frac{1}{2}\ddot{\vartheta}_0\Delta t^2)\right]\\
& \left.-\left[\cos(\dot{\vartheta}_0t'+\frac{1}{2}\ddot{\vartheta}_0t'^2)(\frac{\dot{\vartheta}_0^2}{\dddot{\vartheta}_0}+\ddot{\vartheta}_0t'^2+2\dot{\vartheta}_0t')+\sin(\dot{\vartheta}_0t'+\frac{1}{2}\ddot{\vartheta}_0t'^2)\right]\right)^2\\
& +\frac{1}{1+\dot{\vartheta}_0^4/\ddot{\vartheta}_0^2}\left(\boldsymbol{a}_2\cdot\frac{\dddot{\boldsymbol{t}}'}{\dddot{\vartheta}_0}\left[\sin(\dot{\vartheta}_0\beta\Delta t+\frac{1}{2}\ddot{\vartheta}_0\beta^2\Delta t^2)\right]\right.\\
& +\boldsymbol{a}_3\cdot\frac{\dddot{\boldsymbol{t}}'}{\dddot{\vartheta}_0}\left[\sin(\dot{\vartheta}_0\gamma\Delta t+\frac{1}{2}\ddot{\vartheta}_0\gamma^2\Delta t^2)\right]\\
& +\boldsymbol{a}_4\cdot\frac{\dddot{\boldsymbol{t}}'}{\dddot{\vartheta}_0}\left[\sin(\dot{\vartheta}_0\Delta t+\frac{1}{2}\ddot{\vartheta}_0\Delta t^2)\right]\\
& \left.-\left[-\sin(\dot{\vartheta}_0t'+\frac{1}{2}\ddot{\vartheta}_0t'^2)(\frac{\dot{\vartheta}_0^2}{\dddot{\vartheta}_0}+\ddot{\vartheta}_0t'^2+2\dot{\vartheta}_0t')+\cos(\dot{\vartheta}_0t'+\frac{1}{2}\ddot{\vartheta}_0t'^2)\right]\right)^2\\
& +\frac{1}{1+\dot{\vartheta}_0^4/\ddot{\vartheta}_0^2}\left(\left[\boldsymbol{a}_1\cdot\frac{\dddot{\boldsymbol{t}}'}{\dddot{\vartheta}_0}\right]^2+\left[\boldsymbol{a}_2\cdot\frac{\dddot{\boldsymbol{t}}'}{\dddot{\vartheta}_0}\right]^2\right.\\
& \left.+\left[\boldsymbol{a}_3\cdot\frac{\dddot{\boldsymbol{t}}'}{\dddot{\vartheta}_0}\right]^2+\left[\boldsymbol{a}_4\cdot\frac{\dddot{\boldsymbol{t}}'}{\dddot{\vartheta}_0}\right]^2\right)\frac{\langle|\delta\boldsymbol{X}_p|^2\rangle}{R^2}.
\end{aligned}
\tag{2.37}
$$

Using the same cost functions defined in Equation (2.22) and (2.23), we are aiming to achieve the optimization of quadruple-pulse PTV measurement. The simulation is conducted in the same fashion as of triple-pulse PTV simulation, except that the particle displacement is considered between 20 and 40 pixels since we add another pulse to resolve the particle motion. Table 2.3 lists a wide range of realistic R values and the corresponding noise levels and normalized displacement ranges. Table 2.4 illustrates the parameter space used in quadruple-pulse PTV simulation.

$\sqrt{\langle\|\delta\boldsymbol{X}_p\|^2\rangle}$ (pix)	R (pix)	$\sqrt{\langle\|\delta\boldsymbol{X}_p\|^2\rangle}\big/R$	$\dot{\vartheta}_0\Delta t$
0.3	30	1.0%	0.67-1.33
	40	0.75%	0.5-1.0
	60	0.5%	0.33-0.67
	200	0.15%	0.1-0.2
	400	0.075%	0.05-0.1
	1000	0.03%	0.02-0.04

Table 2.3: List of noise levels and corresponding normalized displacements with wide range of radius of curvature. Assume particle displacement is 20-40 pixels.

d_τ	$22.5\mu m$
β	1/3
γ	2/3
$t'/\Delta t$	$[0,1]$
$\ddot{\vartheta}_0\Delta t/2\dot{\vartheta}_0$	$-0.3, -0.1, 0, 0.2, 0.4$
$\sqrt{\langle\|\delta\boldsymbol{X}_p\|^2\rangle}\big/R$	$0.03\%, 0.075\%, 0.15\%, 0.5\%, 0.75\%, 1.0\%$
$\dot{\vartheta}_0\Delta t$	Corresponds to the noise level, see Table 2.3

Table 2.4: Parameter space for quadruple-pulse PTV simulation with particle displacement range constraint

2.2.2 Simulation results for velocity measurement

Figure 2.8 and 2.9 show the velocity cost function for quadruple-pulse simulation. The minimum cost globally shows at $t'/\Delta t$=0.25 and 0.75.
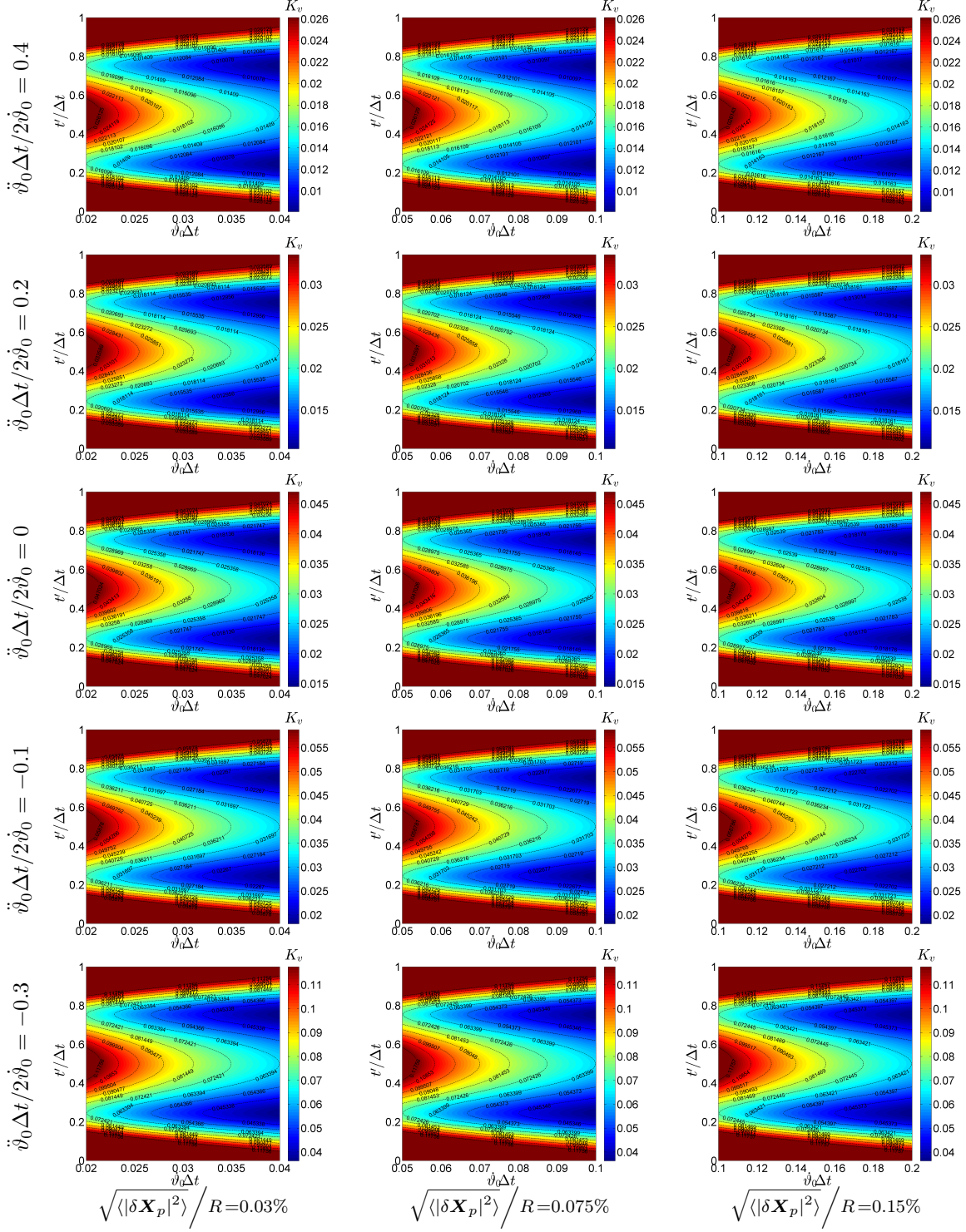
Figure 2.8: Quadruple-pulse velocity cost function with 0.03%, 0.075%, 0.15% noise level, with particle displacement range constraint
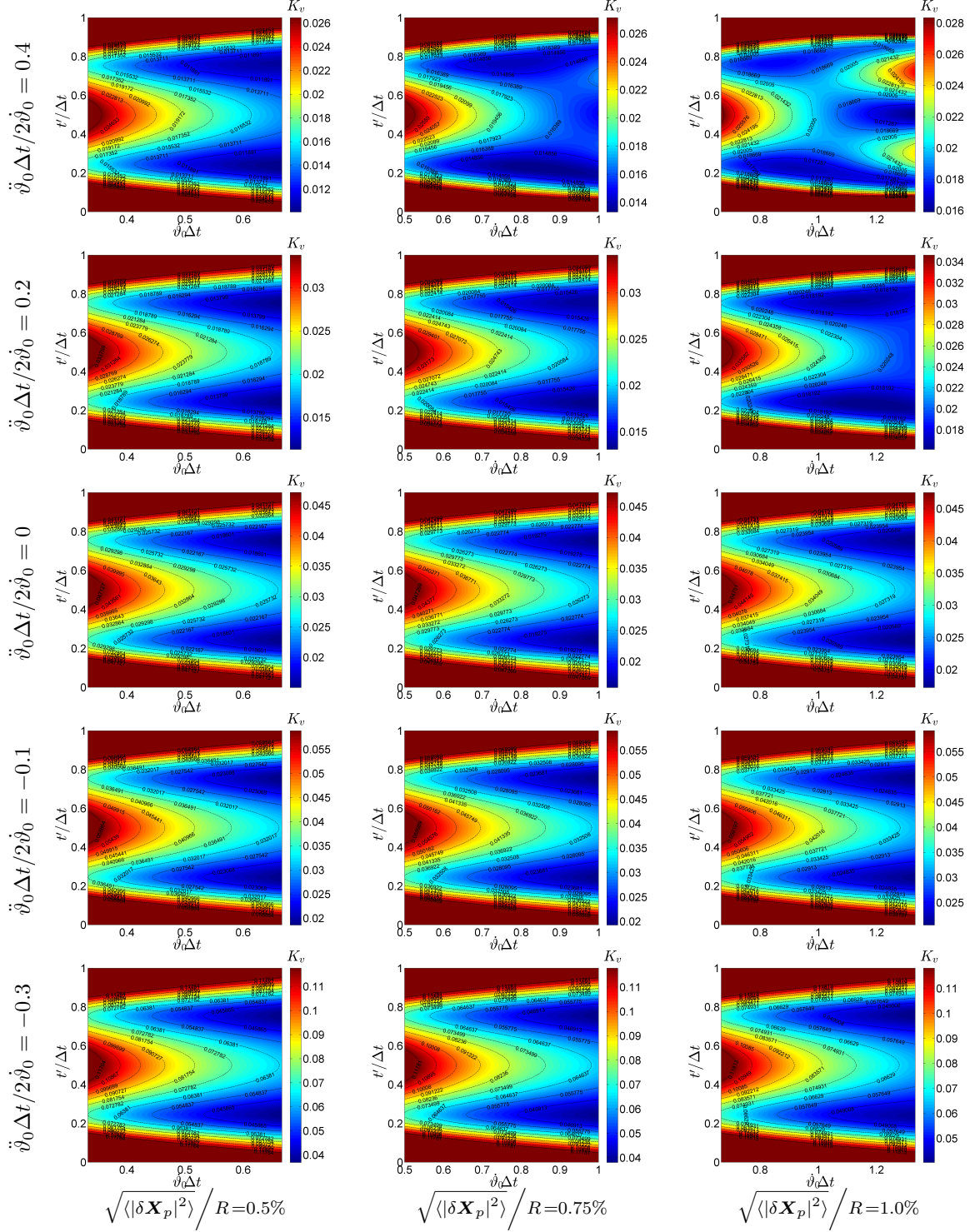
Figure 2.9: Quadruple-pulse velocity cost function with 0.5%, 0.75%, 1.0% noise level, with particle displacement range constraint
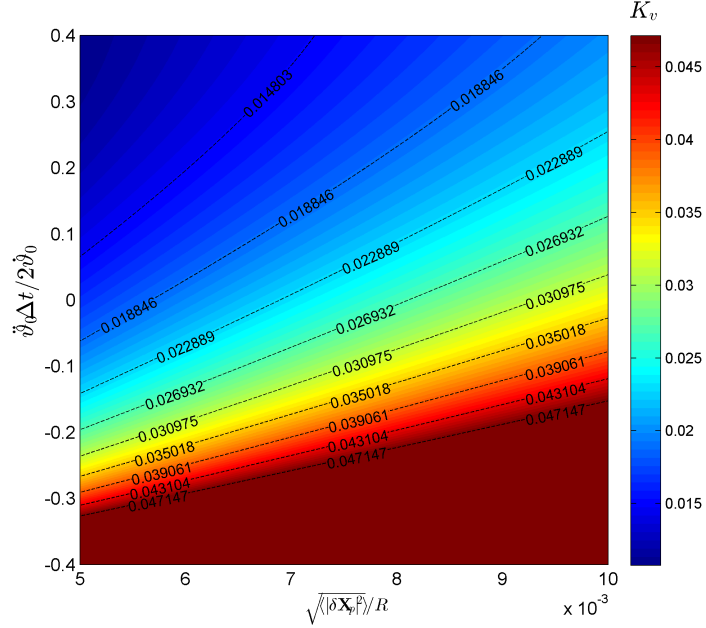
Figure 2.10: Quadruple-pulse velocity cost function plotted against acceleration factor and noise level, with $t'/\Delta t = 0.75$ and $\dot{\vartheta}_0 \Delta t = 0.6$

Figure 2.10 shows the velocity cost function with respect to the noise level and the acceleration factor. Similarly with triple-pulse simulation, the error percentage increases with the increasing noise level. Interestingly, the error percentage is larger when there is less acceleration or more deceleration. In other words, when the full scale velocity $R(\dot{\vartheta}_0 + \ddot{\vartheta}_0 \Delta t)$ is smaller, we get higher velocity error percentage. In comparison with Figure 2.4 of triple-pulse simulation, in which the error percentage increases with the acceleration factor magnitude increases, we could draw the following interpretation. That is, in triple-pulse case, the difference between a linear velocity estimation and a curved velocity profile dominates the velocity error percentage, whereas in quadruple-pule case, a quadratic velocity estimation works better and the velocity error percentage is dominated by the magnitude of the full scale velocity. In addition, we also see that the error percentage change due to noise level becomes less rapid for higher acceleration factor.

2.2.3   Simulation results for acceleration measurement

The acceleration cost function is plotted in Figure 2.11 and 2.12. The optimization is globally observed at $t'/\Delta t$=0.5.

Figure 2.11: Quadruple-pulse acceleration cost function with 0.03%, 0.075%, 0.15% noise level, with particle displacement range constraint
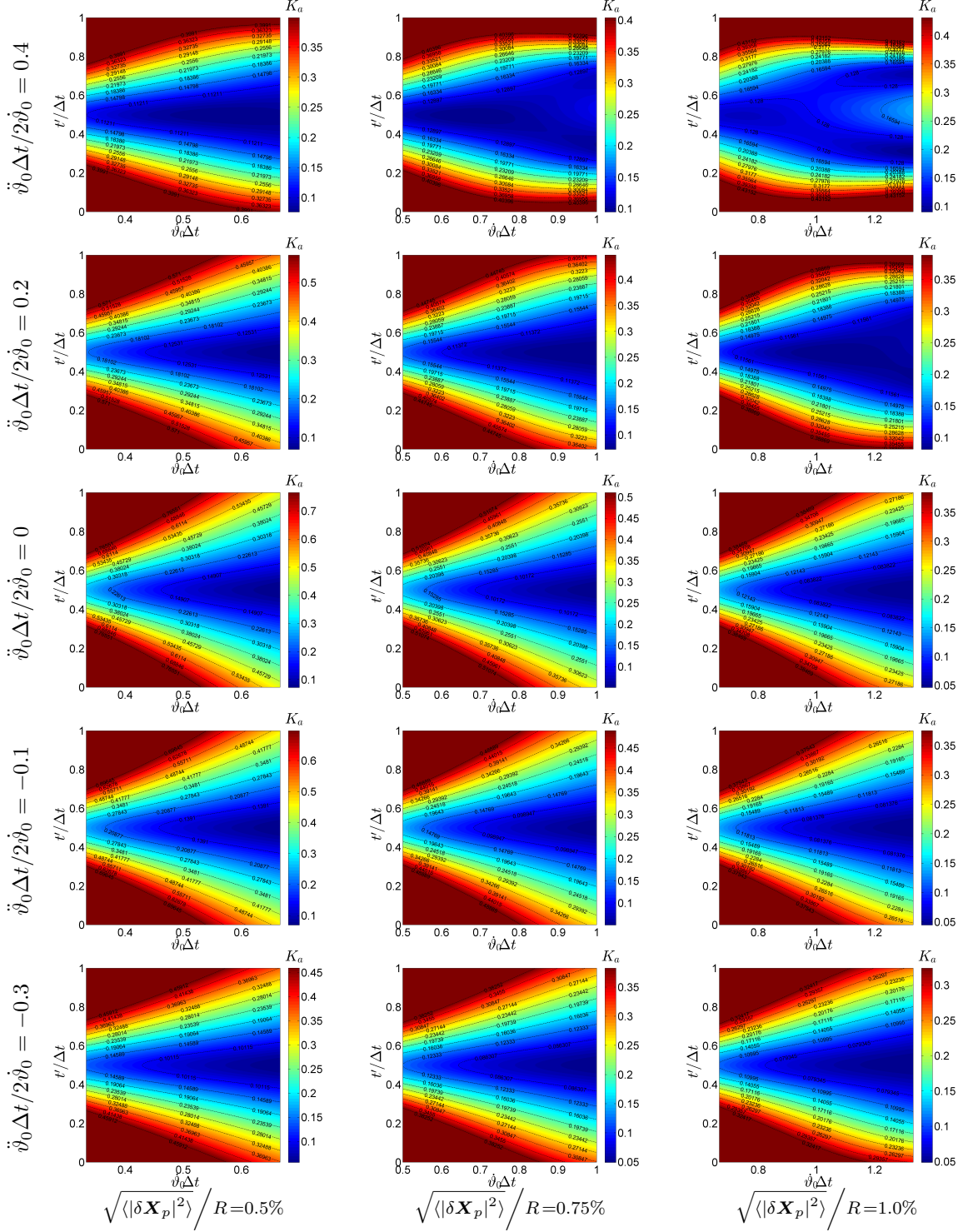
Figure 2.12: Quadruple-pulse acceleration cost function with 0.5%, 0.75%, 1.0% noise level, with particle displacement range constraint

35
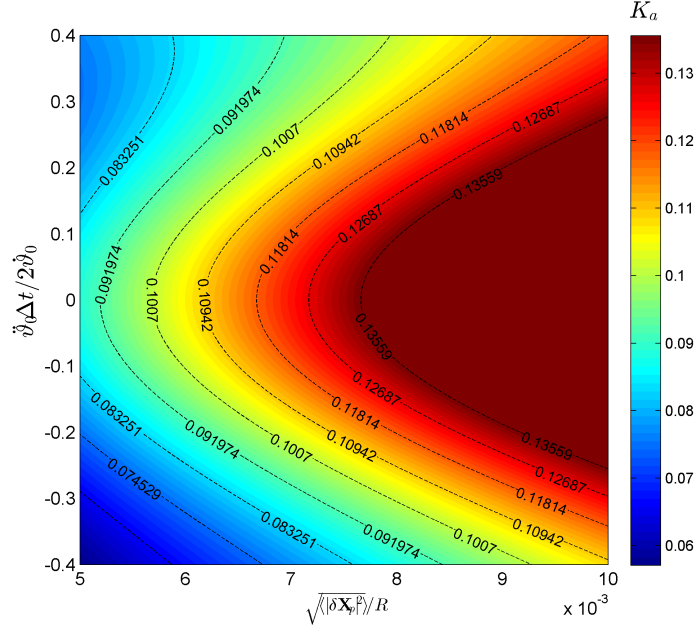
Figure 2.13: Quadruple-pulse acceleration cost function plotted against acceleration factor and noise level, with $t'/\Delta t=0.5$ and $\dot{\vartheta}_0\Delta t=0.6$

	3-pulse	4-pulse
velocity	$t'/\Delta t=0.21$ or 0.78 for $\sqrt{\langle\|\delta\boldsymbol{X}_p\|^2\rangle}\Big/R \geqslant 0.75$ and $\left\|\ddot{\vartheta}_0\Delta t/2\dot{\vartheta}_0\right\| \geqslant 0.3$ (approx.); otherwise, $t'/\Delta t=0.5$	$t'/\Delta t=0.25$ or 0.75
acceleration	$t'/\Delta t=0.5$	$t'/\Delta t=0.5$

Table 2.5: Summary of the optimization for triple-pulse and quadruple-pulse velocity and acceleration measurement, with particle displacement range constraint

The acceleration cost function of quadruple-pulse simulation is plotted against the noise level and the acceleration factor in Figure 2.13. Similar to Figure 2.7, we see the error percentage increases with the noise level increasing and the acceleration factor magnitude increasing; the error percentage changes less rapidly with the noise level for higher acceleration or deceleration, which guide us to achieve better acceleration measurement by enhancing the full-scale acceleration magnitude.

Table 2.5 summarizes the optimization for triple- and quadruple-pulse velocity

36

and acceleration measurement, assuming the particle displacement range is limited by current PIV systems.

Chapter 3

TRIPLE- AND QUADRUPLE-PULSE PTV SIMULATION WITHOUT

PARTICLE DISPLACEMENT RANGE CONSTRAINT

In previous chapter, the multi-pulse PTV is investigated with the assumption that the

particle displacement is within the optimal range that is usually used for current PIV

systems. To date, the obstacles that inhibit the significant extension of the maximum

measurable particle displacement include the out-of-plane motion that causes the

loss of particle pairs, as well as the capability of the interrogation algorithms to

capture particle pairs apart by a long distance. While all these constraints are realistic

currently, we would like to move one step forward. That is to evaluate the performance

of multi-pulse PTV by insulating it from the constraint of the particle displacement

range. We assume herein that all particle displacements can be measured properly

regardless of the distance they travel. All simulations in this chapter are conducted

in the same fashion as in Chapter 2, except that the normalized displacement is

considered over a much wider range. In the end, the performances of dual-pulse,

triple-pulse and quadruple-pulse PTV are comprehensively compared based on error

analysis, showing the improvement by multi-pulse PTV technique.

3.1   Optimization of triple-pulse PTV

The simulation of triple-pulse PTV without the constraint on the range of particle

displacement is presented in this section. Table 3.1 shows the parameter space that

the simulation is conducted on. The normalized displacement $\dot{\vartheta}_0 \Delta t$ is investigated

over a extended range of [0.001,1].

d_τ	22.5 μm
α	0.5
$t'/\Delta t$	[0, 1]
$\dot{\vartheta}_0 \Delta t$	[0.001,1]
$\ddot{\vartheta}_0 \Delta t / 2\dot{\vartheta}_0$	-0.3, -0.1, 0, 0.2, 0.4
$\sqrt{\langle |\delta \boldsymbol{X}_p|^2 \rangle} \big/ R$	0.03%, 0.075%, 0.15%, 0.5%, 0.75%, 1.0%

Table 3.1: Parameter space for triple-pulse PTV simulation without particle displacement range constraint

3.1.1 Simulation results of velocity measurement

Figure 3.1 and 3.2 show the velocity cost function of triple-pulse PTV over the normalized displacement from 0.01 to 1.0. Differently from the previous conclusion, we see that $t'/\Delta t$=0.21 and 0.78 appear as the optimization of the velocity measurement for wide range of $\dot{\vartheta}_0 \Delta t$. For several cases with high noise level and mild acceleration factor, the $t'/\Delta t$=0.21 and 0.78 yield the minimum only for high values of $\dot{\vartheta}_0 \Delta t$. For example, the one with zero acceleration factor and 1.0% noise level, the cost function approaches the minimum at $t'/\Delta t$=0.21 and 0.78 for $\dot{\vartheta}_0 \Delta t \geqslant 0.9$. However, since such exceptions are associated with small radius of curvature, the corresponding displacement $R\dot{\vartheta}_0 \Delta t$ is about of the range within which normal PIV measurements would be done. Thus $t'/\Delta t$=0.21 and 0.78 can be generally used to optimize the velocity measurement by triple-pulse PTV for wide range of normalized displacement.
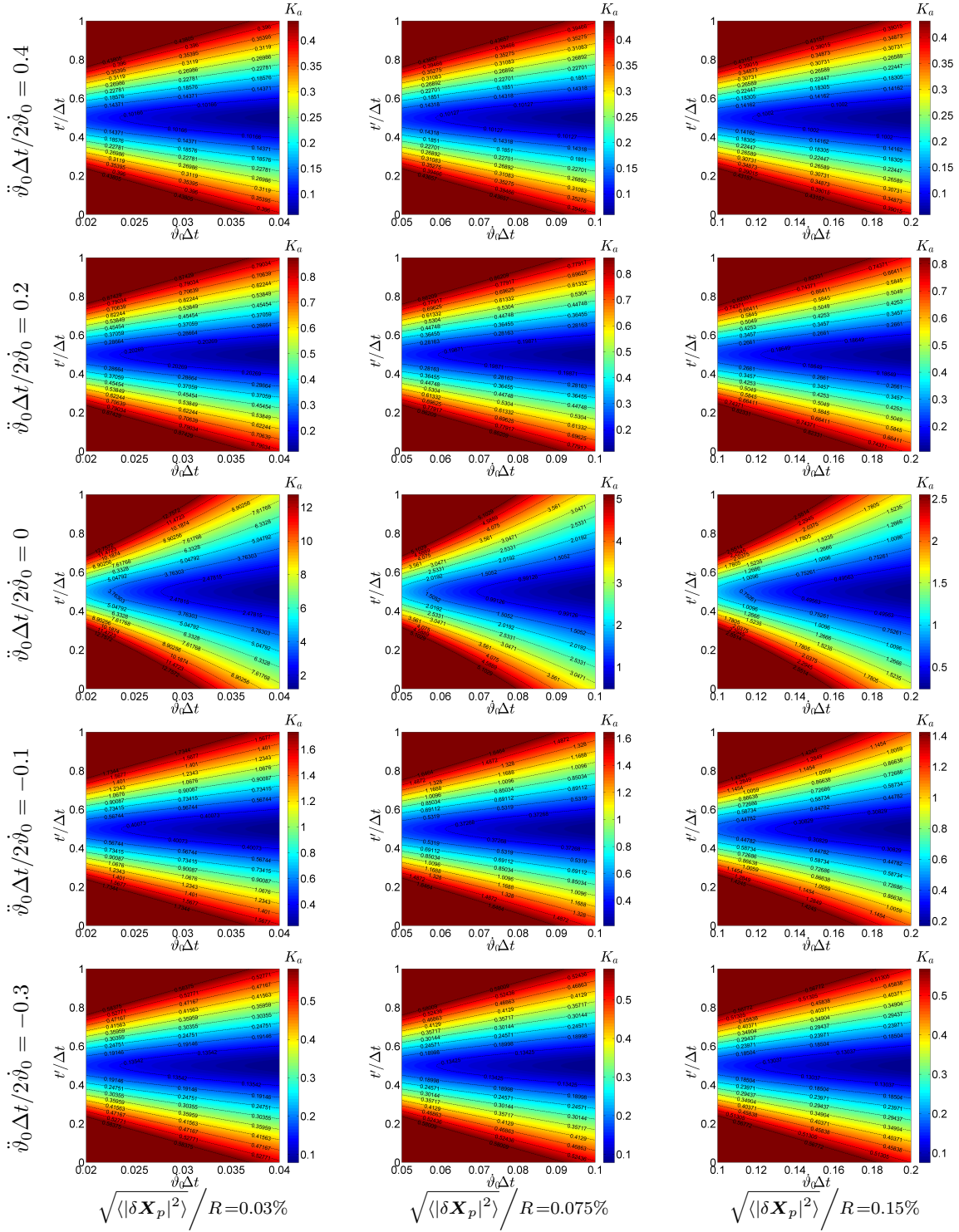
Figure 3.1: Triple-pulse velocity cost function with 0.03%, 0.075%, 0.15% noise level, without particle displacement range constraint

Figure 3.2: Triple-pulse velocity cost function with 0.5%, 0.75%, 1.0% noise level, without particle displacement range constraint

41

3.1.2 Simulation results for acceleration measurement

The acceleration cost function over $\dot{\vartheta}_0 \Delta t \in [0.001,1]$ is plotted in Figure 3.3 and 3.4. The optimization of the cost function is shown globally at $t'/\Delta t = 0.5$. This conclusion is consistent with the previous one for constrained particle displacement range.

Figure 3.3: Triple-pulse acceleration cost function with 0.03%, 0.075%, 0.15% noise level, without particle displacement range constraint

43
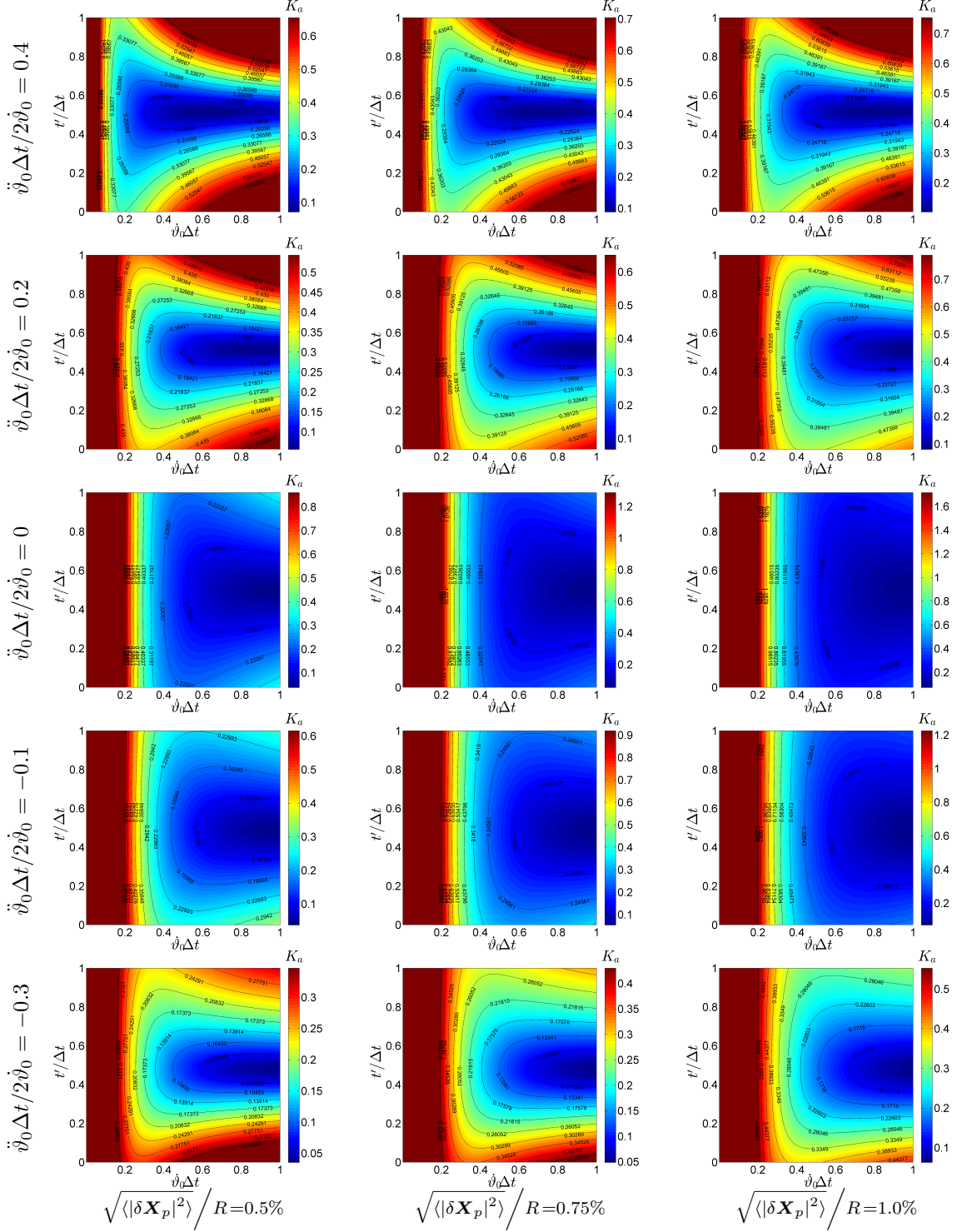
Figure 3.4: Triple-pulse acceleration cost function with 0.5%, 0.75%, 1.0% noise level, without particle displacement range constraint

3.2 Optimization of quadruple-pulse PTV

The performance of quadruple-pulse PTV is assessed over a wide range of normalized displacement in this section. Here the range of $\dot{\vartheta}_0 \Delta t$ is further released up to 1.35 since we add another pulse to resolve the particle motion. Table 3.2 shows the parameter space used in this section.

d_τ	$22.5 \mu m$
β	$1/3$
γ	$2/3$
$t'/\Delta t$	$[0, 1]$
$\dot{\vartheta}_0 \Delta t$	$[0.001, 1.35]$
$\ddot{\vartheta}_0 \Delta t / 2 \dot{\vartheta}_0$	$-0.3, -0.1, 0, 0.2, 0.4$
$\sqrt{\langle |\delta \boldsymbol{X}_p|^2 \rangle} \Big/ R$	$0.03\%, 0.075\%, 0.15\%, 0.5\%, 0.75\%, 1.0\%$

Table 3.2: Parameter space for quadruple-pulse PTV simulation without particle displacement range constraint

3.2.1 Simulation results for velocity measurement

Figure 3.5 and 3.6 show the velocity cost function of quadruple-pulse PTV simulation for $\dot{\vartheta}_0 \Delta t \in [0.001, 1.35]$. It is observed that for low noise level (approximately less than 0.1%), which corresponds to small curvature of the particle trajectory, the minimum is achieved around $t'/\Delta t = 0.13$ and 0.87, as shown in the two columns with the noise level of 0.03% and 0.075%. As the noise level increases, the evaluation moves to the regime of more curved trajectory, and the optimization is achieved at $t'/\Delta t = 0.25$ and 0.75.
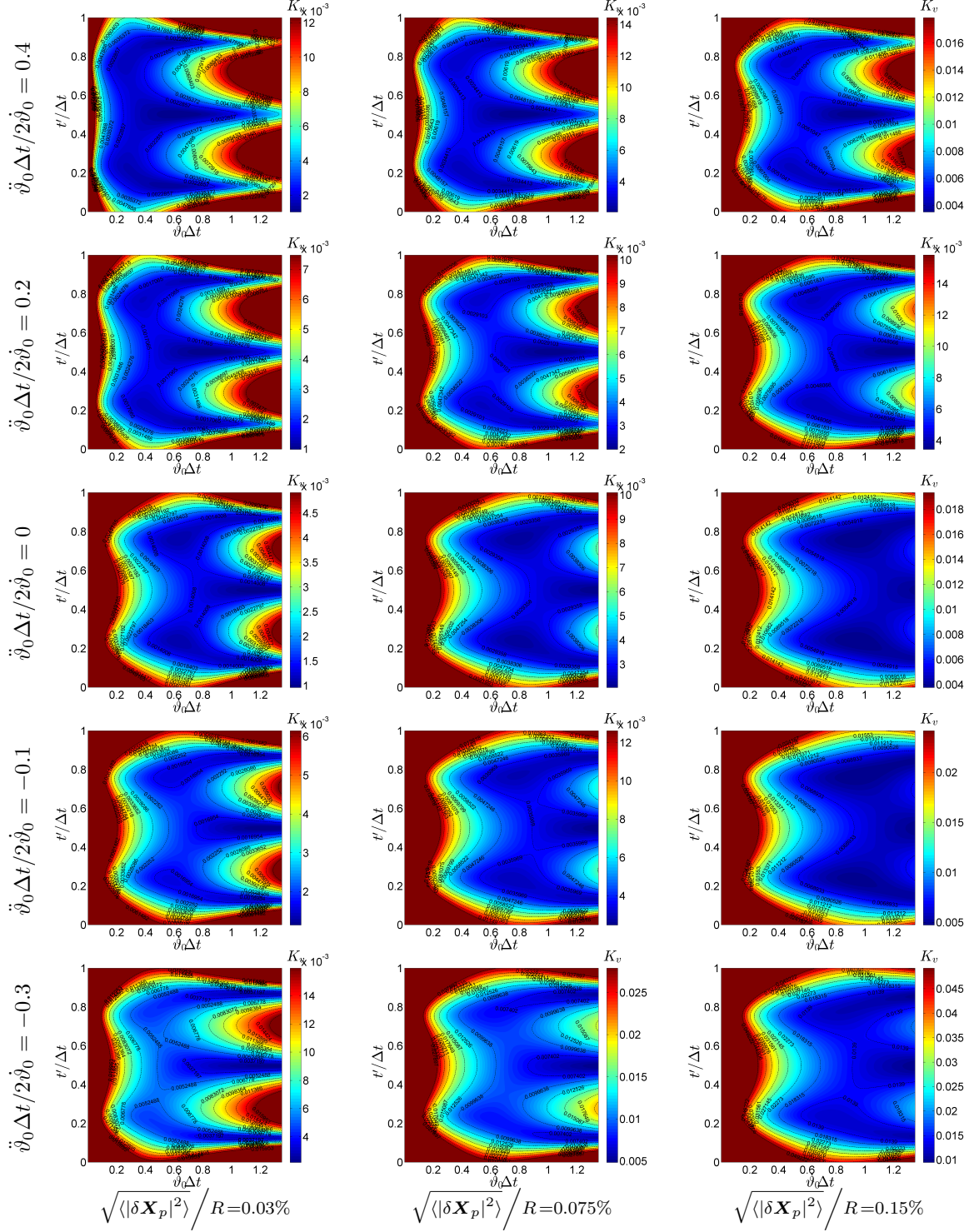
Figure 3.5: Quadruple-pulse velocity cost function with 0.03%, 0.075%, 0.15% noise level, without particle displacement range constraint

46
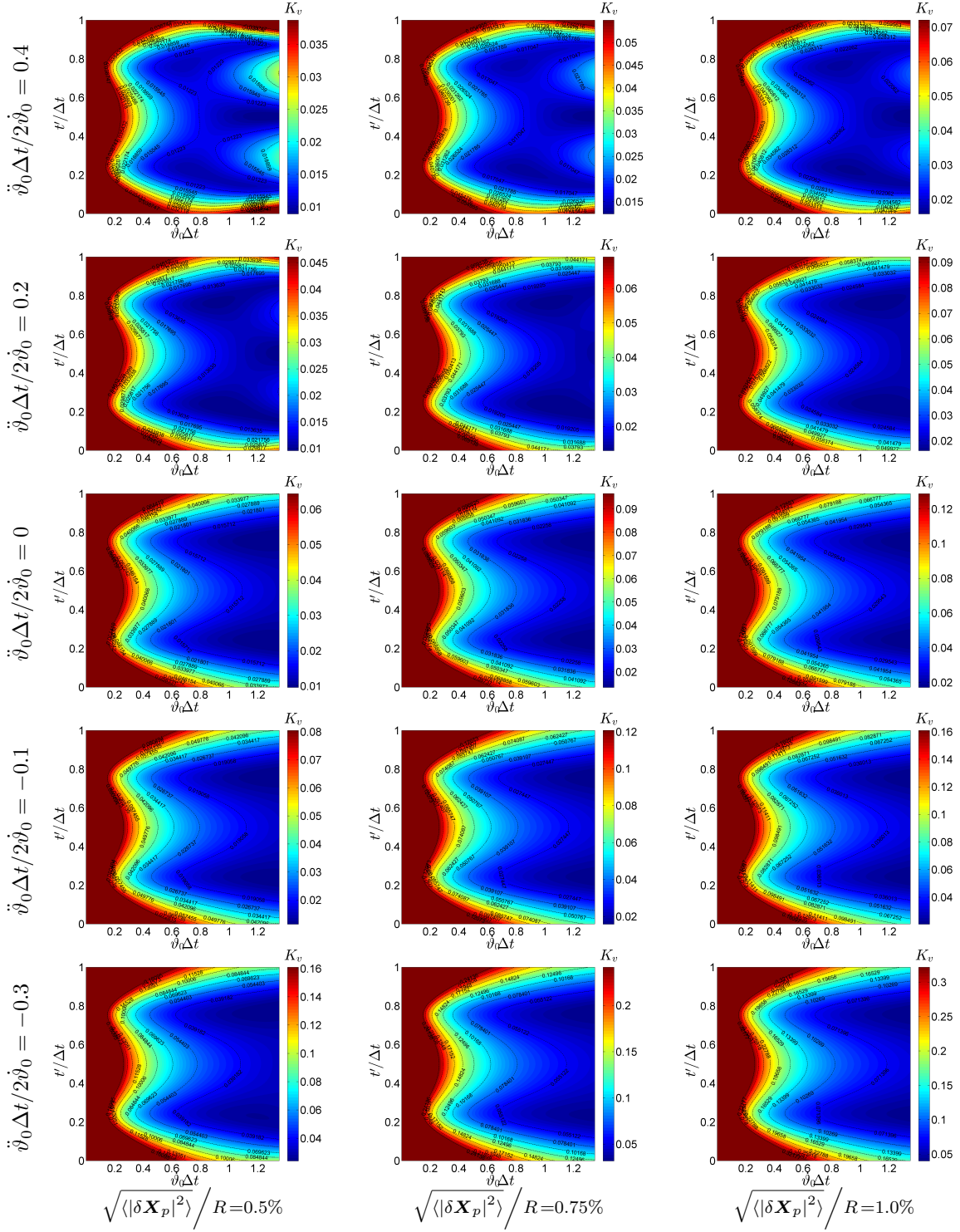
Figure 3.6: Quadruple-pulse velocity cost function with 0.5%, 0.75%, 1.0% noise level, without particle displacement range constraint

.

47

3.2.2 Simulation results for acceleration measurement

Figure 3.7 and 3.8 present the acceleration cost function of quadruple-pulse PTV without limiting the range of the particle displacement. For the cases with low noise level, the optimization appears at $t'/\Delta t$=0.28 and 0.71. Examples are the columns with the noise level of 0.03% and 0.075%. If the noise level increases, only those with strong acceleration/deceleration approach the minimum at $t'/\Delta t$=0.28 and 0.71, while for mild acceleration the optimization shows at $t'/\Delta t$=0.5. For example, we see with noise level 0.15%, those two cases with acceleration factor 0 and -0.1 has the minimum at $t'/\Delta t$=0.5. If the noise level further increases, the minimum generally shows at $t'/\Delta t$=0.5.
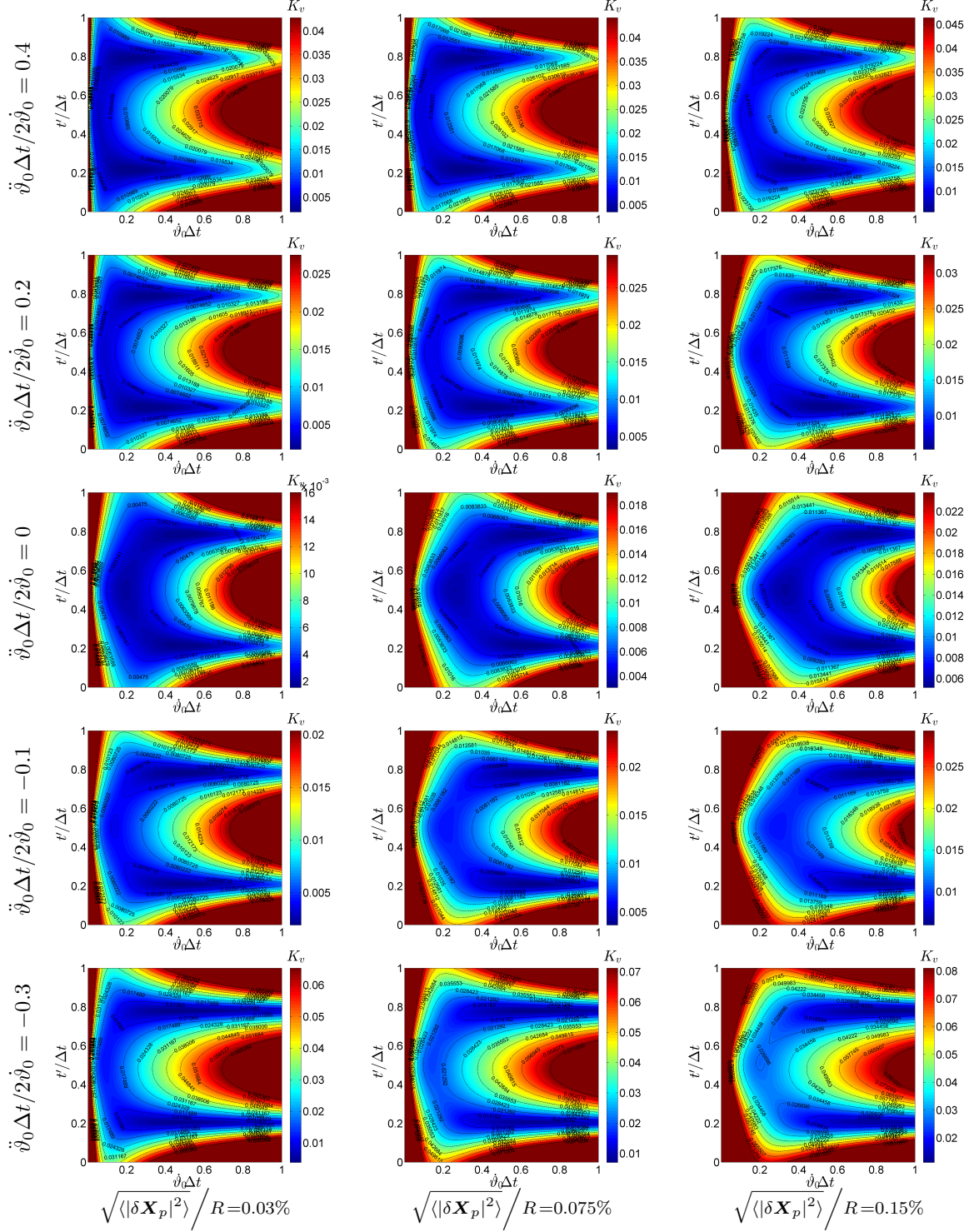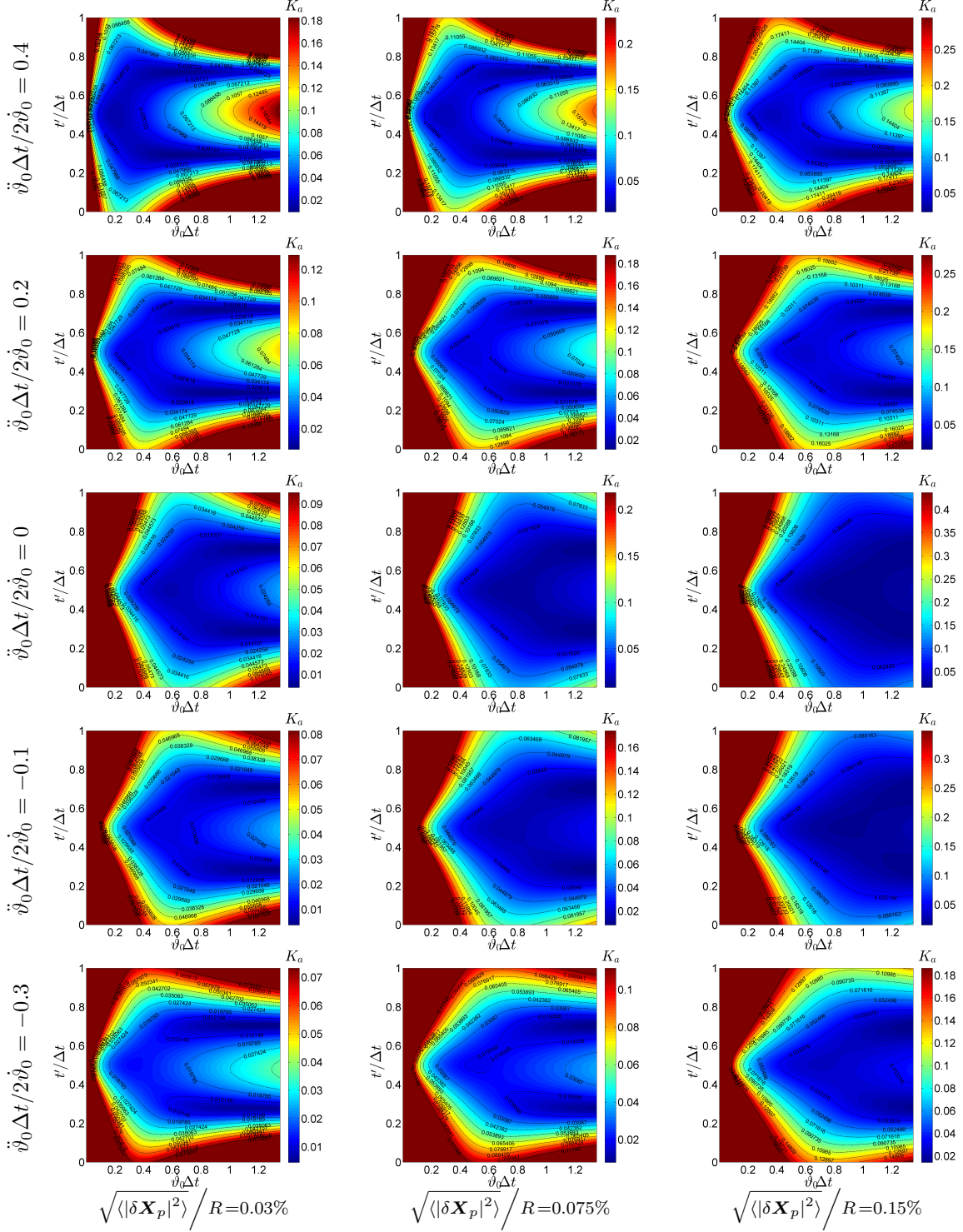
Figure 3.7: Quadruple-pulse acceleration cost function with 0.03%, 0.075%, 0.15% noise level, without particle displacement range constraint
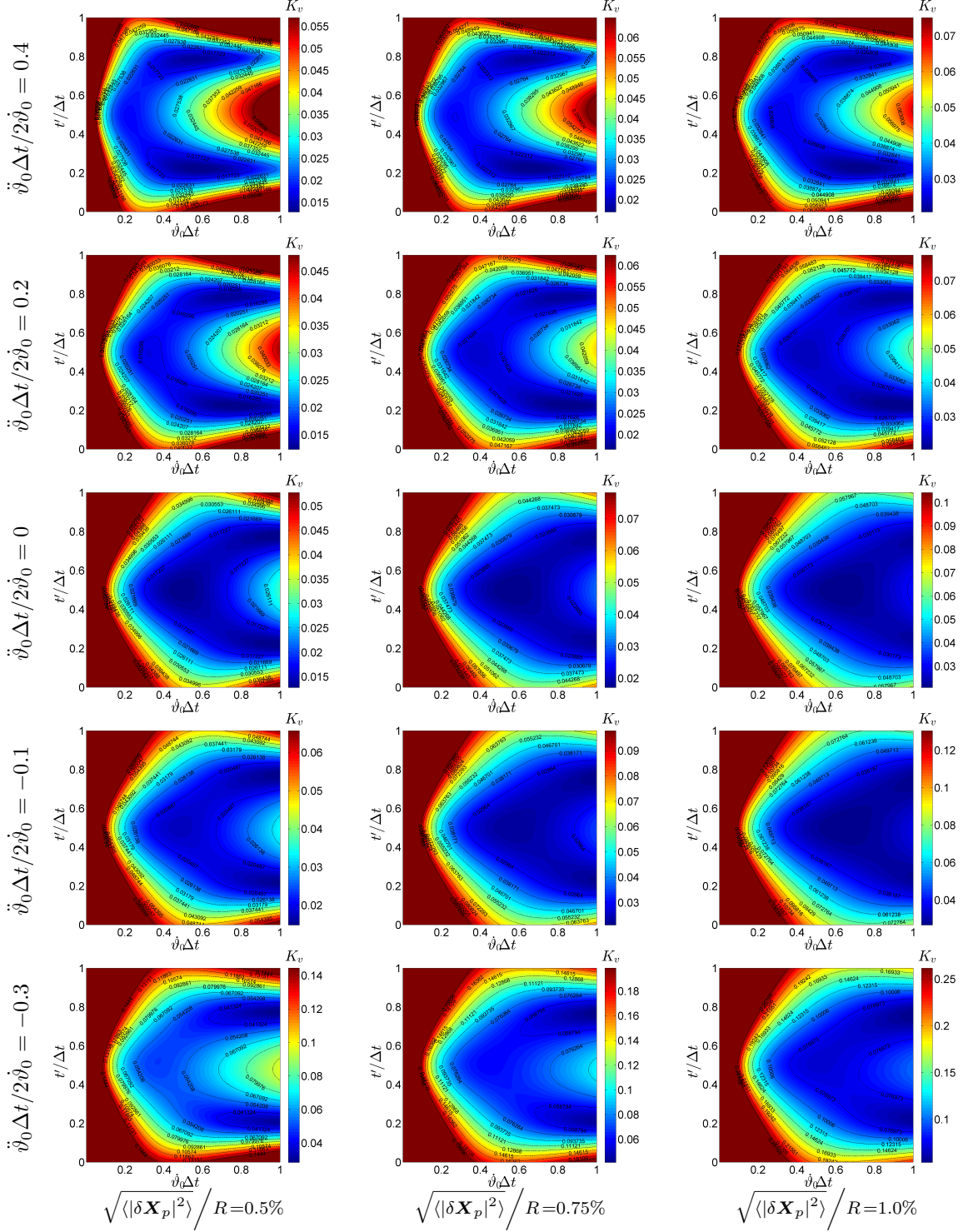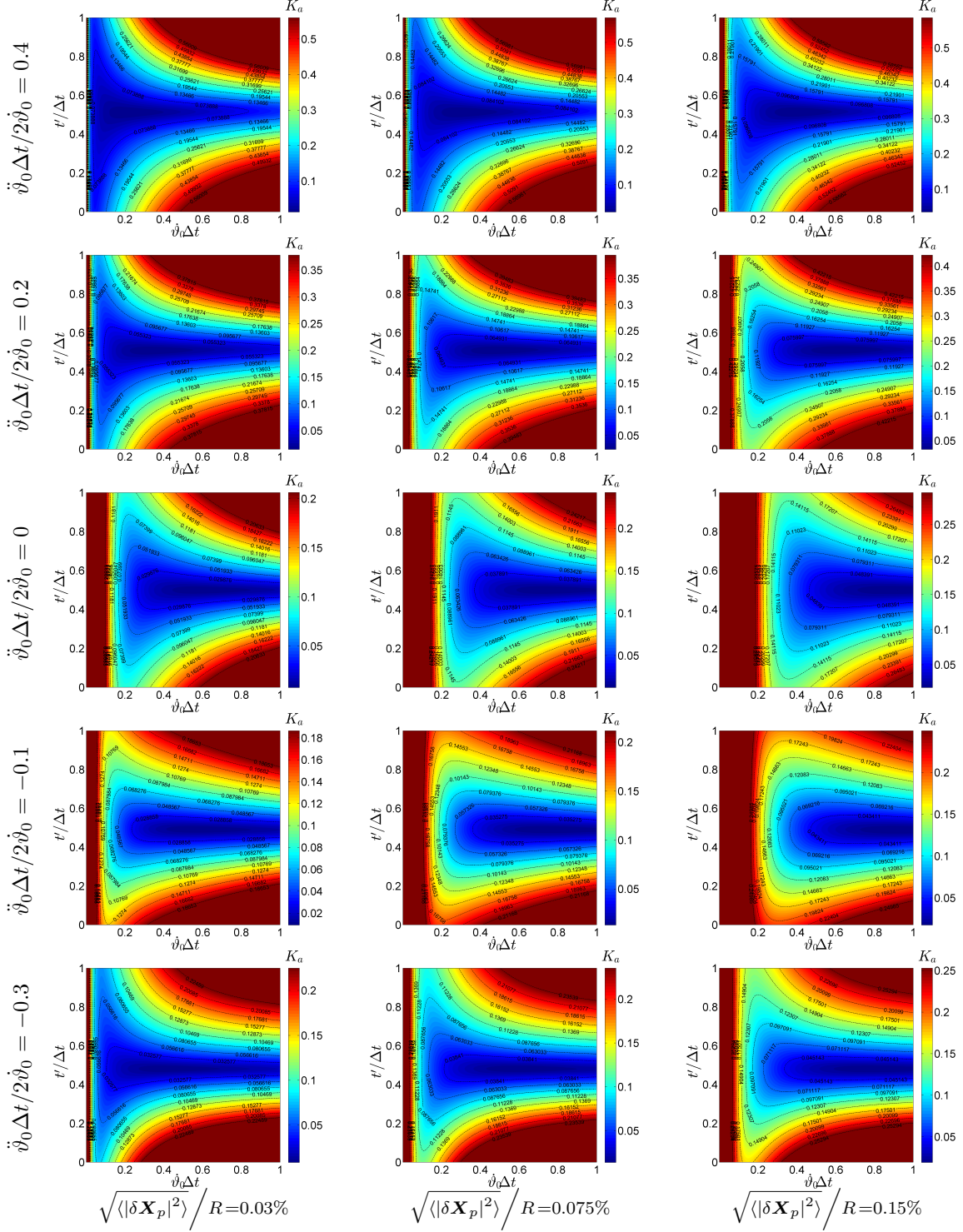
49
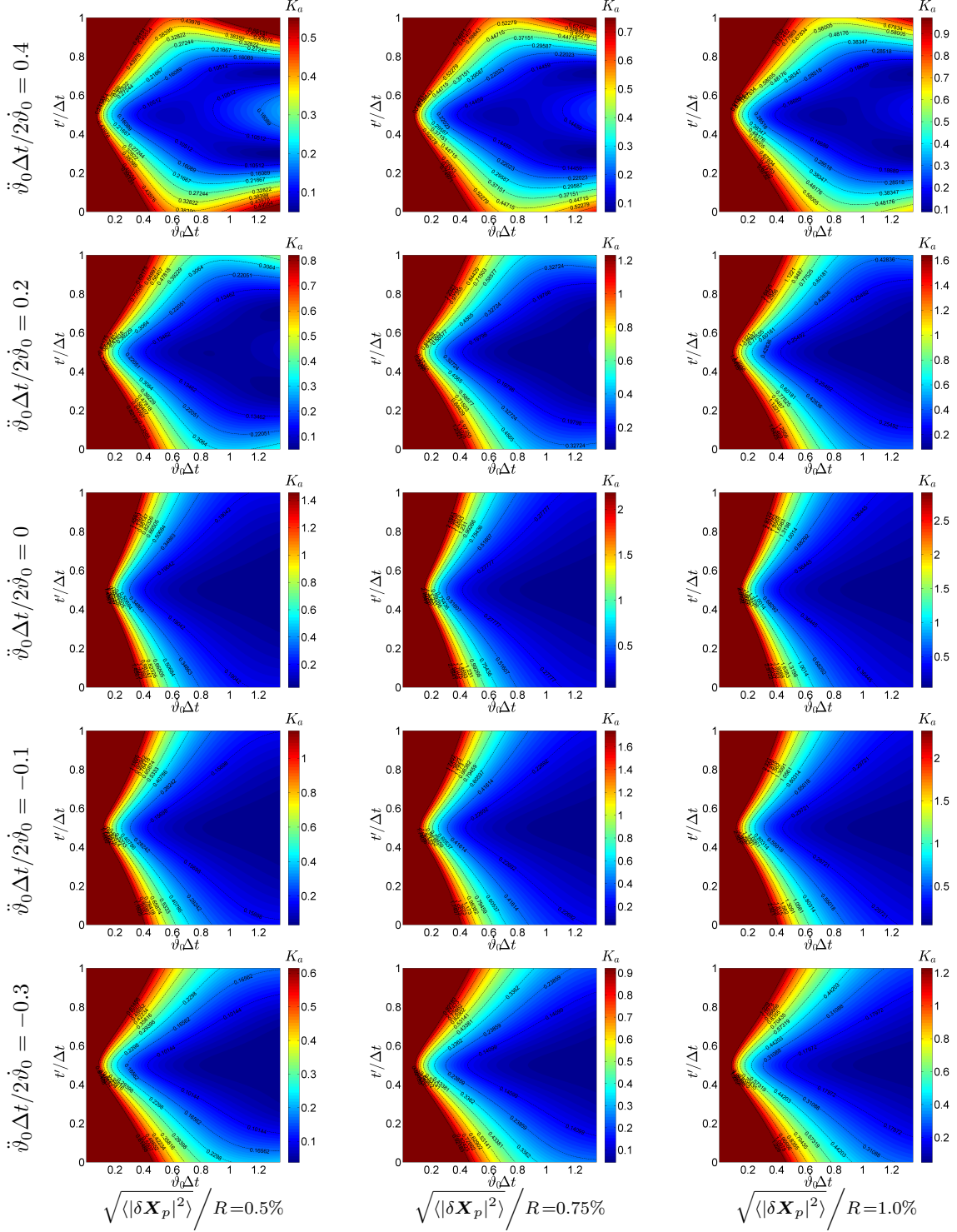
Figure 3.8: Quadruple-pulse acceleration cost function with 0.5%, 0.75%, 1.0% noise level, without particle displacement range constraint

	3-pulse	4-pulse
velocity	$t'/\Delta t$=0.21 or 0.78	$t'/\Delta t$=0.13 or 0.87 for noise level<0.1% (approx.) $t'/\Delta t$=0.25 or 0.75 for noise level$\geqslant$0.1% (approx.)
acceleration	$t'/\Delta t$=0.5	$t'/\Delta t$=0.28 or 0.71 for noise level<0.1% (approx.) $t'/\Delta t$=0.5 for noise level$\geqslant$0.1% (approx.)

Table 3.3: Summary of the optimization for triple-pulse and quadruple-pulse velocity and acceleration measurement, without particle displacement range constraint

Table 3.3 summarizes the optimization for triple- and quadruple-pulse velocity and acceleration measurement, when the constraint of the particle displacement range is released to a much wider range. The optimization behaves differently from what we have in Chapter 2.

In the following section, the errors in position, velocity and acceleration are comprehensively compared among dual-pulse, triple-pulse and quadruple-pulse PTV. To provide a complete picture of the multi-pulse PTV performance, the comparison will also consider the potential we could achieve if the maximum measurable particle displacement is extended. That depends on the development of more robust interrogation algorithms and the improvement of the manufacture technology.

3.3 Comparison of accuracy

Table 3.4 presents the velocity and position errors for velocity measurements by quadruple-, triple-, and dual-pulse PTV. The error of quadruple- and triple-pulse measurement is calculated using the optimization listed in Table 2.5 and Table 3.3. The value of $t'/\Delta t$ is adapted accordingly for different cases. The error of the dual-pulse PTV is calculated using $t'/\Delta t$=0.5. It is found that when the curvature of the trajectory is substantially small and the acceleration is negligible (Case 3), the performance of multi-pulse method can't beat conventional dual-pulse PTV. This is actually the situation that the conventional dual-pulse method is designed for. However, if some acceleration is added (Case 1), the optimized triple-pulse PTV can achieve the same accuracy as the dual-pulse PTV, but with much better position resolution. Similar features are observed from those cases with moderate curvature and acceleration (Case 4-6). That is, for the situation without large curvature and acceleration, the triple-pulse PTV works better than dual-pulse in the sense of achieving better spatial resolution. For large curvature and strong acceleration (Case 8-12), the triple-pulse enhances the accuracy significantly in both velocity and position than dual-pulse PTV. It is also found that the performance of the quadruple-pulse PTV exceeds triple-ulse when the curvature is large and the acceleration is strong (Case 8-12). Comparing Case 9 and 10, as the acceleration increases, we see the quadruple-pulse PTV is able to achieve less position error while the velocity error is slightly smaller than that of the triple-pulse. The comparison between Case 11 and 12 indicates that the quadruple-pulse yields better spatial resolution for larger displacement while the velocity accuracy is slightly better. Lastly, the last two rows show two extreme cases. Case 13 is in the limit of straight trajectory and zero tangential acceleration. In such limit, we see the dual-pulse PTV performs better than multi-pulse

PTV. This further verifies the result shown in Case 3. Case 14 shows the error comparison when there is ideally zero locating error but the trajectory is strongly curved (large sweeping angle) and with strong tangential acceleration. In this case, we see the quadruple-pulse can significantly improve the velocity accuracy and achieve fairly good spatial resolution. Unfortunately, the zero locating error is not achievable in reality. The comparison in Case 14 also implies that the dominant error in realistic multi-pulse PTV measurement comes from the error in locating the center of the particle, i.e. $\langle |\delta \boldsymbol{X}_p|^2 \rangle$. Additionally, two cases (Case 2 and 7)are presented as comparisons to show the potential of multi-pulse PTV without the constraint of the particle displacement range. Case 2 is calculated and compared with Case 1 by releasing the limit on the particle displacement range. Likewise, Case 7 is calculated and compared to Case 6. From that we see with a large normalized displacement, the performance of multi-pulse PTV is significantly improved. In addition, in Case 2 the quadruple-pulse PTV can achieve much better spatial resolution than triple-pulse PTV. The Case 2 and 7 actually imply the great potential of multi-pulse PIV/PTV when the maximum measurable particle displacement can be extended significantly.

The comparison of acceleration and position errors for acceleration measurements is illustrated in Table 3.5. Case 1 shows the limit of straight trajectory with strong tangential acceleration. From that we see quadruple- and triple-pulse PTV can measure the tangential acceleration within 10% error of the full scale. Case 2 is generated with slight curvature and mild acceleration. It turns out that the acceleration measurement error is unacceptably high for such circumstance, and one should probably avoid measuring the acceleration of flow with very small curvature and acceleration. However, if we remove the constraint on the particle displacement range and extend that to 1.0 (Case 3), the performance of multi-pulse PTV in measuring acceleration is quite satisfactory. In addition, the quadruple-pulse is much better than triple-pulse

Case	Noise	Disp.	Accel.	Velocity error (%)			Position error (%)		
	$\sqrt{\langle\|\delta\boldsymbol{X}_p\|^2\rangle}\big/R$	$\dot{\vartheta}_0\Delta t$	$\ddot{\vartheta}_0\Delta t/2\dot{\vartheta}_0$	4-PTV	3-PTV	2-PTV	4-PTV	3-PTV	2-PTV
1	0.03%	0.02	0.2	2.94	1.52	1.52	0.032	0.030	0.100
2*	0.03%	0.5	0.2	0.22	0.28	2.48	0.037	0.35	5.09
3	0.05%	0.02	0	6.86	3.54	3.54	0.054	0.050	0.036
4	0.06%	0.04	0.3	2.57	1.35	1.35	0.065	0.060	0.300
5	0.5%	0.35	-0.2	6.53	4.12	4.12	0.54	0.50	2.03
6	0.5%	0.35	-0.3	9.80	6.84	6.84	0.54	0.50	2.74
7*	0.5%	1.0	-0.3	6.43	3.90	13.58	0.50	1.05	9.47
8	0.75%	0.5	0.3	2.59	2.92	3.59	0.81	0.82	6.4
9	1.0%	0.65	0.2	3.03	3.41	3.82	1.08	1.04	8.16
10	1.0%	0.65	0.4	2.46	2.74	5.76	1.09	1.57	11.91
11	1.25%	0.8	0.4	2.64	2.87	7.36	1.36	2.37	16.98
12	1.25%	1.0	0.4	2.62	2.64	9.75	1.38	3.74	25.1
13	1e-12	1e-10	0	2.74	1.41	1.41	1.08e-10	1.00e-10	7.07e-11
14	0 %	0.8	0.4	0.11	1.03	7.26	0.27	2.14	16.96

Table 3.4: Comparison of velocity and position error of velocity measurement between multi-pulse and dual-pulse PTV. Case 2, 7, 13 of 4-PTV is calculated using $t'/\Delta t$=0.87; other cases of 4-PTV are calculated using $t'/\Delta t$=0.75; Case 1, 3-6, 13 of 3-PTV use $t'/\Delta t$=0.5; other cases of 3-PTV use $t'/\Delta t$=0.78; 2-PTV is calculated using $t'/\Delta t$=0.5. The row with a star indicates the case when the particle displacement constraint is not considered.

PTV as shown in Case 3. In the case of large curvature and strong tangential acceleration (Case 5 and 8), the error percentage can be reduced to within 15%, and quadruple-pule PTV works slightly better than triple-pulse PTV. The comparison between Case 4 and 5 also indicates that the increase in displacement for cases with strong curvature and acceleration benefits the measurement, and so does the increase of tangential acceleration magnitude that is shown in Case 7 and 8. Further reduction of the error percentage is possible if we remove the constraint of the particle displacement range, as shown in Case 6. The last row evaluate the limit of zero locating noise

Case	Noise $\sqrt{\langle|\delta \boldsymbol{X}_p|^2\rangle}\big/R$	Disp. $\dot{\vartheta}_0\Delta t$	Accel. $\ddot{\vartheta}_0\Delta t/2\dot{\vartheta}_0$	Acceleration (%)		Position error (%)	
				4-PTV	3-PTV	4-PTV	3-PTV
1	1e-12	1e-10	0.6	7.5	8.16	8e-11	1e-10
2	0.03%	0.02	0.1	67.17	73.12	0.024	0.030
3*	0.03%	1.0	0.1	0.94	4.0	0.042	0.030
4	0.5%	0.35	0.3	18.69	20.29	0.4	0.5
5	0.5%	0.5	0.3	12.37	13.19	0.4	0.5
6*	0.5%	1.5	0.3	7.11	19.73	0.63	0.5
7	1.0%	0.7	0.1	17.85	19.37	0.8	1.0
8	1.0%	0.7	-0.4	12.55	13.51	0.8	1.0
9	0 %	0.8	0	0.09	1.33	0.006	0

Table 3.5: Comparison of acceleration and position error of acceleration measurement between multi-pulse and dual-pulse PTV. $t'/\Delta t$=0.5 is used for all except Case 3 and 8 of 4-PTV are calculated using $t'/\Delta t$=0.71. The row with a star indicates the case when the particle displacement constraint is not considered.

and zero tangential acceleration, i.e. it accounts for only the centrifugal acceleration. The error percentage is quite satisfactory, and the quadruple-pulse seems better in handling the centrifugal acceleration. But again the zero locating noise is hardly to achieve.

Chapter 4

MULTI-PULSE PIV EXPERIMENT

4.1 Registration error correction

4.1.1 Method description

As discussed previously, the multi-pulse technique is designed to offer better resolution of the particle motion and thus enhance the velocity and acceleration measurement accuracy. In order to satisfy the temporal and spatial scale of various types of flows, the multi-pulse system must be able to generate laser pulse sequence and record image sequence with very short time separations. The conventional dual-pulse PIV camera is manufactured with additional electron storage units so that two consecutive frames can be recorded and transfered with very short time delay. Unfortunately there hasn't been such single-CCD camera conceived perfectly for at least three-frame recording scheme.

In present multi-pulse system, the image recording is realized by a beam-splitting ultra-high-speed camera (HSFC-Pro) with four individual imaging channels. Each channel consists of a 1.3 MP CCD and a micro-channel intensifier that serves as a fast shutter. Light rays go through the lens and are split by optical beam splitters into each imaging channel. Ideally, all four imaging channels can record identical images simultaneously despite the electrical noise. However, in the presence of the misalignment between CCDs, the distortion from different optical beam splitters, and mounting errors of the beam splitters, the registration error in current system is found to be comparable to particle image size, i.e. 2-3 pixels. Such error could significantly pollute the particle displacement measurement when images from different CCDs are

interrogated. An image registration procedure seems necessary to correct the registration error before interrogation and thus benefit multi-pulse PTV/PIV measurements.

In the image processing field, one robust and widely-used technique to register images taken from different circumstances is the so-called control point mapping technique (Brown, 1992). The idea is to firstly identify some features in the image pair as control points, followed by fitting a global mapping function to map control points in the reference image to those in the image to be registered. This technique features with generality and is able to provide a smooth transform over the entire image domain. Usually, the control points could be landmarks in satellite images, or biological tissues in medical images. In PIV measurements, the particles scattered over the entire image serve perfectly as control points. Wieneke (2005) discussed the implementation of correcting the error introduced by the misalignment between the calibration target plane and the laser light sheet in stereoscopic PIV measurements. In his work, the discrepancy map was obtained using simultaneously recorded particle images from two cameras.

In present work, the discrepancy map between CCDs is obtained from the ensemble average of the cross-correlation results of simultaneously recorded images. The mapping function that maps the reference image grid to the corresponding locations on the other image is a combination of the polynomial mapping model proposed by Soloff *et al.* (1997), and the bivariate polynomial model discussed by Brown (1992). The implementation is described as the following.

1. Cross-correlate simultaneously recorded particle images from different CCDs. Ensemble-average the correlation results, i.e. the individual discrepancy vector fields, to obtain a noiseless and reliable discrepancy map e on the reference grid $\boldsymbol{X}_{ref}$.

2. A mapping function $\boldsymbol{F}$ is fitted in the least square sense to map the reference grid, $\boldsymbol{X}_{ref}$, on the reference image to the corresponding grid positions, $\boldsymbol{X}_{ref}+\boldsymbol{e}$, on the other image, i.e. $\boldsymbol{X}_{ref}+\boldsymbol{e} = \boldsymbol{F}(\boldsymbol{X}_{ref})$. The form of the mapping function is proposed as:

$$\boldsymbol{F}(X,Y) = \frac{\boldsymbol{a}_1}{X^2} + \frac{\boldsymbol{a}_2}{XY} + \frac{\boldsymbol{a}_3}{Y^2} + \frac{\boldsymbol{a}_4}{X} + \frac{\boldsymbol{a}_5}{Y}$$
$$+ \boldsymbol{a}_6 + \boldsymbol{a}_7 X + \boldsymbol{a}_8 Y + \boldsymbol{a}_9 X^2 + \boldsymbol{a}_{10} XY + \boldsymbol{a}_{11} Y^2 \qquad (4.1)$$

where $\boldsymbol{a}_i$ are coefficient vectors to be determined.

3. Define the pixel grid, $\boldsymbol{X}_{pix}$, on the reference image. Calculate the mapped pixel grid $\boldsymbol{F}(\boldsymbol{X}_{pix})$. Re-sample the image to be registered at the mapped pixel grid. In other words, the image is deformed to eliminate the registration error with respect to the reference image. In our test, the use of cubic-spline interpolation for re-sampling images yields good accuracy.

4. Images from different CCDs are re-sampled with respect to a reference CCD before being analyzed by cross-correlation or particle identification.

4.1.2   Registration error correction test

The method for registration correction is tested with particle images recorded simultaneously by different CCDs of the HSFC-Pro camera. Here the images of CCD#3 are considered as the reference as the light rays pass through the least number of beam splitters to reach CCD#3. In this test, the images of CCD#1 are to be registered with respect to the reference images. The correlation results of 500 image pair samples are averaged to calculate the discrepancy map, $\boldsymbol{e}$, shown in Figure 4.1a. The pattern of the discrepancy vector field indicates the misalignment is sort of rotation plus some distortions. A 2-D mapping function $\boldsymbol{F}(X,Y)$, whose form is

given in Equation (4.1), is fitted in a least-square fashion to represent the discrepancy between CCD#1 and #3. The fitting residual ϵ, which is defined as

$$\epsilon \triangleq |\boldsymbol{F}(\boldsymbol{X}_{ref}) - \boldsymbol{X}_{ref} - \boldsymbol{e}| \qquad (4.2)$$

is calculated and plotted in Figure 4.1b. From that plot we see the mapping function can well represent the discrepancy with the fitting residual less than 0.2 pixels.

A further test on the performance of the registration correction is conducted by deforming the images of CCD#1 using the mapping function followed by cross-correlation with the reference images. Again, 500 image pair samples are registered, correlated and averaged. The outcome is considered as the residual error after the correction of registration error, which indicates the performance of the proposed mapping function model. As we see from the probability density function of the residual error in Figure 4.2b, the error mostly concentrates in the range of -0.03~0.03 pixels. The global mean of the residual error in X is -0.011 pixels and the standard deviation is 0.021 pixels. The global mean of the residual error in Y is -0.010 pixels and the standard deviation is 0.018 pixels. Some large values are observed close to the corners and the borders of the field of view, as shown in Figure 4.2a. This is acceptable since for more than 95% area in the center we eliminate the registration error with good accuracy.
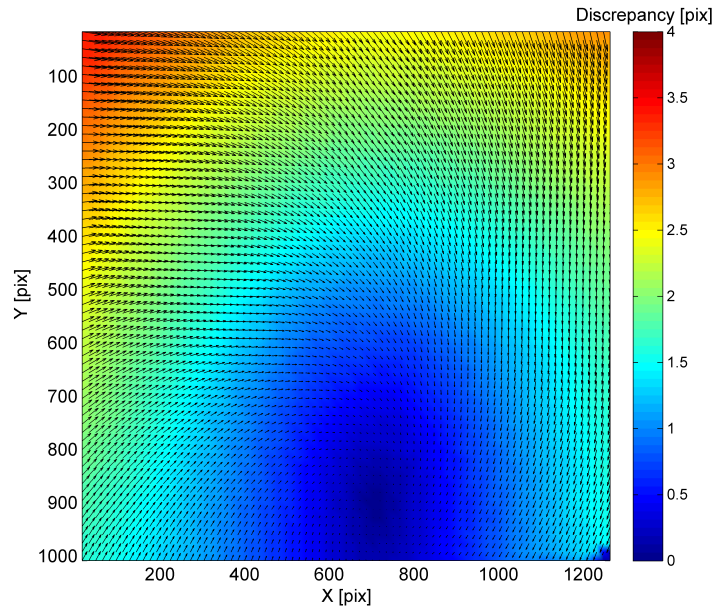
(a) discrepancy map
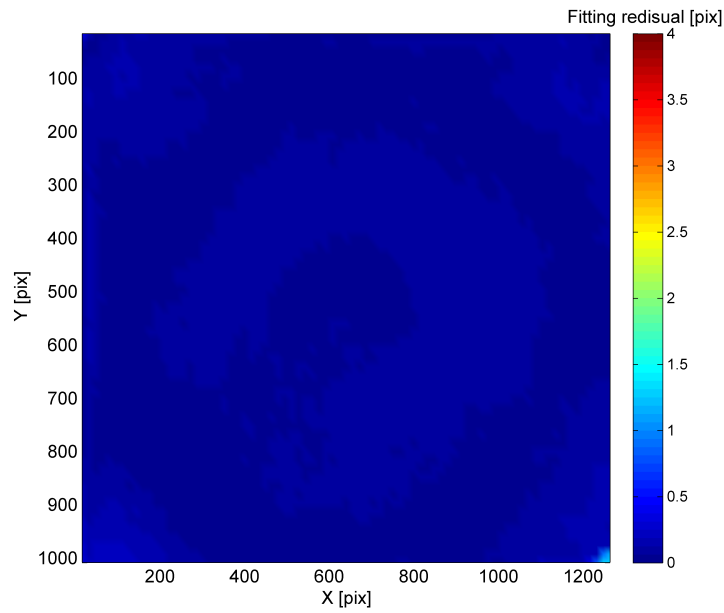
(b) fitting residual

Figure 4.1: The discrepancy map and the mapping function fitting residual.
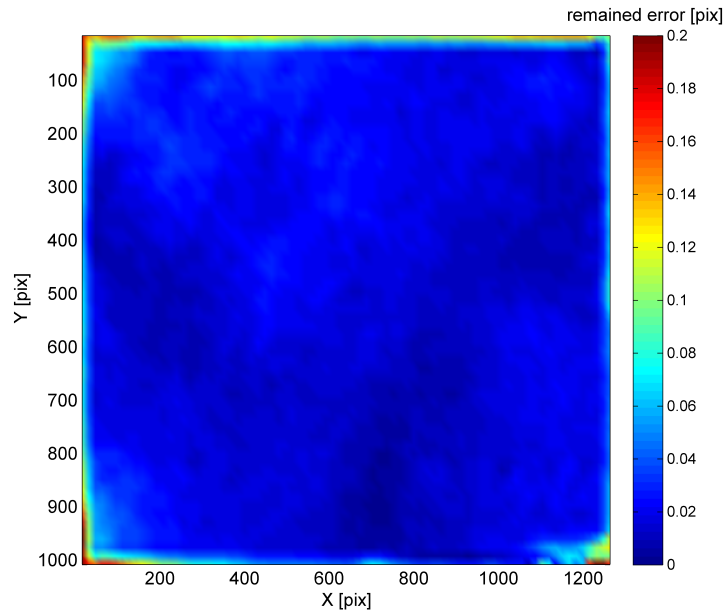
(a) residual error
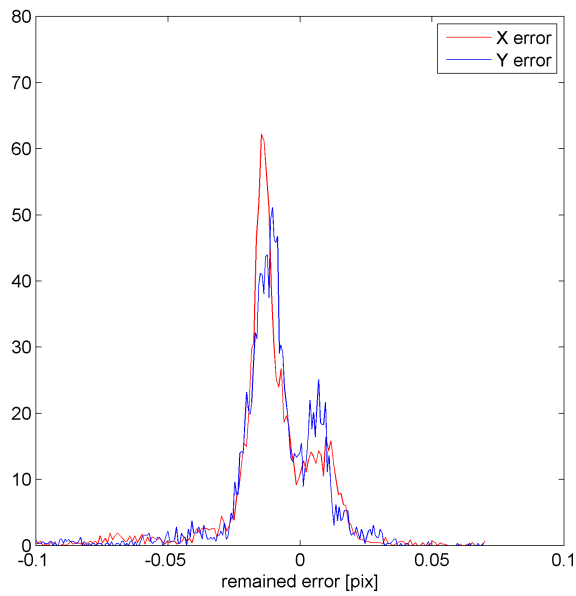
(b) residual error pdf

Figure 4.2: Residual error after the registration correction.

4.2   Impinging jet experiment

In this section, the triple-pulse experiment is illustrated and the velocity and acceleration measurements are presented. Instead of tracking individual particles, cross-correlation-based PIV technique is implemented to measure the particle group displacement between neighboring frames. This is a good approximation given the flow field of the jet doesn't exhibit strong spatial displacement gradient within the area of a interrogation spot.

4.2.1   experimental setup

The experiment is conducted to measure a round impinging air jet at $Re \approx 3000$. The flow along the centerline of the jet has a strong deceleration as it approaches the stagnation point. This is the flow region that we investigate to test the capability of triple-pulse technique to measure accelerations.

A schematic of the multi-pulse PIV system is shown in Figure 4.3. To satisfy the requirement of short time delay, a custom 8-pulse Nd:YAG laser system is utilized to produce eight independently-triggered $532nm$ laser pulses. All eight laser beams are co-linearly combined by beam-combining optics in front of the four dual-cavity laser heads. The optical beam combining system is designed to achieve identical optical path lengths and over 90% overlap of all laser beams. Two 8-channel BNC565 Pulse Generators are used to trigger flash lamps and Q-switches respectively, so that we have good flexibility and accuracy in the timing control. Particle images are recorded by HSFC-Pro, which consists of four individual imaging channels and four 1.3MP CCD chips. The image is split by the integrated beam splitter system that ensures equal optical path lengths for each channel. This imaging architecture makes it possible to straddle different frames on different CCDs with acceptable registration errors. The
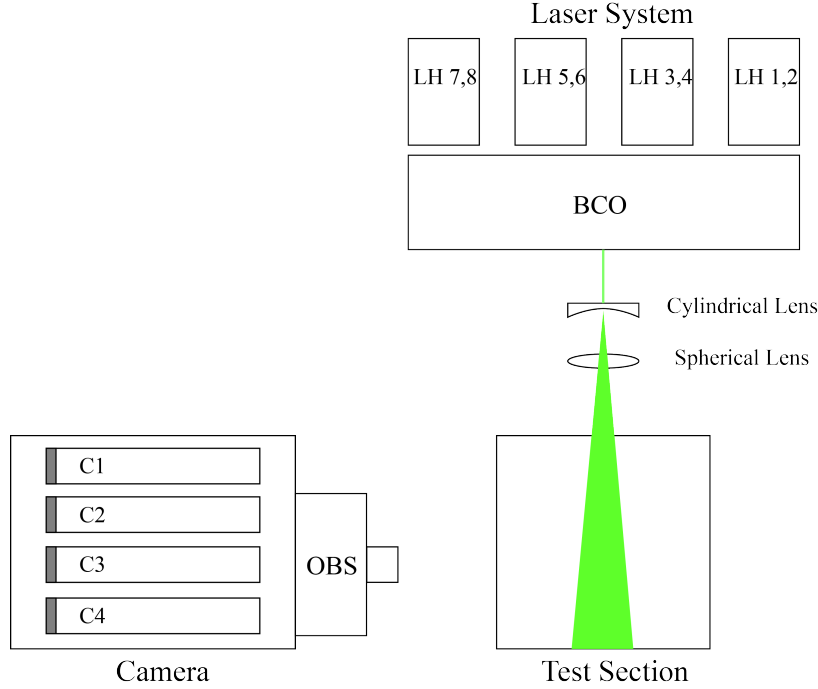
Figure 4.3: Schematic of the multiple-pulse PIV system. OBS:optical beam splitter; BCO: beam combining optics; LH: laser head.

refined registration correction is realized by the method described above. Another BNC565 Pulse Generator combined with a SRS DG535 unit is used to synchronize the laser pulses and the exposures of the camera.

The impinging air jet is measured using triple-pulse PIV. The centerline of the jet is normal to the impinging plate within experimental tolerance. A schematic of the test section is shown in Figure 4.4. The laser sheet is aligned with the axis of symmetry of the jet. The diameter D of the exit nozzle is $21.59mm$. The nozzle is mounted with about $H = 4D$ above the impinging plate. An area of 960 by 672 pixels is cropped out of the original image, which corresponds to $3.00D(w) \times 2.10D(h)$ region of interest in the physical space right above the impinging plate. DEHS (Di-Ethyl-Hexyl-Sebacat) aerosol generated by Laskin nozzle is used as tracer particles. The lateral magnification is about 0.10 and the effective f-number is about 20. The
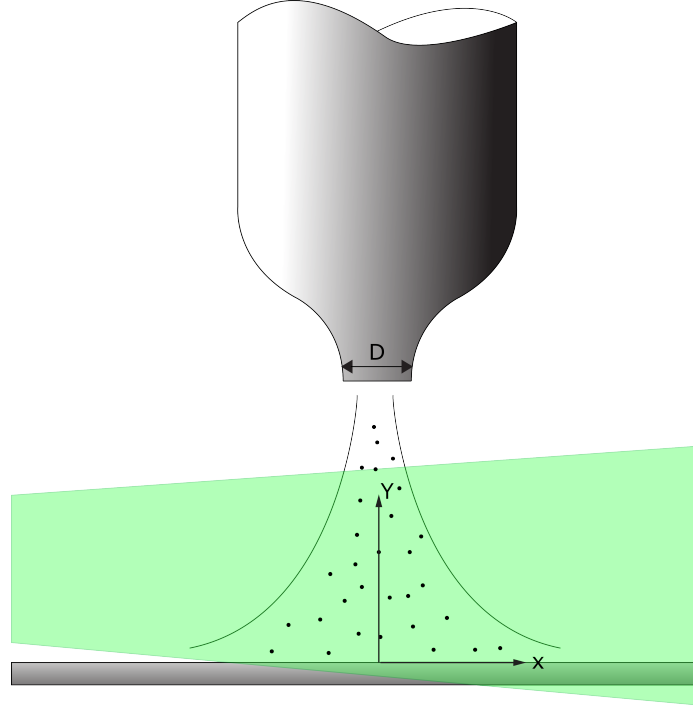
Figure 4.4: Schematic of the impinging jet test section

time separation Δt between pulses 1 and 3 is 80 μs.

The particle images are processed by cross-correlation to determine the displacement fields. Multi-grid interrogation scheme is utilized to achieve the final interrogation window size of 48×48 pixels, corresponding to $3.24mm \times 3.24mm$ in the physical space. Interrogation windows are sampled with 75% overlap of the window size. Window-offset with fractional pixel numbers is used to reduce the displacement RMS error (Adrian and Westerweel, 2011). Each interrogation window is weighted by a window function to eliminate the particle cropping effect near the edges as well as to increase the effective spatial resolution. The window weight function applied here is with 1 for the one-quarter area in the center and decays to the edge in a cosine way (Figure 4.5). A Gaussian low-pass filter with kernel size 5×5 and standard deviation 1.8 is used in the intermediate steps and in the post-smoothing.
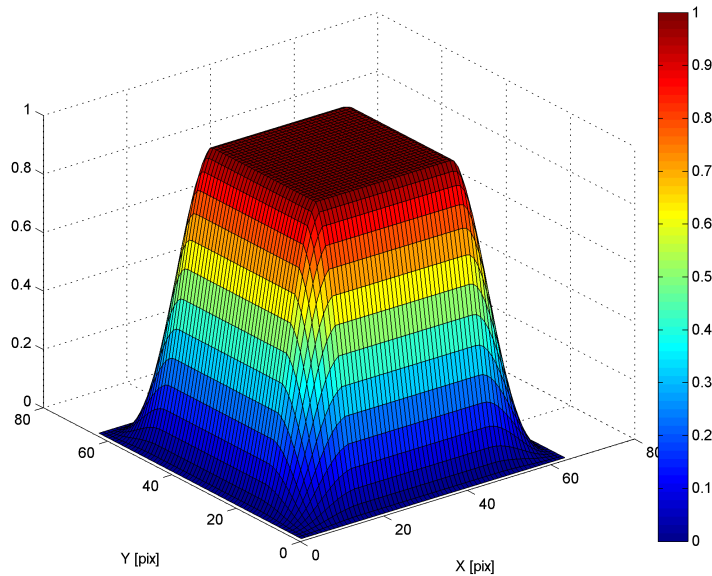
Figure 4.5: Window weight function applied to interrogation spots, with 1 in the center region and decaying by cosine to the edges.

4.2.2 velocity and acceleration measurements

In previous chapters, the multi-pulse measurement is discussed in terms of measured particle locations. However, in the experiment the cross-correlation directly outputs the particle displacement field. In this work, the correlation analysis is performed from frame 2 to 1, and from frame 2 to 3, respectively, to effectively resolve particle locations at three pulse times. This backward-forward correlation scheme (see Figure 4.6) has the benefit of attenuating the degradation of the correlation due to loss-of-pair effect when a relatively long Δt is used. As a comparison, if the correlation is performed on frame 1 to 2 and frame 1 to 3, the latter one would have higher percentage of invalid vectors because stronger out-of-plane motion is introduced by setting a longer Δt. Additionally, as suggested in Table 2.5, the optimized velocity and acceleration measurements are achieved at $t'/\Delta t = 0.5$, and assigned to the corresponding locations, i.e. the locations where the particles appear on frame 2. In other
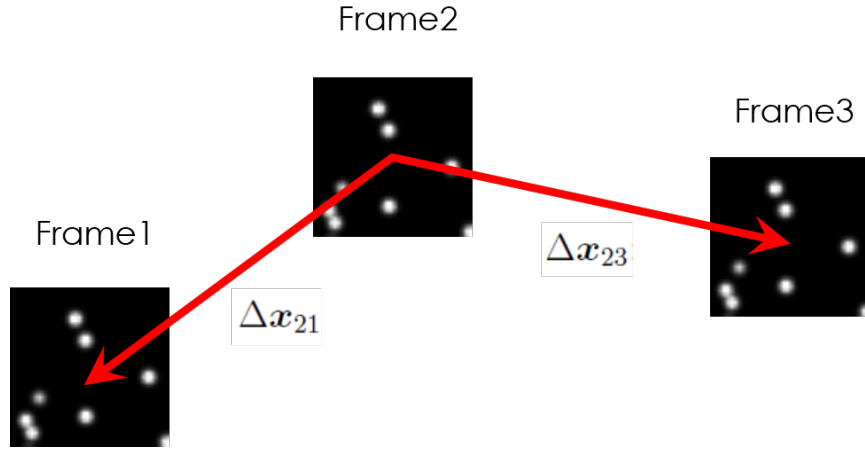
Figure 4.6: Schematic of the backward-forward correlation scheme. The correlation is computed from frame 2 to 1, and frame 2 to 3, respectively.

words, by starting the correlation from the center frame, the optimized measurements are achieved automatically on a regular grid, while for most other implementations additional interpolation needs to be performed to interpolate the scattered data onto a regular grid.

Figure 4.7 illustrates the comparison of the mean velocity fields measured by triple-pulse PIV and dual-pulse PIV. The triple-pulse measurement in Figure 4.7a is calculated using the optimization stated in Table 2.5, i.e. $t'/\Delta t$=0.5. The dual-pulse PIV velocity field is calculated using the correlation result of frame 2 and 3. The spatial coordinates are normalized by the diameter of the exit nozzle, D. The similarity of the comparison verifies the capability of triple-pulse PIV for velocity measurement. From the velocity magnitude contour, we see that the mean velocity field is symmetric with respect to the centerline. The velocity magnitude decays as it goes further away from the centerline. The flow decelerates along the vertical direction as it approaches the impinging plate.

To verify the capability of triple-pulse PIV for acceleration measurement, the ensemble-averaged centerline acceleration profile is calculated and compared. Con-

sidering the flow is statistically stationary, as the temporal derivative vanishes, the fluid material derivative, i.e. the fluid parcel Lagrangian acceleration is given by:

$$\frac{D\boldsymbol{u}}{Dt} = \boldsymbol{u} \cdot \nabla \boldsymbol{u} \tag{4.3}$$

where $\boldsymbol{u} = (u_x, u_y, u_z)$. Along the jet centerline, the mean flow is unidirectional, i.e. $\langle u_{xc}\rangle = \langle u_{zc}\rangle = 0$. Furthermore, because of the symmetry of the mean field, the derivatives of any quantities at centerline with respect to x and z vanish. Therefore, the mean centerline acceleration along y-axis is given by

$$\langle \frac{Du_{yc}}{Dt}\rangle = \frac{1}{2}\frac{\partial\langle u_{yc}\rangle^2}{\partial y} + \frac{1}{2}\frac{\partial\langle u_{yc}'^2\rangle}{\partial y} \tag{4.4}$$

where the centerline velocity u_{yc} is decomposed into the mean $\langle u_{yc}\rangle$ and the fluctuation u_{yc}', i.e. $u_{yc} = \langle u_{yc}\rangle + u_{yc}'$. Equation (4.4) implies that the jet mean centerline acceleration can be calculated from the spatial derivatives of the mean centerline velocities and its RMS fluctuations. Here we use the dual-pulse PIV measurement of frame 2 and 3 to compute (4.4) as the ground truth. A 8th polynomial is fit to represent the quantity $\langle u_{yc}\rangle^2 + \langle u_{yc}'^2\rangle$ in Equation (4.4). The centerline acceleration is then obtained by analytically differentiating the fitted polynomial. On the other hand, the acceleration is also computed by triple-pulse method given in Equation (2.11), and compared to the ground truth. For convenience, Equation (2.11) is rewritten in physical space in terms of the displacement from frame 2 to 1, $\Delta\boldsymbol{x}_{21}$, and the displacement from frame 2 to 3, $\Delta\boldsymbol{x}_{23}$:

$$\ddot{\boldsymbol{x}}_p = 2\frac{\alpha\Delta\boldsymbol{x}_{23} + (1-\alpha)\Delta\boldsymbol{x}_{21}}{\alpha(1-\alpha)\Delta t^2} \tag{4.5}$$

The centerline acceleration comparison is presented in Figure 4.8. The blue triangles are triple-pulse acceleration measurements and solid black line denotes the ground truth of the mean centerline acceleration profile. Observed from that, the

flow maintains zero acceleration for approximately $y/D > 1.0$. As it approaches the impinging plate, the acceleration sharply increases to the maximum at approximately y/D=0.2, and then dramatically decreases within a thin layer above the plate. Note that the decelerating flow has positive acceleration since the y-axis is pointing up and the flow is downward. Generally speaking, the triple-pulse measurement shows good agreement with the ground truth, especially for $0.1 < y/D < 0.8$ where the flow exhibits strong deceleration. For the thin layer above the plate, $y/D < 0.1$, the triple-pulse data don't decrease as rapidly as shown by the ground truth. This is considered as the consequence of using finite interrogation windows to resolve the flow within such small scales. In the experiment, the thin layer, $y/D < 0.1$, corresponds to a 2.1mm thick layer, whereas the interrogation window size is around 3.2mm and the data spacing is 0.8mm. It turns out to be a tough case since it tries to resolve the flow with strong gradient within the length of one single interrogation window. Usually, micro-PIV works properly to resolve the flow within small scales, such as turbulent boundary layers. Another observation from Figure 4.8 is that the triple-pulse measurement exhibits bias errors toward negative values for the constant velocity region, $y/D > 0.8$. The maximum difference in this region is around $1500m/s^2$, which is around 10% of the full-scale acceleration. The $1500m/s^2$ error corresponds to an error of 0.018 pixels in the displacement measurement for $\Delta\boldsymbol{x}_{23}$ and $\Delta\boldsymbol{x}_{21}$ in Equation (4.5). This error is acceptably small in PIV experiments. It is also noted that the residual registration error, shown in Figure 4.2b, is of the same level as 0.018 pixels. This indicates that the bias error might be introduced by the residual misalignment between CCDs.

One of the instantaneous acceleration fields is shown in Figure 4.9. The vector field is validated by the normalized median test (Westerweel and Scarano, 2005) over a 5-by-5 neighborhood and with the threshold of 2, and smoothed by a Gaussian low-

pass filter with 5×5 kernel and standard deviation of 2. Some physical aspects of the jet can be extracted from the instantaneous acceleration field. Strong deceleration is observed near the stagnation point, $x/D = 0$. As the flow approaches the plate, it separates to both sides, and the acceleration field indicates the centrifugal acceleration associated with the separating flow. Also, the pattern of the acceleration field shows the entrainment of the ambient air into the jet. It is not surprised that the instantaneous acceleration field is noisy, because the acceleration measurement is quite sensitive to the error in detecting the particle displacement as discussed above. From the previous analysis for the acceleration measurement, the potential improvement could be achieved by setting a longer Δt and thus extend the particle displacement. The realization of the potential requires robust technique to search larger regions for the displaced particles.
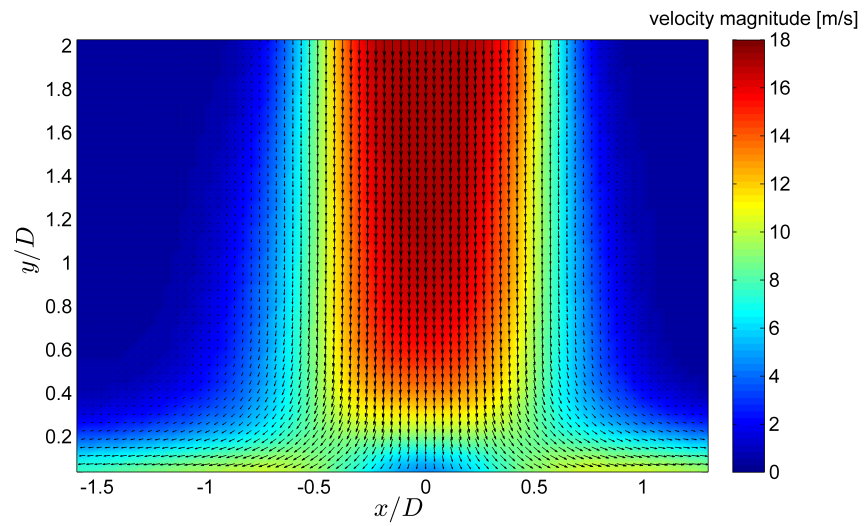
(a) Triple-pulse
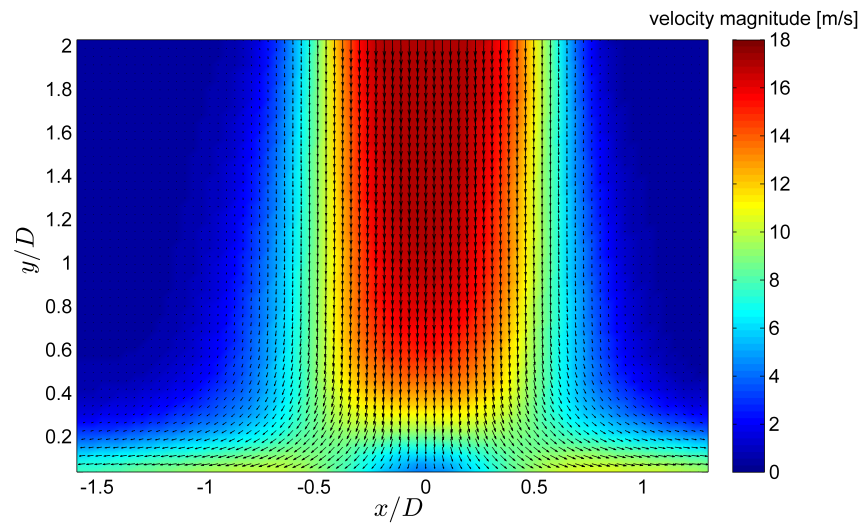
(b) Dual-pulse

Figure 4.7: Comparison of mean velocity fields of (a) triple-pulse PIV and (b) dual-pulse PIV
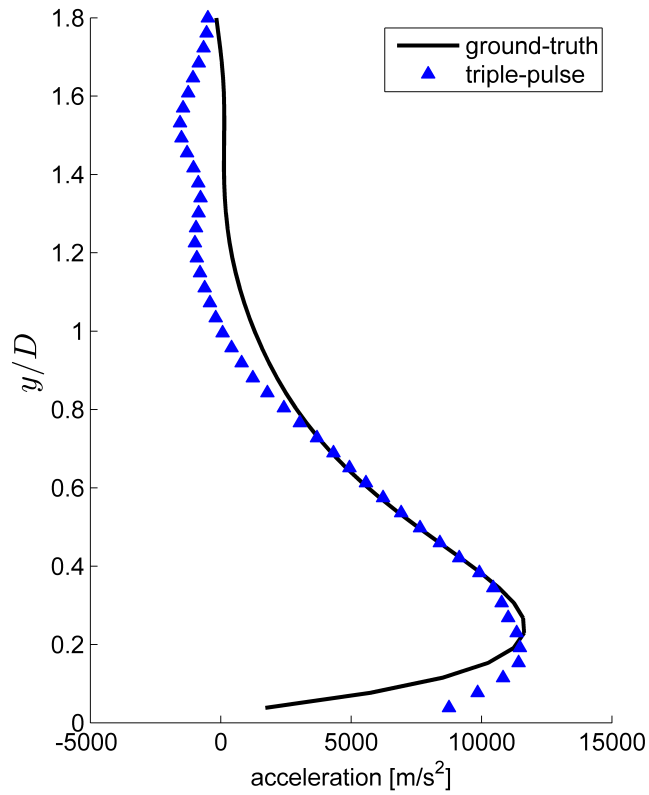
Figure 4.8: Comparison of mean centerline acceleration. Black solid line: ground truth from dual-pulse PIV; Blue triangles: acceleration measurement by triple-pulse PIV.
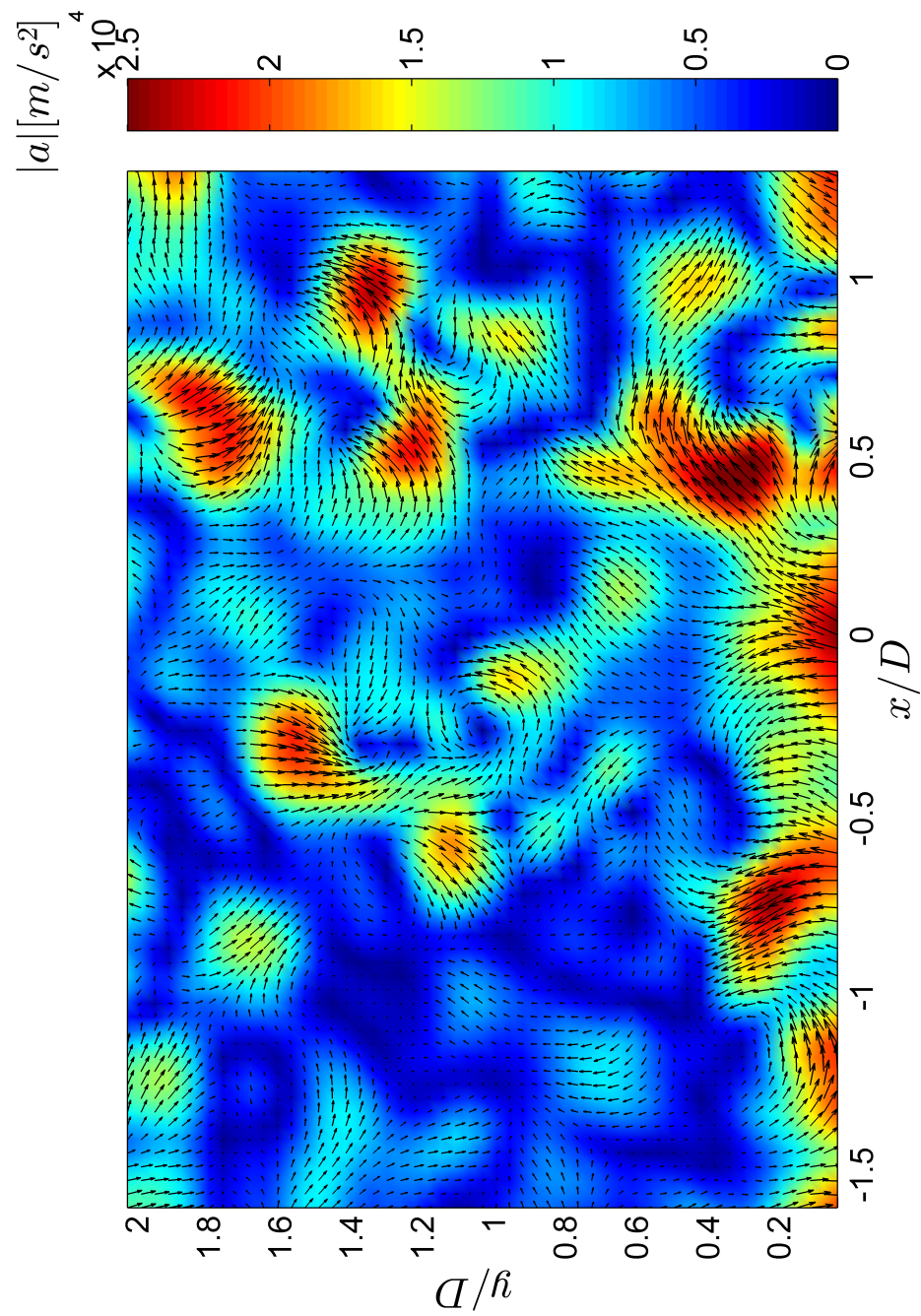
Figure 4.9: Instantaneous acceleration field of the jet measured by triple-pulse PIV

Chapter 5

SUMMARY

Multi-pulse PIV/PTV is a recently proposed technique aiming at better resolution of the particle motion. In principle, the dynamic range of current PIV systems can be extended by adding pulses in between to resolve the curvilinear particle trajectory and the velocity variation. In addition, multi-pulse techniques offer direct measurement of the acceleration field, opening the way to calculating fluid forces and correcting for particle inertial lag.

In this study, the performances of triple- and quadruple-pulse PTV are numerically evaluated in terms of the RMS errors in position, velocity and acceleration, by assuming the particle travels along a locally circular path. The analysis is conducted in two scenarios. Firstly we consider the particle displacement within the range that is considered to be optimal for most current PIV systems. We define two cost functions as the combined error in position and velocity, and the combined error in position and acceleration, for velocity and acceleration measurements, respectively. The evaluation of the cost functions accounts for the accuracy of assigning a velocity or acceleration measurement to an Eulerian position in the fluid. By finding the $t'/\Delta t$ that minimizes the cost functions, the optimizations for velocity and acceleration measurements are achieved. Secondly, the scope of the analysis is extended to explore a wider range of the particle displacement. The extension of the maximum measurable particle displacement has the potential to increase the accuracy and dynamic velocity range of PIV/PTV measurements. The optimizations are achieved in the same way as in the first scenario. Also, the optimal $t'/\Delta t$ behaves differently when we release the constraint on the particle displacement range. The performances

of quadruple-, triple- and dual-pulse PTV are then comprehensively compared for different flow conditions. It is found that for the case with nearly straight trajectory and mild tangential acceleration, dual-pulse PTV still offers the best accuracy. As the acceleration, the normalized displacement and the noise level increase, multi-pulse PTV works substantially better than dual-pulse PTV. Furthermore, the quadruple-pulse PTV performs better than triple-pulse in the cases with even stronger acceleration and even larger normalized displacement. It is also found that the error percentage of both velocity and acceleration can be substantially reduced if the measurement of much larger particle displacements is achievable. The extent to which displacements can be increased depends on additional factors such as out-of-plane displacement and the computational cost of searching larger regions for the displaced particles.

Experimentally, the triple-pulse technique is tested by correlation-based PIV with backward-forward correlation scheme. The experiment measures the velocity and acceleration fields of a steady, impinging air jet. A multi-pulse PIV system consisting of a custom 8-pulse laser system and a high-speed beam-splitting camera is used because it was available and it offered completely flexibility in timing the pulses. To correct the registration error between CCDs, an image registration technique is developed and tested based on fitting the global mapping function. The residual root mean square error after registration correction is found to be under 0.03 pixels.

Comparison of the mean velocity fields measured by triple-pulse PIV and dual-pulse PIV, respectively, shows good agreement. The mean acceleration profile along the jet centerline is calculated in two ways. Firstly, since the flow is statistically stationary, the mean centerline acceleration can be calculated via the spatial derivatives of mean centerline velocity obtained from dual-pulse PIV measurements. This is considered as the ground truth for the comparison. Secondly, the centerline acceleration profile is measured by triple-pulse acceleration estimator. The comparison

74

between the two methods has good consistency, which verifies the capability of triple-pulse technique for acceleration measurement. The maximum mean acceleration error shown in the comparison corresponds to 0.018-pixel error of the displacement measurement, which is within the acceptable range of ordinary PIV measurements. This amount of error might also be associated with the residual registration error between CCDs. An instantaneous acceleration field of the jet is presented, which reveals some physical aspects, such as the deceleration near the plate, the flow separation, and the entrainment of ambient fluid into the jet.

In conclusion, the introduction of third and fourth pulses to the PIV technique has been shown to increase accuracy in the measurement of position and velocity, and to offer a means for direct measurement of instantaneous acceleration fields. Further work will be needed to refine the technique before its full potential can be realized.

REFERENCES

Adrian, R. J., "Particle-imaging techniques for experimental fluid mechanics", Annual review of fluid mechanics **23**, 1, 261–304 (1991).

Adrian, R. J., "Dynamic ranges of velocity and spatial resolution of particle image velocimetry", Measurement Science and Technology **8**, 12, 1393 (1997).

Adrian, R. J., "Twenty years of particle image velocimetry", Experiments in fluids **39**, 2, 159–169 (2005).

Adrian, R. J. and J. Westerweel, *Particle image velocimetry* (Cambridge University Press, 2011).

Boillot, A. and A. Prasad, "Optimization procedure for pulse separation in cross-correlation piv", Experiments in fluids **21**, 2, 87–93 (1996).

Brown, L. G., "A survey of image registration techniques", ACM computing surveys (CSUR) **24**, 4, 325–376 (1992).

Christensen, K. and R. Adrian, "Measurement of instantaneous eulerian acceleration fields by particle image accelerometry: method and accuracy", Experiments in fluids **33**, 6, 759–769 (2002).

Farrugia, N., S. Kanne and D. Greenhalgh, "Three-pulse digital particle image velocimetry", Optics letters **20**, 17, 1827–1829 (1995).

Hain, R. and C. Kähler, "Fundamentals of multiframe particle image velocimetry (piv)", Experiments in fluids **42**, 4, 575–587 (2007).

Haranandani, G., "Optimization and accuracy of 3-pulsed particle tracking velocimetry", MSE Proj. Rep., Arizona State Univ (2011).

Keane, R., R. Adrian and Y. Zhang, "Super-resolution particle imaging velocimetry", Measurement Science and Technology **6**, 6, 754 (1995).

Keane, R. D. and R. J. Adrian, "Optimization of particle image velocimeters: II. multiple pulsed systems", Measurement science and technology **2**, 10, 963 (1991).

Lynch, K. and F. Scarano, "A high-order time-accurate interrogation method for time-resolved piv", Measurement Science and Technology **24**, 3, 035305 (2013).

Scarano, F., K. Bryon and D. Violato, "Time-resolved analysis of circular and chevron jets transition by tomo-piv", 15th Int Symp on Applications of Laser Techniques to Fluid Mechanics, Lisbon, Portugal, 05-08 July (2010).

Sciacchitano, A., F. Scarano and B. Wieneke, "Multi-frame pyramid correlation for time-resolved piv", Experiments in fluids **53**, 4, 1087–1105 (2012).

Soloff, S. M., R. J. Adrian and Z.-C. Liu, "Distortion compensation for generalized stereoscopic particle image velocimetry", Measurement science and technology **8**, 12, 1441 (1997).

Westerweel, J., G. E. Elsinga and R. J. Adrian, "Particle image velocimetry for complex and turbulent flows", Annual Review of Fluid Mechanics **45**, 409–436 (2013).

Westerweel, J. and F. Scarano, "Universal outlier detection for piv data", Experiments in Fluids **39**, 6, 1096–1100 (2005).

Wieneke, B., "Stereo-piv using self-calibration on particle images", Experiments in Fluids **39**, 2, 267–280 (2005).

APPENDIX A

MATLAB SCRIPTS: ERROR CALCULATION OF PARTICLE POSITION, VELOCITY AND ACCELERATION

A.1   Triple-pulse calculation

```
%        MS Thesis Script Appendix - Triple-Pulse PTV
%
%        t_bar         - normalized time                   [1]
%          s           - normalized displacement           [1]
%          q           - acceleration factor               [1]
%          u           - center location uncertainty       [100%]
%        d_tau         - particle diameter                 [mm]
%          R           - radius of curvature               [mm]
%          a           - alpha                             [1]
%         eta          - wighting factor                   [1]
%      sigma_x_bar     - normalized postiion rms error     [1]
%      sigma_v_bar     - normalized velocity rms error     [1]
%      sigma_a_bar     - normalized acceleration rms error [1]


clc,clear all,close all

N=1000;
M=1000;
t_bar=linspace(0,1,N)';
d_tau=22.5e-03;
R=2;
a=1/2;
eta=1/2;
path='E:\Research\Multi-pulse PIV\PTV Simulation\MS Thesis Figures 3pulse\';
for q=[-0.3 -0.1 eps 0.2 0.4]
    for u=[0.03 0.075 0.15 0.5 0.75 1]*1e-02

        s=linspace(10/(0.3/u),30/(0.3/u),1000);

        filename=sprintf('q%+04du%+07d',round(q*100),round(u*100000));

        Ax=zeros(N,M);
        Bx=zeros(N,M);
        C1x=zeros(N,M);
        C2x=zeros(N,M);
        C3x=zeros(N,M);
        for i=1:M
            Ax(:,i)=(1/a/(1-a)*t_bar-1/a/(1-a)*t_bar.^2)...
                *(1-cos(a*s(i)+a^2*q*s(i)))...
                -(a/(1-a)*t_bar-1/(1-a)*t_bar.^2)*(1-cos(s(i)+q*s(i)))...
                -(1-cos(s(i)*t_bar+s(i)*q*t_bar.^2));
            Bx(:,i)=(1/a/(1-a)*t_bar-1/a/(1-a)*t_bar.^2)...
                *sin(a*s(i)+a^2*q*s(i))...
                -(a/(1-a)*t_bar-1/(1-a)*t_bar.^2)*sin(s(i)+q*s(i))...
                -sin(s(i)*t_bar+s(i)*q*t_bar.^2);
            C1x(:,i)=1-(1+a)/a*t_bar+1/a*t_bar.^2;
            C2x(:,i)=1/a/(1-a)*t_bar-1/a/(1-a)*t_bar.^2;
            C3x(:,i)=-a/(1-a)*t_bar+1/(1-a)*t_bar.^2;
        end
        sigma_x_bar=sqrt(Ax.^2+Bx.^2+(C1x.^2+C2x.^2+C3x.^2)*u^2);
        figure
        pcolor(s,t_bar,sigma_x_bar)
        hold on
        axis square
        axis xy
```

```
shading interp
hx=xlabel('$\dot{\vartheta_0}\Delta t$',...
'interpreter','latex','Fontsize',12);
%set(hx,'Position',[0.50 -0.06]);
hy=ylabel('$t^\prime/\Delta t$','interpreter','latex','Fontsize',12);
%set(hy,'Position',[-0.06 0.5]);
%set(gca,'XTick',0.05:0.1:0.95,'YTick',0:0.1:1);
set(gca,'FontSize',12);
hc=colorbar;
[clim1,clim2]=newclim(sigma_x_bar,0,0.2);
caxis([clim1,clim2])
ht=title(hc,'$\sigma_x/R$','interpreter','latex','Fontsize',12);
set(ht,'Position',[0 clim2+(clim2-clim1)*0.03]);
[C,h]=contour(s,t_bar,sigma_x_bar,linspace(clim1,clim2,10),'k--');
clabel(C,h);
% print(gcf,[path,'sigma_x_',filename,'.pdf'],'-dpdf','-r300');
% print(gcf,[path,'sigma_x_',filename,'.eps'],'-depsc ','-r300');
% print(gcf,[path,'sigma_x_',filename,'.png'],'-dpng','-r300');

Av=zeros(N,M);
Bv=zeros(N,M);
C1v=zeros(N,M);
C2v=zeros(N,M);
C3v=zeros(N,M);
for i=1:M
    Av(:,i)=((1/a/(1-a)/s(i)-2/a/(1-a)*t_bar/s(i))...
        *(1-cos(a*s(i)+a^2*q*s(i)))...
        -(a/(1-a)/s(i)-2/(1-a)*t_bar/s(i))*(1-cos(s(i)+q*s(i)))...
        -(sin(s(i)*t_bar+s(i)*q*t_bar.^2).*(1+2*q*t_bar)))/(1+2*q);
    Bv(:,i)=((1/a/(1-a)/s(i)-2/a/(1-a)*t_bar/s(i))...
        *sin(a*s(i)+a^2*q*s(i))...
        -(a/(1-a)/s(i)-2/(1-a)*t_bar/s(i))*sin(s(i)+q*s(i))...
        -cos(s(i)*t_bar+s(i)*q*t_bar.^2).*(1+2*q*t_bar))/(1+2*q);
    C1v(:,i)=(-(1+a)/a/s(i)+2/a*t_bar/s(i))/(1+2*q);
    C2v(:,i)=(1/a/(1-a)/s(i)-2/a/(1-a)*t_bar/s(i))/(1+2*q);
    C3v(:,i)=(-a/(1-a)/s(i)+2/(1-a)*t_bar/s(i))/(1+2*q);
end
sigma_v_bar=sqrt(Av.^2+Bv.^2+(C1v.^2+C2v.^2+C3v.^2)*u^2);
figure
pcolor(s,t_bar,sigma_v_bar)
hold on
axis square
axis xy
shading interp
hx=xlabel('$\dot{\vartheta_0}\Delta t$',...
'interpreter','latex','Fontsize',12);
%set(hx,'Position',[0.5 -0.06]);
hy=ylabel('$t^\prime/\Delta t$','interpreter','latex','Fontsize',12);
%set(hy,'Position',[-0.06 0.5]);
%set(gca,'XTick',0.05:0.1:0.95,'YTick',0:0.1:1);
set(gca,'FontSize',12);
hc=colorbar;
[clim1,clim2]=newclim(sigma_v_bar,0,0.2);
caxis([clim1,clim2])
ht=title(hc,'$\sigma_v/R(\dot{\vartheta_0}+\ddot{\vartheta}_0\Deltat)$'...
,'interpreter','latex','Fontsize',12);
set(ht,'Position',[0 clim2+(clim2-clim1)*0.03]);
```

```
[C,h]=contour(s,t_bar,sigma_v_bar,linspace(clim1,clim2,10),'k--');
clabel(C,h);
% print(gcf,[path,'sigma_v_',filename,'.pdf'],'-dpdf','-r300');
% print(gcf,[path,'sigma_v_',filename,'.eps'],'-depsc ','-r300');
% print(gcf,[path,'sigma_v_',filename,'.png'],'-dpng','-r300');

Aa=zeros(N,M);
Ba=zeros(N,M);
C1a=zeros(N,M);
C2a=zeros(N,M);
C3a=zeros(N,M);
for i=1:M
    Aa(:,i)=((-2/a/(1-a)/2/q/s(i))*(1-cos(a*s(i)+a^2*q*s(i)))...
        -(-2/(1-a)/2/q/s(i))*(1-cos(s(i)+q*s(i)))...
        -(cos(s(i)*t_bar+s(i)*q*t_bar.^2).*(s(i)/2/q+2*s(i)*q*t_bar.^2+...
        2*s(i)*t_bar)+sin(s(i)*t_bar+s(i)*q*t_bar.^2)))...
        /sqrt(1+s(i)^2/4/q^2);
    Ba(:,i)=((-2/a/(1-a)/2/q/s(i))*sin(a*s(i)+a^2*q*s(i))...
        -(-2/(1-a)/2/q/s(i))*sin(s(i)+q*s(i))...
        -(-sin(s(i)*t_bar+s(i)*q*t_bar.^2).*(s(i)/2/q+2*s(i)*q*t_bar.^2+...
        2*s(i)*t_bar)+cos(s(i)*t_bar+s(i)*q*t_bar.^2)))...
        /sqrt(1+s(i)^2/4/q^2);
    C1a(:,i)=2/a/2/q/s(i)/sqrt(1+s(i)^2/4/q^2);
    C2a(:,i)=-2/a/(1-a)/2/q/s(i)/sqrt(1+s(i)^2/4/q^2);
    C3a(:,i)=2/(1-a)/2/q/s(i)/sqrt(1+s(i)^2/4/q^2);
end
sigma_a_bar=sqrt(Aa.^2+Ba.^2+(C1a.^2+C2a.^2+C3a.^2)*u^2);
figure
pcolor(s,t_bar,sigma_a_bar)
hold on
axis square
axis xy
shading interp
hx=xlabel('$\dot{\vartheta_0}\Delta t$',...
'interpreter','latex','Fontsize',12);
%set(hx,'Position',[0.5 -0.06]);
hy=ylabel('$t^\prime/\Delta t$','interpreter','latex','Fontsize',12);
%set(hy,'Position',[-0.06 0.5]);
%set(gca,'XTick',0.05:0.1:0.95,'YTick',0:0.1:1);
set(gca,'FontSize',12);
hc=colorbar;
[clim1,clim2]=newclim(sigma_a_bar,0,0.2);
caxis([clim1,clim2])
ht=title(hc,'$\sigma_a/(R\sqrt{{\ddot{\vartheta_0}}^2...
    +{\dot{\vartheta_0}}^4})$'...
    ,'interpreter','latex','Fontsize',12);
set(ht,'Position',[0 clim2+(clim2-clim1)*0.03]);
[C,h]=contour(s,t_bar,sigma_a_bar,linspace(clim1,clim2,10),'k--');
clabel(C,h);
% print(gcf,[path,'sigma_a_',filename,'.pdf'],'-dpdf','-r300');
% print(gcf,[path,'sigma_a_',filename,'.eps'],'-depsc ','-r300');
% print(gcf,[path,'sigma_a_',filename,'.png'],'-dpng','-r300');

Kv=sqrt(eta*sigma_x_bar.^2+(1-eta)*sigma_v_bar.^2);
figure
pcolor(s,t_bar,Kv)
hold on
```

```matlab
        axis square
        axis xy
        shading interp
        hx=xlabel('$\dot{\vartheta_0}\Delta t$',...
        'interpreter','latex','Fontsize',12);
        %set(hx,'Position',[0.5 -0.06]);
        hy=ylabel('$t^\prime/\Delta t$','interpreter','latex','Fontsize',12);
        %set(hy,'Position',[-0.06 0.5]);
        %set(gca,'XTick',0.05:0.1:0.95,'YTick',0:0.1:1);
        set(gca,'FontSize',12);
        hc=colorbar;
        [clim1,clim2]=newclim(Kv,0,0.2);
        caxis([clim1,clim2])
        ht=title(hc,'$K_v$','interpreter','latex','Fontsize',12);
        set(ht,'Position',[0 clim2+(clim2-clim1)*0.03]);
        [C,h]=contour(s,t_bar,Kv,linspace(clim1,clim2,10),'k--');
        clabel(C,h);
        % print(gcf,[path,'Kv_',filename,'.pdf'],'-dpdf','-r300');
        % print(gcf,[path,'Kv_',filename,'.eps'],'-depsc','-r300');
        print(gcf,[path,'Kv_',filename,'.png'],'-dpng','-r300');

        Ka=sqrt(eta*sigma_x_bar.^2+(1-eta)*sigma_a_bar.^2);
        figure
        pcolor(s,t_bar,Ka)
        hold on
        axis square
        axis xy
        shading interp
        hx=xlabel('$\dot{\vartheta_0}\Delta t$',...
        'interpreter','latex','Fontsize',12);
        %set(hx,'Position',[0.5 -0.06]);
        hy=ylabel('$t^\prime/\Delta t$','interpreter','latex','Fontsize',12);
        %set(hy,'Position',[-0.06 0.5]);
        %set(gca,'XTick',0.05:0.1:0.95,'YTick',0:0.1:1);
        set(gca,'FontSize',12);
        hc=colorbar;
        [clim1,clim2]=newclim(Ka,0,0.2);
        caxis([clim1,clim2])
        ht=title(hc,'$K_a$','interpreter','latex','Fontsize',12);
        set(ht,'Position',[0 clim2+(clim2-clim1)*0.03]);
        [C,h]=contour(s,t_bar,Ka,linspace(clim1,clim2,10),'k--');
        clabel(C,h);
        % print(gcf,[path,'Ka_',filename,'.pdf'],'-dpdf','-r300');
        % print(gcf,[path,'Ka_',filename,'.eps'],'-depsc ','-r300');
        print(gcf,[path,'Ka_',filename,'.png'],'-dpng','-r300');
        close all
    end
end
```

A.2 Quadruple-pulse calculation

```
%       MS Thesis Script Appendix - Quadruple-Pulse PTV
%
%       t_bar           - normalized time                       [1]
%        s              - normalized displacement               [1]
%        q              - acceleration factor                   [1]
%        u              - center location uncertainty           [100%]
%      d_tau            - particle diameter                     [mm]
%        R              - radius of curvature                   [mm]
%        b              - beta                                  [1]
%        c              - gamma                                 [1]
%    sigma_x_bar        - normalized postiion rms error         [1]
%    sigma_v_bar        - normalized velocity rms error         [1]
%    sigma_a_bar        - normalized acceleration rms error     [1]


clc,clear all,close all

N=1000;
M=1000;
t_bar=linspace(0,1,N)';
d_tau=22.5e-03;
R=2;
b=1/3;
c=2/3;
eta=1/2;
path='E:\Research\Multi-pulse PIV\PTV Simulation\MS Thesis Figures 4pulse\';
for q=[-0.3 -0.1 eps 0.2 0.4]
    for u=[0.03 0.075 0.15 0.5 0.75 1]*1e-02

        s=linspace(20/(0.3/u),40/(0.3/u),1000);

        filename=sprintf('q%+04du%+07d',round(q*100),round(u*100000));

        a1=[-(b*c+b+c);1+b+c;-1]/b/c;
        a2=[c;-(c+1);1]/b/(1-b)/(c-b);
        a3=[-b;b+1;-1]/c/(1-c)/(c-b);
        a4=[b*c;-(b+c);1]/(1-b)/(1-c);

        Ax=zeros(N,M);
        Bx=zeros(N,M);
        C1x=zeros(N,M);
        C2x=zeros(N,M);
        C3x=zeros(N,M);
        C4x=zeros(N,M);
        for i=1:M
            Ax(:,i)=[t_bar,t_bar.^2,t_bar.^3]*a2*(1-cos(b*s(i)+b^2*q*s(i)))...
                +[t_bar,t_bar.^2,t_bar.^3]*a3*(1-cos(c*s(i)+c^2*q*s(i)))...
                +[t_bar,t_bar.^2,t_bar.^3]*a4*(1-cos(s(i)+q*s(i)))...
                -(1-cos(s(i)*t_bar+s(i)*q*t_bar.^2));
            Bx(:,i)=[t_bar,t_bar.^2,t_bar.^3]*a2*sin(b*s(i)+b^2*q*s(i))...
                +[t_bar,t_bar.^2,t_bar.^3]*a3*sin(c*s(i)+c^2*q*s(i))...
                +[t_bar,t_bar.^2,t_bar.^3]*a4*sin(s(i)+q*s(i))...
                -sin(s(i)*t_bar+s(i)*q*t_bar.^2);
            C1x(:,i)=1+[t_bar,t_bar.^2,t_bar.^3]*a1;
            C2x(:,i)=[t_bar,t_bar.^2,t_bar.^3]*a2;
            C3x(:,i)=[t_bar,t_bar.^2,t_bar.^3]*a3;
```

```
        C4x(:,i)=[t_bar,t_bar.^2,t_bar.^3]*a4;
end
sigma_x_bar=sqrt(Ax.^2+Bx.^2+(C1x.^2+C2x.^2+C3x.^2+C4x.^2)*u^2);
figure
pcolor(s,t_bar,sigma_x_bar)
hold on
axis square
axis xy
shading interp
hx=xlabel('$\dot{\vartheta_0}\Delta t$',...
'interpreter','latex','Fontsize',12);
% set(hx,'Position',[0.6 -0.06]);
hy=ylabel('$t^\prime/\Delta t$','interpreter','latex','Fontsize',12);
%set(hy,'Position',[-0.08 0.5]);
% set(gca,'XTick',0.05:0.1:1.2,'YTick',0:0.1:1);
set(gca,'FontSize',12);
hc=colorbar;
[clim1,clim2]=newclim(sigma_x_bar,0,0.2);
caxis([clim1,clim2])
ht=title(hc,'$\sigma_x/R$','interpreter','latex','Fontsize',12);
set(ht,'Position',[0 clim2+(clim2-clim1)*0.03]);
% print(gcf,[path,'sigma_x_',filename,'.pdf'],'-dpdf','-r300');
% print(gcf,[path,'sigma_x_',filename,'.eps'],'-depsc ','-r300');

Av=zeros(N,M);
Bv=zeros(N,M);
C1v=zeros(N,M);
C2v=zeros(N,M);
C3v=zeros(N,M);
C4v=zeros(N,M);
for i=1:M
    Av(:,i)=([ones(N,1)/s(i),2*t_bar/s(i),3*t_bar.^2/s(i)]*a2...
        *(1-cos(b*s(i)+b^2*q*s(i)))...
        +[ones(N,1)/s(i),2*t_bar/s(i),3*t_bar.^2/s(i)]*a3...
        *(1-cos(c*s(i)+c^2*q*s(i)))...
        +[ones(N,1)/s(i),2*t_bar/s(i),3*t_bar.^2/s(i)]*a4...
        *(1-cos(s(i)+q*s(i)))...
        -(sin(s(i)*t_bar+s(i)*q*t_bar.^2).*(1+2*q*t_bar)))/(1+2*q);
    Bv(:,i)=([ones(N,1)/s(i),2*t_bar/s(i),3*t_bar.^2/s(i)]*a2...
        *sin(b*s(i)+b^2*q*s(i))...
        +[ones(N,1)/s(i),2*t_bar/s(i),3*t_bar.^2/s(i)]*a3...
        *sin(c*s(i)+c^2*q*s(i))...
        +[ones(N,1)/s(i),2*t_bar/s(i),3*t_bar.^2/s(i)]*a4...
        *sin(s(i)+q*s(i))...
        -cos(s(i)*t_bar+s(i)*q*t_bar.^2).*(1+2*q*t_bar))/(1+2*q);
    C1v(:,i)=([ones(N,1)/s(i),2*t_bar/s(i),3*t_bar.^2/s(i)]*a1)/(1+2*q);
    C2v(:,i)=([ones(N,1)/s(i),2*t_bar/s(i),3*t_bar.^2/s(i)]*a2)/(1+2*q);
    C3v(:,i)=([ones(N,1)/s(i),2*t_bar/s(i),3*t_bar.^2/s(i)]*a3)/(1+2*q);
    C4v(:,i)=([ones(N,1)/s(i),2*t_bar/s(i),3*t_bar.^2/s(i)]*a4)/(1+2*q);
end
sigma_v_bar=sqrt(Av.^2+Bv.^2+(C1v.^2+C2v.^2+C3v.^2+C4v.^2)*u^2);
figure
pcolor(s,t_bar,sigma_v_bar)
hold on
axis square
axis xy
shading interp
```

84

```
hx=xlabel('$\dot{\vartheta_0}\Delta t$',...
'interpreter','latex','Fontsize',12);
% set(hx,'Position',[0.6 -0.06]);
hy=ylabel('$t^\prime/\Delta t$','interpreter','latex','Fontsize',12);
% set(hy,'Position',[-0.08 0.5]);
% set(gca,'XTick',0.05:0.1:1.2,'YTick',0:0.1:1);
set(gca,'FontSize',12);
hc=colorbar;
[clim1,clim2]=newclim(sigma_v_bar,0,0.2);
caxis([clim1,clim2])
ht=title(hc,'$\sigma_v/R\dot{\vartheta_0}$',...
'interpreter','latex','Fontsize',12);
set(ht,'Position',[0 clim2+(clim2-clim1)*0.03]);
% print(gcf,[path,'sigma_v_',filename,'.pdf'],'-dpdf','-r300');
% print(gcf,[path,'sigma_v_',filename,'.eps'],'-depsc ','-r300');

Aa=zeros(N,M);
Ba=zeros(N,M);
C1a=zeros(N,M);
C2a=zeros(N,M);
C3a=zeros(N,M);
C4a=zeros(N,M);
for i=1:M
    Aa(:,i)=([zeros(N,1),ones(N,1)/q/s(i),3*t_bar/q/s(i)]*a2...
        *(1-cos(b*s(i)+b^2*q*s(i)))...
        +[zeros(N,1),ones(N,1)/q/s(i),3*t_bar/q/s(i)]*a3...
        *(1-cos(c*s(i)+c^2*q*s(i)))...
        +[zeros(N,1),ones(N,1)/q/s(i),3*t_bar/q/s(i)]*a4...
        *(1-cos(s(i)+q*s(i)))...
        -(cos(s(i)*t_bar+s(i)*q*t_bar.^2)...
        .*(s(i)/2/q+2*s(i)*q*t_bar.^2+2*s(i)*t_bar)...
        +sin(s(i)*t_bar+s(i)*q*t_bar.^2)))/sqrt(1+s(i)^2/4/q^2);
    Ba(:,i)=([zeros(N,1),ones(N,1)/q/s(i),3*t_bar/q/s(i)]*a2...
        *sin(b*s(i)+b^2*q*s(i))...
        +[zeros(N,1),ones(N,1)/q/s(i),3*t_bar/q/s(i)]*a3...
        *sin(c*s(i)+c^2*q*s(i))...
        +[zeros(N,1),ones(N,1)/q/s(i),3*t_bar/q/s(i)]*a4...
        *sin(s(i)+q*s(i))...
        -(-sin(s(i)*t_bar+s(i)*q*t_bar.^2)...
        .*(s(i)/2/q+2*s(i)*q*t_bar.^2+2*s(i)*t_bar)...
        +cos(s(i)*t_bar+s(i)*q*t_bar.^2)))/sqrt(1+s(i)^2/4/q^2);
    C1a(:,i)=[zeros(N,1),ones(N,1)/q/s(i),3*t_bar/q/s(i)]*a1...
        /sqrt(1+s(i)^2/4/q^2);
    C2a(:,i)=[zeros(N,1),ones(N,1)/q/s(i),3*t_bar/q/s(i)]*a2...
        /sqrt(1+s(i)^2/4/q^2);
    C3a(:,i)=[zeros(N,1),ones(N,1)/q/s(i),3*t_bar/q/s(i)]*a3...
        /sqrt(1+s(i)^2/4/q^2);
    C4a(:,i)=[zeros(N,1),ones(N,1)/q/s(i),3*t_bar/q/s(i)]*a4...
        /sqrt(1+s(i)^2/4/q^2);
end
sigma_a_bar=sqrt(Aa.^2+Ba.^2+(C1a.^2+C2a.^2+C3a.^2+C4a.^2)*u^2);
figure
pcolor(s,t_bar,sigma_a_bar)
hold on
axis square
axis xy
shading interp
```

```
hx=xlabel('$\dot{\vartheta_0}\Delta t$',...
'interpreter','latex','Fontsize',12);
% set(hx,'Position',[0.6 -0.06]);
hy=ylabel('$t^\prime/\Delta t$','interpreter','latex','Fontsize',12);
% set(hy,'Position',[-0.08 0.5]);
% set(gca,'XTick',0.05:0.1:1.2,'YTick',0:0.1:1);
set(gca,'FontSize',12);
hc=colorbar;
[clim1,clim2]=newclim(sigma_a_bar,0,0.2);
caxis([clim1,clim2])
ht=title(hc,'$\sigma_a/(R\sqrt{{\ddot{\vartheta_0}}^2...
    +{\dot{\vartheta_0}}^4)$'...
    ,'interpreter','latex','Fontsize',12);
set(ht,'Position',[0 clim2+(clim2-clim1)*0.03]);
% print(gcf,[path,'sigma_a_',filename,'.pdf'],'-dpdf','-r300');
% print(gcf,[path,'sigma_a_',filename,'.eps'],'-depsc ','-r300');

Kv=sqrt(eta*sigma_x_bar.^2+(1-eta)*sigma_v_bar.^2);
figure
pcolor(s,t_bar,Kv)
hold on
axis square
axis xy
shading interp
hx=xlabel('$\dot{\vartheta_0}\Delta t$',...
'interpreter','latex','Fontsize',12);
% set(hx,'Position',[0.6 -0.06]);
hy=ylabel('$t^\prime/\Delta t$','interpreter','latex','Fontsize',12);
% set(hy,'Position',[-0.08 0.5]);
% set(gca,'XTick',0.05:0.1:1.2,'YTick',0:0.1:1);
set(gca,'FontSize',12);
hc=colorbar;
[clim1,clim2]=newclim(Kv,0,0.2);
caxis([clim1,clim2])
ht=title(hc,'$K_v$','interpreter','latex','Fontsize',12);
set(ht,'Position',[0 clim2+(clim2-clim1)*0.03]);
[C,h]=contour(s,t_bar,Kv,linspace(clim1,clim2,10),'k--');
clabel(C,h);
% print(gcf,[path,'Kv_',filename,'_4p.pdf'],'-dpdf','-r300');
% print(gcf,[path,'Kv_',filename,'_4p.eps'],'-depsc','-r300');
% print(gcf,[path,'Kv_',filename,'_4p.png'],'-dpng','-r300');

Ka=sqrt(eta*sigma_x_bar.^2+(1-eta)*sigma_a_bar.^2);
figure
pcolor(s,t_bar,Ka)
hold on
axis square
axis xy
shading interp
hx=xlabel('$\dot{\vartheta_0}\Delta t$',...
'interpreter','latex','Fontsize',12);
% set(hx,'Position',[0.6 -0.06]);
hy=ylabel('$t^\prime/\Delta t$','interpreter','latex','Fontsize',12);
% set(hy,'Position',[-0.08 0.5]);
% set(gca,'XTick',0.05:0.1:1.2,'YTick',0:0.1:1);
set(gca,'FontSize',12);
hc=colorbar;
```

```
        [clim1,clim2]=newclim(Ka,0,0.2);
        caxis([clim1,clim2])
        ht=title(hc,'$K_a$','interpreter','latex','Fontsize',12);
        set(ht,'Position',[0 clim2+(clim2-clim1)*0.03]);
        [C,h]=contour(s,t_bar,Ka,linspace(clim1,clim2,10),'k--');
        clabel(C,h);
        % print(gcf,[path,'Ka_',filename,'_4p.pdf'],'-dpdf','-r300');
        % print(gcf,[path,'Ka_',filename,'_4p.eps'],'-depsc ','-r300');
        % print(gcf,[path,'Ka_',filename,'_4p.png'],'-dpng','-r300');
        close all
    end
end
```

APPENDIX B

ESTIMATION OF LOCAL RADIUS OF CURVATURE AND ACCELERATION FACTOR USING THREE PARTICLE POSITIONS

This appendix presents the derivation of Equation (2.24) and (2.25), which estimate the local radius of curvature and the acceleration factor using three measured particle locations.

B.1 Estimation of local radius of curvature

Figure B.1 illustrates the particle trajectory as a locally circular path, as indicated by the solid line. The dashed line shows a extended fraction of the local circle. Along the trajectory, three particle position, $\boldsymbol{X}_{pi,m}$, $i = 1, 2, 3$ are measured. The local radius of curvature is R. The angle spanned by vector $\boldsymbol{X}_{p1,m} - \boldsymbol{X}_{p2,m}$ and vector $\boldsymbol{X}_{p3,m} - \boldsymbol{X}_{p2,m}$ is denoted as φ, and given by

$$\varphi = cos^{-1} \left[\frac{(\boldsymbol{X}_{p1,m} - \boldsymbol{X}_{p2,m}) \cdot (\boldsymbol{X}_{p3,m} - \boldsymbol{X}_{p2,m})}{\Delta_{12} \Delta_{23}} \right] \tag{B.1}$$

with $\Delta_{12} = |\boldsymbol{X}_{p1,m} - \boldsymbol{X}_{p2,m}|$, and $\Delta_{23} = |\boldsymbol{X}_{p3,m} - \boldsymbol{X}_{p2,m}|$. Assuming that three particle locations are approximately on the local circle, with the knowledge of fundamental geometry, the local radius of curvature can be estimated as

$$R \approx \frac{|\boldsymbol{X}_{p3,m} - \boldsymbol{X}_{p1,m}|}{2 sin\varphi}. \tag{B.2}$$

B.2 Estimation of acceleration factor

The acceleration factor, $\ddot{\vartheta}_0 \Delta t / 2\dot{\vartheta}_0$, characterizes the ratio of the particle displacement due to the tangential acceleration, $R\ddot{\vartheta}_0$, to that due to the initial particle velocity, $R\dot{\vartheta}_0$. Recall that the particle motion is modeled in this work as the equation (2.7). Thus, with known particle positions, $\boldsymbol{X}_{pi,m}$, and known particle angular displacement from equation (2.7) at $t' = \alpha\Delta t$ and Δt, we can build up the following two equalities,

$$\begin{cases} 2sin^{-1}(\Delta_{12}/2R) = \dot{\vartheta}_0 \alpha\Delta t + \dfrac{1}{2}\ddot{\vartheta}_0 \alpha^2 \Delta t^2 \\ 2sin^{-1}(\Delta_{23}/2R) = \dot{\vartheta}_0(1 - \alpha)\Delta t + \dfrac{1}{2}\ddot{\vartheta}_0(1 - \alpha^2)\Delta t^2 \end{cases} \tag{B.3}$$
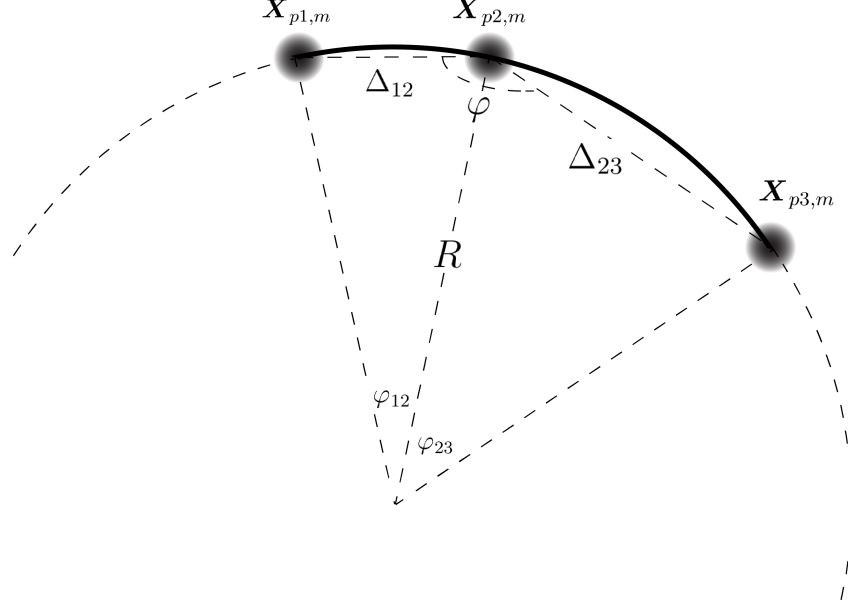
Figure B.1: Illustration of a particle trajectory as a locally circular path

The left-hand side of equation (B.3) comes from the formula of calculating the central angle given the chord length and the radius. For simplicity, we use φ_{12} and φ_{23} to denote the central angles, i.e.

$$\varphi_{12} = 2sin^{-1}(\Delta_{12}/2R), \qquad \varphi_{23} = 2sin^{-1}(\Delta_{23}/2R) \tag{B.4}$$

as shown in Figure B.1. The equation (B.3) can be solved in terms of $\dot{\vartheta}_0 \Delta t$ and $\ddot{\vartheta}_0 \Delta t^2$, and thus one can estimate the acceleration factor. Alternatively, by taking the ratio of the two equations in (B.3), one can get

$$\alpha^2 \frac{1/\alpha + \ddot{\vartheta}_0 \Delta t/2\dot{\vartheta}_0}{1 + \ddot{\vartheta}_0 \Delta t/2\dot{\vartheta}_0} = \frac{\varphi_{12}}{\varphi_{12} + \varphi_{23}}. \tag{B.5}$$

From this, the acceleration factor is estimated as

$$\ddot{\vartheta}_0 \Delta t/2\dot{\vartheta}_0 \approx \frac{\alpha \varphi_{23} - (1 - \alpha)\varphi_{12}}{-\alpha^2 \varphi_{23} + (1 - \alpha^2)\varphi_{12}}, \tag{B.6}$$

90